

Study of New Miniaturized Microwave Devices based on Ratchet Effect in an Environment of Asymmetric Nano-Scatterers

Dina Medhat Abdel Maksoud

▶ **To cite this version:**

Dina Medhat Abdel Maksoud. Study of New Miniaturized Microwave Devices based on Ratchet Effect in an Environment of Asymmetric Nano-Scatterers. Electromagnetism. Institut National Polytechnique de Toulouse - INPT, 2012. English. NNT : 2012INPT0075 . tel-04279861v2

HAL Id: tel-04279861

https://theses.hal.science/tel-04279861v2

Submitted on 10 Nov 2023

HAL is a multi-disciplinary open access archive for the deposit and dissemination of scientific research documents, whether they are published or not. The documents may come from teaching and research institutions in France or abroad, or from public or private research centers.

L'archive ouverte pluridisciplinaire **HAL**, est destinée au dépôt et à la diffusion de documents scientifiques de niveau recherche, publiés ou non, émanant des établissements d'enseignement et de recherche français ou étrangers, des laboratoires publics ou privés.

Université de Toulouse

THÈSE

En vue de l'obtention du

DOCTORAT DE L'UNIVERSITÉ DE TOULOUSE

Délivré par :
Institut National Polytechnique de Toulouse (INP Toulouse)

Discipline ou spécialité :

Micro-Ondes, Electromagnétisme et Optoélectronique

Présentée et soutenue par :
Dina MEDHAT MOHAMED ABDEL MAKSOUD

le : lundi 15 octobre 2012

Titre :

Study of New Miniaturized Microwave Devices based on Ratchet Effect in an Environment of Asymmetric Nano-Scatterers

---

Ecole doctorale :
Génie Electrique, Electronique et Télécommunications (GEET)

Unité de recherche :
LAAS-CNRS

Directeur(s) de Thèse :
M. Hervé AUBERT, Professeur des Universités, INP, Toulouse (Directeur de thèse)
M. Alexandru TAKACS, Maître de Conférences, UPS, Toulouse (Co-directeur de thèse)

Rapporteurs :

M. Alain REINEIX, Directeur de Recherche du CNRS, Université de Limoges
M. Pierre BLONDY, Professeur des Universités, Université de Limoges

Membre(s) du jury :
Mme Elodie RICHALOT, Professeur des Universités, Université Paris-Est Marne-la-Vallée
M. Jean-Claude PORTAL, Professeur des Universités, INSA, Toulouse
M. Dima SHEPELYANSKY, Professeur des Universités, UPS, Toulouse (invité)
M. Georgios DELIGEORGIS, Ingénieur de Recherche, LAAS-CNRS, Toulouse (invité)

ABSTRACT

Nanotechnology is a growing field that has attracted significant research attention due to its unlimited potential applications. Millimeter wave technology is another interesting field that plays a leading role in the development of wireless communications systems. Combining these two advanced research fields together, has given rise to the innovation of the Ratchet Device which is now a new challenging application. This device has a nanoscale size and its concept of operation consists of generating a DC voltage when radiating a two-dimensional electron gas based device with microwave energy.
The aim of this thesis is in trying to improve the device response and hence opening new perspectives in the fabrication of high frequency field detectors on the nanoscale level. Unfortunately, the current Ratchet Devices, based on semiconductor heterostructures, realized till now, operate at low temperatures to ensure high electron mobility. This condition necessitates the use of a complex experimental setup that has a great impact on the induced voltage and on the reproducibility of the observed Ratchet phenomenon.
In this context, the work performed within the framework of this thesis has addressed this problem in two parts. The first part concerns the electromagnetic analysis of the experimental setup behavior. This has been achieved by implementing intensive full wave electromagnetic simulations. Different solutions have been proposed to optimize the setup and thus enhance the Ratchet voltage produced. In addition to the electromagnetic study, some modulation measurements have been performed to test the feasibility of the Ratchet Device as an amplitude demodulator. The second part of this thesis deals with the study of the material composing the Ratchet Device. Recently, graphene has started to invade the scientific and the technological world with its fascinating electronic properties, such as its high electron mobility at room temperature, which distinguishes it from conventional materials that typically collide with obstacles. As a result, the idea of fabricating a Ratchet Device based on graphene instead of semiconductor heterojunctions has been introduced. Several design models, characterizations and RF measurements have been performed in order to obtain a reliable Ratchet Device suitable for many practical applications at room temperature. This has been done in the microwave frequency range and can also extend to the terahertz band.

I would like to take this opportunity to thank those without whom it would have been impossible to finish my thesis. Their support and help, all along the way, was crucial to me, and made this experience, an unforgettable one.

To my beloved parents; Somaya and Medhat, they are my ultimate source of encouragement. They have inspired me throughout my life. I thank them for their love, for their belief in me, for encouraging me to pursue my life dreams, and for all their prayers.

To my soul; my sister Sally, she is my great source of love and to my little angel; my niece Sandra.

To my brother-in-law; Diaa, to his sister; Reham and his mother; Aunt Aida.

To my one and only; kitty the cat, for his tenderness and intelligence.

To my closest friends; May, Iman and Noha. Since our childhood, together, we have shared good and hard times, and hopefully we will share much more happiness and good surprises in the future.

ACKNOWLEDGMENTS

I am forever grateful to my supervisor M. Hervé AUBERT. I have learnt so much from him, not only regarding the scientific aspect, but the personal aspect as well. He is able to deal with different personalities and cope with hard situations, all this while maintaining good spirits and with a smile on his face. Best communication tools indeed.
My sincere thanks to Alexandru TAKACS who supported and helped me throughut my thesis.
I would like to thank all the jury members for taking time to evaluate my work, for encouraging me and for giving me insightful comments.
I also want to thank Georgios DELIGEORGIS for the time he had spent in fabricating the Ratchet samples and for his valuable discussions. Thanks also go to Fabio COCCETTI and Manos TENTZERIS for their encouragements regarding my work, I really appreciated it.

I am thankful to all my friends and colleagues in LAAS with whom I shared great moments:

Serge KARBOYAN; what an annoying brother and a very helpful person. We were always figthing and laughting as the same time. But this spirit helped me to survive and to continue my thesis. Your jokes and your funny tricks are so creative. Keep up this good spirit.
Tonio IDDA; I learnt a lot from you. I really appreciated the time and effort you devoted to me. Good luck in your future plans.
Céline LECLERC; since we were in the same office, you were the first one to know about my thesis' problems. Thank you for your support, you were so nice with me. I will miss our talks and your cakes.
Ayoub RIFAI and Olivier RIPOCHE; I liked the spirit that you add both of you to our office especially when you talk about the latest movies.
Céline, Ayoub and Olivier; I will not mention here the tragic story that happened every time a bee comes into our office.

Mihai ALEXANDRU, Mariano ERCOLI, Nuria TORRES, Khaldoun SALEH and Sofiene BOUAZIZ; I will not be able to count all the great memories we have shared together. We have started togther the thesis adventure, so let us finish with victory to begin another fascinating chapter in our life.
Rosa DE PAOLIS; you are a very kind and decent person.
Giancarlo VINCENZ; thank you for the support and the useful discussion.
Hong LIU (Patricia); sweet smile and perfect Chinese cook.
I would like also to thank Trang THAI, Anya TRAILLE, Franck CHEBILA, Nisrina ABDO, Ayad GHANNAM, Seraphin Dieudonné NSELE, Amel ALI SLIMANE, Olga BUSHUEVA, Alexandre RUMEAU, Alexei CHEPELIANSKII and Leonardo ERMANN.
I am also grateful to Silvia FABIANI, Euloge TCHIKAYA, Badreddine OUAGAGUE, Hicham YOUSSEF and Michael KRAEMER.
My Egyptian friends in Toulouse; I will not forget our hangouts, our jokes and our laughs. You were always beside me.
Also, my Egyptian friends and colleagues who are preparing their Ph.D. all over the world; stay strong and make your mark on the world.
I am very grateful to my french family; Mr and Mrs PAPAIS, they treated me like their own daughter. I had a really good time with them and I enjoyed playing with their cat Caline and their dog Pacha.

The list is yet endless, and I am sure I missed some, so please forgive me. A final thank you to everyone who contributed in one way or another in this work.

CONTENTS

General Introduction 1

1 INTRODUCTION TO THE RATCHET EFFECT 3
- 1.1 General Definition 3
- 1.2 Some Examples of Ratchet Effect in Different Domains 4
- 1.3 Ratchet Device Based on Semiconductor Heterostructures and its Applications 4
  - 1.3.1 Ratchet Device based on AlGaAs/GaAs heterostructure 5
  - 1.3.2 Ratchet Device based on Si/SiGe heterostructure 10
  - 1.3.3 Other research works performed on Ratchet Device based on heterostructures 14
- 1.4 Ratchet Device Based on Graphene 15
- 1.5 Conclusion 16

2 ELECTROMAGNETIC ANALYSIS OF THE EXPERIMENTAL SETUP FRONT-END MODULE USED TO INVESTIGATE THE RATCHET EFFECT 17
- 2.1 Introduction 17
- 2.2 Description of the Experimental Setup 17
- 2.3 Electromagnetic Simulation Model of the Microwave Front-End Module 18
- 2.4 Evaluating the Intrinsic Performance of the Microwave Front-End Module 20
- 2.5 Parametric Analysis of the Microwave Front-End Module 21
- 2.6 Experimental Validation of the Simulations Results using Indirect Measurements Techniques 23
- 2.7 Different Proposed Techniques to Optimize the Front-End Module 27
  - 2.7.1 Electromagnetic illumination using the WR22 aperture 27
  - 2.7.2 Electromagnetic illumination using the WR22 aperture and a Diaphragm 27
  - 2.7.3 Electromagnetic illumination using the WR22 aperture and a Dielectric Lens 27
  - 2.7.4 Electromagnetic illumination using the WR22 and a Dielectric Multislab structure 28
  - 2.7.5 Electromagnetic illumination using the WR22 and a Horn Antenna 29
- 2.8 Performance Comparison between the Different Proposed Techniques 30
- 2.9 Conclusion 31

3 INFLUENCE OF THE CRYOGENIC METALLIC CAVITY SYSTEM ON THE ELECTROMAGNETIC BEHAVIOR OF THE SETUP USED AT LOW TEMPERATURE 33
- 3.1 Introduction 33
- 3.2 Description of the Front-End Module used at Low Temperature 33
- 3.3 Electromagnetic Simulation Models of the Front-End Module used at Low Temperature 33
- 3.4 Study of the Electromagnetic Response of the Simulation Models 34
- 3.5 Dependence of the Setup Electromagnetic Response on the Operating Frequency 41
- 3.6 Conclusion 43

4 FEASIBILITY STUDY OF AMPLITUDE DEMODULATORS BASED ON RATCHET EFFECT 45
4.1 Introduction 45
4.2 Experimental Setup used in the Analog Amplitude Demodulation Tests 45
4.3 Description of the Studied Samples 47
4.4 Experimental Results 47
4.5 Pulse Modulation Techniques 52
4.5.1 Pulse Width Modulation (PWM) 52
4.5.2 Pulse Position Modulation (PPM) 52
4.6 Conclusion 53
5 EXPERIMENTAL INVESTIGATION OF THE RATCHET EFFECT IN GRAPHENE AT ROOM TEMPERATURE 55
5.1 Elementary Properties of Graphene 55
5.2 Theoretical, Numerical and Analytical Study of the Ratchet Electron Transport in Graphene 55
5.2.1 Electrons motion in graphene 56
5.2.2 Properties of Ratchet transport in graphene 56
5.3 Photocurrent Generation in Graphene Monolayer under Terahertz Radiation 57
5.4 Characterization and RF Measurements of a Graphite Sample with a Periodic Array of Asymmetric Shaped Antidots 57
5.4.1 Sample description 58
5.4.2 I-V measurements 59
5.4.3 RF measurements at room temperature 59
5.5 Designs, Characterizations and RF Measurements of Monolayer and Bilayer Graphene Samples with a Periodic Array of Asymmetric Shaped Antidots 60
5.5.1 Sample designs 61
5.5.2 Graphene sample selection 62
5.5.3 Antidots patterning 64
5.5.4 Mobility and electron density 65
5.5.5 Description of the experimental setup used to study the Ratchet Effect at room temperature 66
5.5.6 Experimental conditions and the results obtained 68
5.6 Conclusion 78
General Conclusion and Perspectives 80

BIBLIOGRAPHY 83
Publications 88
Appendix 89
A CALCULATION OF THE NUMBER OF PROPAGATING MODES IN A CIRCULAR WAVEGUIDE USING A MATLAB CODE 91
B EFFECT OF THE SUBSTRATE THICKNESS ON THE INCIDENT ELECTRIC FIELD 97

LIST OF FIGURES

Figure 1 Schematic of the Feynman-Smoluchowski Ratchet Device. 3
Figure 2 Photo showing the motion of water droplet on asymmetric surface [5]. 4
Figure 3 Schematic of the hexagonal lattice parameters. 5
Figure 4 Design and AFM image of AlGaAs/GaAs sample with a period a = 1.5 µm and a radius r = 0.5 µm, patterned in the middle of the three Hall bars [5]. 6
Figure 5 Longitudinal and transversal magnetoresistance measured at low temperature: Red curve is the SdH (B vs Rxx), without microwave radiation. Blue curve is the MIRO's (B vs Rxx), with microwave radiation. Green line is the Hall resistance (B vs Rxy), with microwave radiation [5]. 7
Figure 6 Longitudinal magnetoresistivity measured at low temperature. Blue curve is for circular antidots. Red curve is for pure 2DEG [5, 6]. 7
Figure 7 Induced photovoltage measured when applying a magnetic field on circular and semicircular antidots for two different microwave polarizations [5, 6]. 8
Figure 8 Induced photovoltage (for two different microwave polarizations) and electron mobility (for semicircular antidots and 2DEG) for large temperature range [5, 6]. 9
Figure 9 Induced photovoltage measured when varying the output microwave power for two different microwave polarizations [5, 6]. 10
Figure 10 (a) AFM image of Si/SiGe sample with a period a = 0.6 µm and a radius r = 0.2 µm. (b) Schematic of the Si/SiGe heterostructure layers. (c) The dimensions of the three Hall bar fabricated on the sample [9]. 11
Figure 11 (a) Induced photovoltage measured when applying a magnetic field on 2DEG, circular and semicircular antidots (b) for two different microwave polarizations. (c) Induced photovoltage measured for large temperature range. (d) Electron mobility measured (for 2DEG, semicircular and circular antidots) for large temperature range. (e) Induced photovoltage measured when varying the output microwave power [9]. 12
Figure 12 Induced photovoltage measured when applying a magnetic field for different temperatures. Inset is a schematic of the Hall bar dimensions in which a 2DEG and semicircular antidots have been fabricated [10]. 13
Figure 13 Induced photovoltage measured when applying a magnetic field for different microwave frequencies, at T = 4 K and a power level of 30 dBm at the microwave generator output. 14
Figure 14 (a) Photo [5] of the complete experimental setup. (b) Schematic of the setup showing the different parts of the cryogenic system used. (c) Photo of the sample connected to the package using wire bonding. 18

Figure 15 3D simulation model representing the microwave front-end module of the experimental setup. 19
Figure 16 P_n, K_E and K_P in function of d1 and the diaphragm materials, for d2 = 0.162 mm and c_x = 3 mm. 22
Figure 17 P_n, K_E and K_P in function of d2 and the diaphragm materials, for d1 = 1.5 mm and c_x = 3 mm. 22
Figure 18 P_n, K_E and K_P in function of c_x and the diaphragm materials, for d1 = 1.5 mm and d2 = 0.162 mm. 23
Figure 19 HFSS model of the proposed back-to-back structure. 24
Figure 20 Simulated S-parameters for the back-to-back structure in function of the slot length c_x and the diaphragm materials. 25
Figure 21 (a) Schematic of the experimental back-to-back structure. (b) Photo of the back-to-back structure connected to the VNA. (c) Set of metallic diaphragms and plastic pieces. 25
Figure 22 Measured and simulated reflection coefficient S11 of the two coaxial-to-WR22 transitions. 26
Figure 23 Measured and simulated transmission coefficient S21 of the coaxial-to-WR22 transitions, for slot length c_x = 2 mm, 3 mm and 4 mm. 26
Figure 24 HFSS model of the dielectric homogeneous lens representing the two shapes: (a) hemispherical and (b) spherical. 28
Figure 25 HFSS model of two-dielectric slabs structure. 29
Figure 26 HFSS model of the horn antenna designed. 29
Figure 27 Photo and schematic of the complex metallic parts inside the metallic cavity of the cryogenic system. 34
Figure 28 Schematics of the simulation models representing the front-end module used at low temperature. 35
Figure 29 (a) 3D plot of the magnitude of the total electric field in V/m inside the closed metallic cavity. (b)E_y, K_E and K_D calculated on the rectangles representing the sample at different positions (Model 0). 36
Figure 30 (a) 3D plot of the magnitude of the total electric field in V/m inside the closed metallic cavity. (b)E_y, K_E and K_D calculated on the rectangles representing the sample at different positions (Model 1). 37
Figure 31 (a) 3D plot of the magnitude of the total electric field in V/m inside the closed metallic cavity. (b)E_y, K_E and K_D calculated on the rectangles representing the sample at different positions (Model 2). 37
Figure 32 (a) 3D plot of the magnitude of the total electric field in V/m inside the closed metallic cavity. (b)E_y, K_E and K_D calculated on the rectangles representing the sample at different positions (Model 3). 38
Figure 33 E_y, K_E and K_D calculated on the rectangles representing the sample at different positions when varying the waveguide transition height between 15 mm and 19 mm. 39
Figure 34 (a) 3D plot of the magnitude of the total electric field in V/m inside the closed metallic cavity. (b)E_y, K_E and K_D calculated on the rectangles representing the sample at different positions (Model 4). 40

Figure 35 Convergence curve of Model 3 with maximum delta S = 0.01 and the minimum number of converged passes is 3. 40
Figure 36 Convergence curve of Model 4 with maximum delta S = 0.05 and the minimum number of converged passes is 2. 41
Figure 37 Variation of E_y for various operating frequencies at different positions of the sample (Model 4). 42
Figure 38 Variation of (a) K_E and (b) K_D for various operating frequencies at different positions of the sample (Model 4). 42
Figure 39 Schematic of the set used to test the modulation technique. 46
Figure 40 (a) Variation of the output power with respect to the duty cycle of the message signal at different frequencies using a carrier signal of 140 GHz. (b) Variation of the Ratchet photovoltage with respect to the duty cycle of the message signal, for a carrier signal of 44.09 GHz and a modulating signal of 1 KHz. 46
Figure 41 Schematic of the experimental setup and the instruments used in the amplitude demodulation tests. 47
Figure 42 Schematics of the two studied heterostructures samples based on Si/SiGe. (a) Sample with semicircular antidots, unpatterned 2DEG region and circular antidots. (b) Virgin sample without antidots. 48
Figure 43 The variation of the photovoltage generated by the semicircular antidots with respect to the microwave frequency. The studied sample is at zero magnetic field and a temperature of 4 K. 48
Figure 44 Semicircular antidots region response to the applied amplitude modulated RF signals with different modulation depths. An output power of 16 dBm, a carrier signal of f = 36.71 GHz and a sine wave modulating signal of f = 100 Hz have been used. 49
Figure 45 2DEG and the circular antidots region response to the applied amplitude modulated RF signal for an output power of 10 dBm and a modulation depth of 50 %. A carrier signal of f = 36.71 GHz and a sine wave modulating signal of f = 10 KHz have been used. 50
Figure 46 Virgin sample response to the applied amplitude modulated RF signal for an output power of 10 dBm and a modulation depth of 50 %. (a) Sine wave modulating signal, (b) pulse wave modulating signal, with f = 100 Hz and a carrier signal of f = 36.71 GHz. 51
Figure 47 Virgin sample response to the applied amplitude modulated RF signals when varying the output power and fixing the modulation depth at 50 %. (a) Sine wave modulating signal, (b) pulse wave modulating signal, with f = 100 Hz and a carrier signal of f = 36.71 GHz. 51
Figure 48 PWM; varied width and fixed period. 52
Figure 49 PPM; fixed width and varied period. 53
Figure 50 Graphene band structure showing the zero band gap [47]. 55
Figure 51 Schematic (cross section) of the graphite sample with an array of asymmetric antidots. 58
Figure 52 Image of the graphite sample observed with the optical microscope showing the contacts and the graphite flake between the contacts with a resolution of 5 X and 100 X in (a) and (b) respectively. 58

Figure 53 Image of the graphite sample observed with the AFM. (a) The region of antidots with a period of 721 nm, (b) one single antidot with a radius of 114 nm and a depth of 4 nm. 59
Figure 54 (a) Schematic of the first technique used to measure the resistance. (b) Photo of the second technique used: I-V small signal Test Probe Station. 60
Figure 55 Voltage variation with respect to frequency for a signal power of 0 and 10 dBm. 60
Figure 56 Initial design "A" of Ratchet Device. 61
Figure 57 Design "B": metallic areas are minimized to increase the field interaction. 62
Figure 58 Design "C": graphene placement is optimized to increase the interaction length and the number of antidots between the metallic contacts. 62
Figure 59 Optical image of graphene monolayer and bilayer flakes. The difference in contrast corresponds to different number of layers. 63
Figure 60 (a) Optical image of a graphene flake, no cracks appear in the flake area. (b) KPFM image of a graphene flake showing the craks. 63
Figure 61 AFM image of the arc shaped antidots. (a) Antidot radius is 36.75 nm and its thickness is 12.3 nm, (b) period between antidots is 197.3 nm. 64
Figure 62 AFM image showing the antidot depth of 2.081 nm. 65
Figure 63 HL5500PC Hall Effect Measurement System. 65
Figure 64 Photo of the experimental setup with its different parts used in measuring the Ratchet Effect. 66
Figure 65 Schematic representing the variation of the electric field polarization angle over the Ratchet Device. 67
Figure 66 Reflection coefficient S11 of the setup measured in three different cases: Metallic plate, Absorber and Polycarbonate plate. 68
Figure 67 Voltage variation with respect to time produced from a bilayer graphene flake with an array of arc shaped antidots. ON signifies that RF generator is switched ON, OFF signifies that RF generator is switched OFF. 69
Figure 68 Histogram of the produced voltage for 1000 points of measurements at angle = 0°, the applied power is 20 dBm and the frequency is 30.75 GHz. 70
Figure 69 Histogram of the produced voltage for 1000 points of measurements at: (a) angle = 15° and (b) angle = -15°, the applied power is 20 dBm and the frequency is 30.75 GHz. 71
Figure 70 Histogram of the produced voltage for 1000 points of measurements at: (a) angle = 25° and (b) angle = -25°, the applied power is 20 dBm and the frequency is 30.75 GHz. 71
Figure 71 Voltage variation with respect to the polarization angle. The horn antenna is at distance of 16 cm from the sample, the applied power is 20 dBm, the frequency is 30.75 GHz and the attenuation of the cable used is about 3 dB. 72
Figure 72 Reflection coefficient S11 of the modified setup measured with the presence of the sample. 72

Figure 73 Voltage variation with respect to the polarization angle. The horn antenna is at distance of 6 cm from the sample, the applied power is 20 dBm, the frequency is 30.5 GHz and the attenuation of the cable used is about 7 dB. 73
Figure 74 Voltage variation with respect to the frequency when the antenna is at 6 cm from the sample. This measurement has been repeated three times, taking the average of 20 points of measurements for each frequency. 74
Figure 75 Photo of the horn antenna (1-12 GHz) when it is at a distance of: (a) 11 cm and (b) 60 cm from the sample. 74
Figure 76 Reflection coefficient S11 of the setup measured when the horn antenna (1-12 GHz) is at a distance of 11 cm and 60 cm from the sample. 75
Figure 77 Voltage variation with respect to the frequency when the antenna is at 11 cm from the sample. This measurement has been repeated three times, taking the average of 20 points of measurements for each frequency. 75
Figure 78 Voltage ranges with respect to the frequency: (a) f = 1 to 3 GHz, (b) f = 3.5 to 7 GHz and (c) 7.5 to 12 GHz. 76
Figure 79 Voltage variation with respect to the frequency when the antenna is at 60 cm from the sample, taking the average of 20 points of measurements for each frequency. 77
Figure 80 Voltage ranges with respect to the frequency: (a) f = 1 to 3 GHz, (b) f = 3.5 to 6 GHz and (c) 6.5 to 12 GHz. 77
Figure 81 Schematic of dielectric boundaries. 97
Figure 82 (a) Total input reflection coefficient and (b) amount of the electric field on the substrate surface with respect to the the substrate thickness 99

LIST OF TABLES

Table 1 Summary of electromagnetic simulation results. 30
Table 2 Roots of Bessel function, **P_TM**. 92
Table 3 Roots of Bessel function Derivatives, **P_TE**. 92

GENERAL INTRODUCTION

This thesis is a part of a research work that attempts to develop a miniaturized microwave Ratchet Device that operates at room temperature. The contribution of this thesis to this main target could be classified into two parts:

i. Study of the actual case: by presenting the Ratchet Devices realized till now, their specific properties, their advantages and their drawbacks. Also this part contains the study of the experimental measurements environments conditions.

ii. Finding solutions: by implementing electromagnetic simulations to enhance the actual experiment conditions and by proposing new materials and new technology process in fabricating the Ratchet Device.

These two parts are presented in details in the thesis chapters which are organized as follows:

Chapter 1 gives a general introduction to the Ratchet Effect concept by clarifying the principle conditions that have to be satisfied in the different scientific domains in order to obtain this particular phenomenon. Then, this chapter focuses on the Ratchet Device based on two-dimensional electron gas system by presenting the several trials of the Ratchet Device fabrication and the experimental results obtained. Finally, it concludes by identifying the factors that cause a change in the device behavior.
Chapter 2 describes the whole complex experimental setup that exists in CNRS-LNCMI used in the measurements. An electromagnetic investigation and a parametric analysis of the microwave front-end module part are performed to evaluate its intrinsic performance. Different illunination techniques are proposed to optimize the setup response.
Chapter 3 analyses the influence of the closed metallic cryogenic system on the electromagnetic behavior of the setup used at low temperature. This has been achieved by creating a simple simulation model representing the cryogenic system, and then the model complexity has been increased by adding more details to be closer to the current setup. This analysis throws light on the importance of the Ratchet sample position inside the cryogenic system.
Chapter 4 proposes the use of the Ratchet Device as an amplitude demodulator. It presents the difference in response between patterned Ratchet sample (with antidots) and virgin sample (without antidots) to the modulation tests performed.
Chapter 5 presents a solution to the disadvantages of the Ratchet Device based on heterojunctions by changing the Ratchet Device material to graphene. A set of characterization and RF measurements performed in CNRS-LAAS explains the new Device properties.
The last part of this thesis is dedicated to a general conclusion and perspectives. This manuscript is ended by bibliography, appendix and a list of publications.
A part of this thesis work was financially supported by ANR NANOTERRA (French Research Agency) project.

1 INTRODUCTION TO THE RATCHET EFFECT

1.1 GENERAL DEFINITION

Ratchet Effect [1] is a commonly observed phenomenon that can be defined, in general terms, as the generation of motion in only one direction within an asymmetric system due to an external energy, while the motion in any other direction is prevented. For many years, this phenomenon has been observed and exploited in different domains and in various systems characterized by asymmetry and non-equilibrium. The most known examples in the research fields include: the motion of liquid droplets on hot metallic asymmetrical surfaces [2], the biological molecular transport in systems such as proteins and bacteria [3] and the Feynman-Smoluchowski Ratchet Device [1].
Marian Smoluchowski (in 1912) and Richard Feynman (in 1962) were the first to discuss about the Ratchet Effect in the thermal and statistical physics domain [1]. The idea of Ratchet was illustrated by a simple machine which called the Feynman-Smoluchowski Ratchet Device or the Brownian Ratchet Device. This device, shown in Figure 1, consists of a gear connected to a pawl that forces the gear to rotate only in one direction. A paddle wheel is connected to the gear by an axle and the overall system is immersed in a fluid of molecules at thermal equilibrium. According to the second law of thermodynamics, this device will not rotate without the presence of an external source of energy.
Therefore, the basic conditions in order to generate the Ratchet motion can be concluded by observing the Feynman-Smoluchowski Ratchet model, as well as the other examples producing the Ratchet flow. The first condition is the presence of **spatial inversion asymmetry** and the second one is the presence of a **source of external energy**

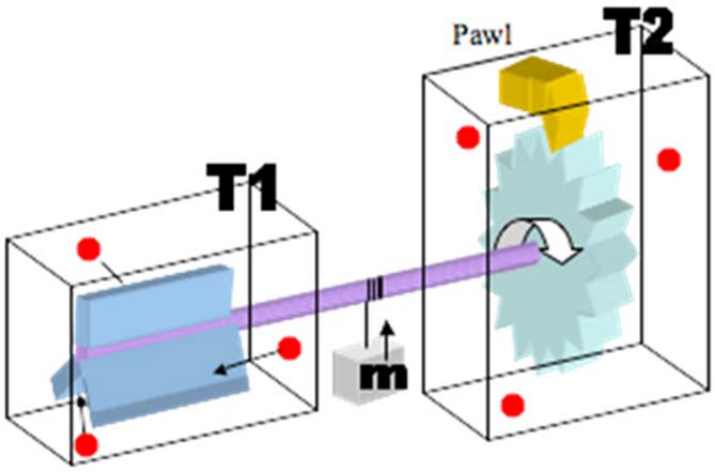


Figure 1: Schematic of the Feynman-Smoluchowski Ratchet Device.

1.2 SOME EXAMPLES OF RATCHET EFFECT IN DIFFERENT DOMAINS

H. Linke *et al.* [2] have reported that liquid droplets perform self-propelled motion when they are placed on hot surfaces with asymmetric topology (sawtooth shaped substrate), as shown in Figure 2. This phenomenon has been considered as a Ratchet Effect. The liquid motion is due to a viscous force caused by the vapor flow between the solid and the liquid. This effect has been observed for all liquids they have investigated (nitrogen, acetone, methanol, ethanol, water, and hexadecane) over a wide range of temperature.

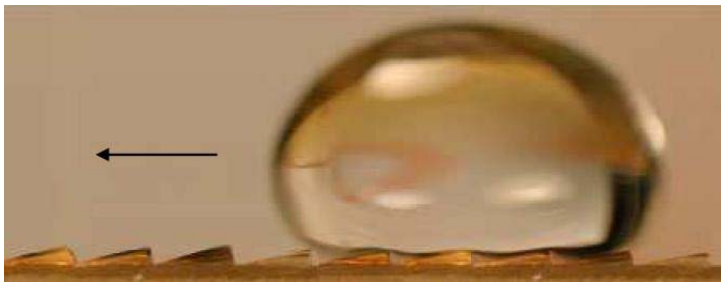


Figure 2: Photo showing the motion of water droplet on asymmetric surface [5].

R. Ait-Haddou and W. Herzog [3] have explained the link between the Brownian Ratchet theory and the biomoleular motors. Biomolecular motors are proteins that convert chemical energy into mechanical motion. These motors generate motion by rectifying the thermal random fluctuations that exist in an anisotropic system. The chemical energy causes the disequilibrium of the system and thus it can produce work from the thermal fluctuations.

1.3 RATCHET DEVICE BASED ON SEMICONDUCTOR HETEROSTRUCTURES AND ITS APPLICATIONS

Semiconductor heterostructures allow the formation of a two-dimensional electron gas (2DEG) characterized by a high electron mobility. Recently [4-10], Ratchet transport of electrons has been observed in AlGaAs/GaAs [5-7] and Si/SiGe [8-10] heterostructures samples that satisfy the cited Ratchet conditions. In such samples, the **spatial inversion asymmetry** condition has been achieved by patterning a periodic array of semi-discs shaped nanoantidots in a hexagonal lattice (by using electron beam lithography). Also, the **source of external energy** condition has been satisfied by radiating the studied sample with a linearly polarized microwave radiation at high frequency. Therefore, the electrons scatter with the antidots and move in one direction due to the effect of the microwave linear polarized radiation and due to the asymmetry of the antidots shape (semi-discs) [11-14].
A third condition that has to be satisfied in these semiconductor samples is that the **period and the radius of antidots must be smaller than the mean free path of electrons**[1] **at the working temperature** [12, 14]. Realizing this condition enhances the electrons to collide with the antidots lattice whilst reducing the interaction between electrons. This third condition can be guaranteed by working at low temperature and by reducing the antidots size to the nanoscale pattern [5-10]. Moreover, the antidots lattice has to be hexagonal to avoid the presence of regions of small collisions with antidots. Figure 3 illustrates how to compute the lattice parameters.

1 The mean free path is the average distance a particle covers before colliding with another particle [1].

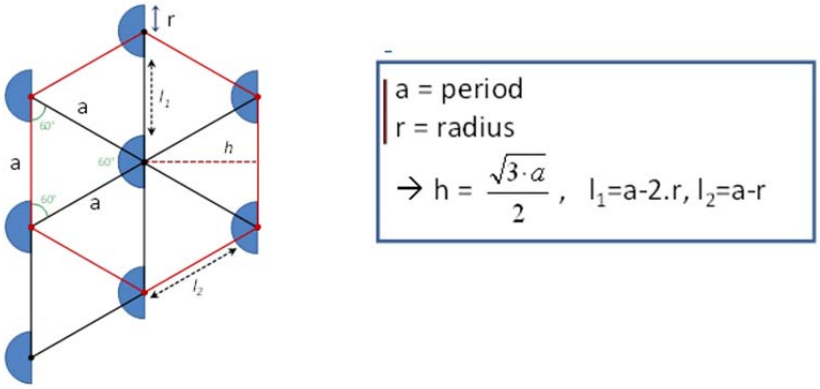


Figure 3: Schematic of the hexagonal lattice parameters.

As a result, a directed Ratchet transport of electrons has been found and thus an induced DC Ratchet photovoltage of few milli-volts has been measured between the sample contacts at low temperature [5-10].
Another important feature of the Ratchet Effect is that the sign of the induced photovoltage could be controlled by selecting the polarization of the microwave radiation. This feature has been predicted by theoretical studies [11-14] and has been confirmed by practical experiments on AlGaAs/GaAs heterojunction samples [5-7]. This dependence of the Ratchet photovoltage on the microwave polarization has not been observed in Si/SiGe heterojunction samples [9].
The Ratchet Effect has been also observed when radiating semiconductor heterostructures by terahertz radiation. Experimental and theoretical analysis have been performed in [15] on GaN/AlGaN and in [16] on AlGaAs/GaAs with a lateral periodic potential. Therefore, a Ratchet Device can be considered as a solution to generate a DC voltage from electromagnetic fields over a distance and hence to feed wirelessly microcircuits. It opens new perspectives in the fabrication of current generators and electromagnetic field detectors in the nanoscale level that can work at the microwave frequency, with the interesting possibility of using the millimeter wave and the terahertz radiation.

1.3.1 *Ratchet Device based on AlGaAs/GaAs heterostructure*

The first experiments on AlGaAs/GaAs heterostructure [5-7] have been performed by CNRS-LNCMI laboratory in Grenoble, under the direction of Prof. J.-C. Portal (ANR project coordinator). Figure 4 shows a design and an AFM image of one of the samples used in the measurements. The device has a 2DEG at a depth of 117 nm below the surface.The array of semi-discs antidots has been patterned with a depth of 54 nm in the middle of one of the three Hall bars fabricated on the sample with the dimensions of 250 µm × 50 µm. The antidots period is 1.5 µm and the antidots radius is 0.5 µm. An array of circular antidots has been fabricated in the second Hall bar, while a 2DEG in the third Hall bar has been left unpatterned, without antidots.
The sample studied by S. Sassine et al. [5-7] has been exposed to low magnetic fields and a large temperature range (1.4 to 100 K) in order to perform the magnetotransport and the photovoltage measurements. Also, the sample has been radiated with microwave energy using a tunable microwave carcinotron in the 33-50 GHz frequency range.

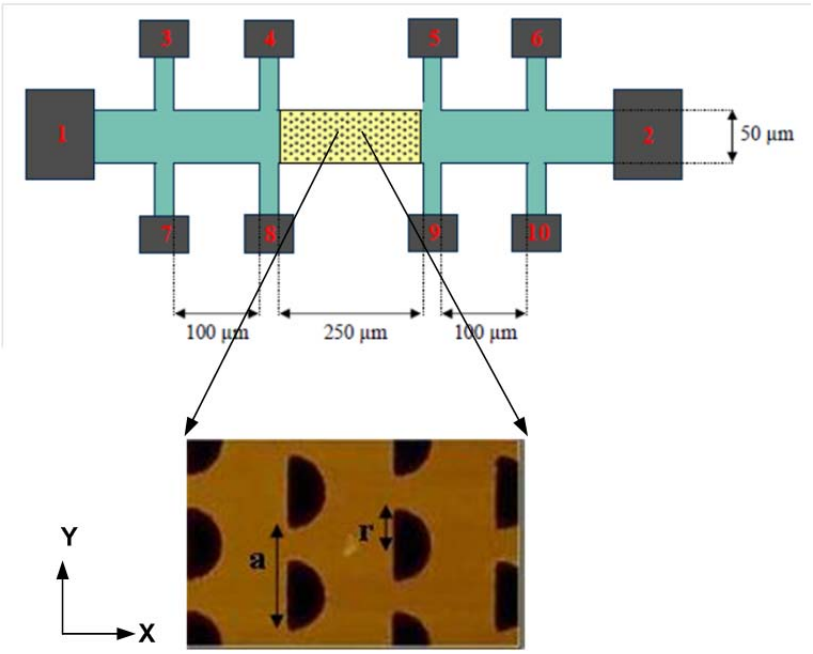


Figure 4: Design and AFM image of AlGaAs/GaAs sample with a period a = 1.5 µm and a radius r = 0.5 µm, patterned in the middle of the three Hall bars [5].

Before measuring the induced Ratchet photovoltage, LNCMI team performs some logical process in order to test the quality of the studied samples:

1) *2DEG quality*: it can be ensured by measuring the sample mobility, the quantum Hall effect and the Shubnikov de Haas oscillations. At low temperature and low magnetic field, the Hall resistance is the transversal resistance measured between two contacts when using the microwave radiation. While the Shubnikov de Haas oscillations are presented when measuring the longitudinal resistance between two contacts without using the microwave radiation.

2) *Interaction of the microwave radiation with the 2DEG*: this can be tested by measuring the MIRO's, Microwave Induced Resistance Oscillations. At low temperature and low magnetic field, these oscillations are presented when measuring the longitudinal resistance between two contacts while using the microwave radiation.
The measured Hall resistance, the Shubnikov de Haas oscillations (SdH) and the MIRO's are shown in Figure 5.

3) *Antidots definition*: in order to determine the shape and the dimensions of the antidots, the commensurability curve is extracted. Commensurability peaks (Figure 6) must be well defined to ensure the electrical conduction quality around the antidots and their dimensions. At low temperature, low magnetic field and low current injection, these oscillations are presented when measuring the longitudinal resistivity between two contacts while using the microwave radiation.

4) *Parasitic effects*:

- Contacts resistance: this could be achieved by injecting current between two pairs of contacts and measuring the resistance (for example between contacts 4 and 5 in Figure 4), this resistance should be the same while inverting the current injection.

- Parasitic voltage: while applying the microwave radiation, the Ratchet photovoltage has to be generated only between two pairs of contacts which are horizontal to the plane

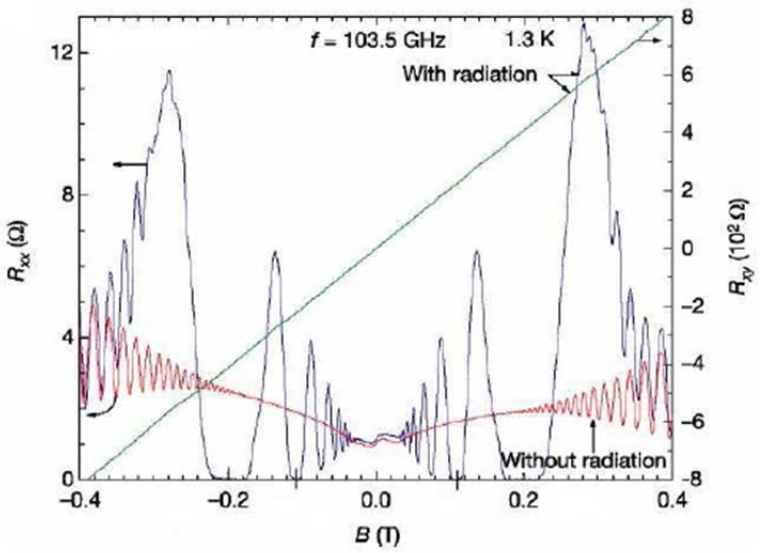


Figure 5: Longitudinal and transversal magnetoresistance measured at low temperature: Red curve is the SdH (B vs Rxx), without microwave radiation. Blue curve is the MIRO's (B vs Rxx), with microwave radiation. Green line is the Hall resistance (B vs Rxy), with microwave radiation [5].

of the semicircular antidots (for example between contacts 4 and 5 in Figure 4). No voltage has to be produced between two pairs of vertical contacts or it will be considered as a parasitic voltage. Therefore, the voltage value between two pairs of vertical contacts (for example between contacts 4 and 8 in Figure 4) is checked where it is supposed to be 0 V. Figure 7 shows the dependence of the DC induced photovoltage on the magnetic field applied on the AlGaAs/GaAs sample at a frequency of 42.7 GHz and a temperature of 1.5 K. The microwave power on the sample surface is estimated to be 20 µW.

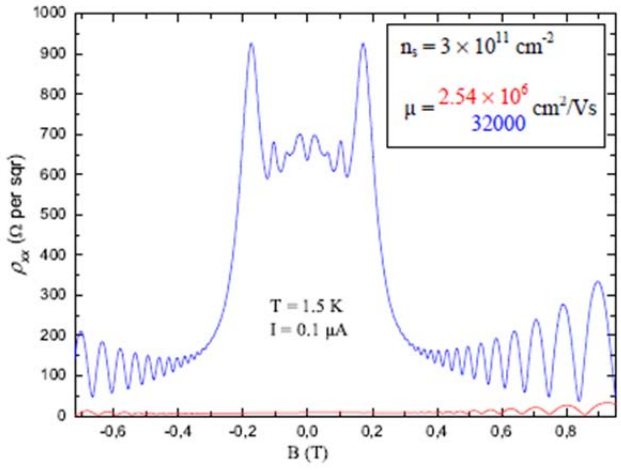


Figure 6: Longitudinal magnetoresistivity measured at low temperature. Blue curve is for circular antidots. Red curve is for pure 2DEG [5, 6].

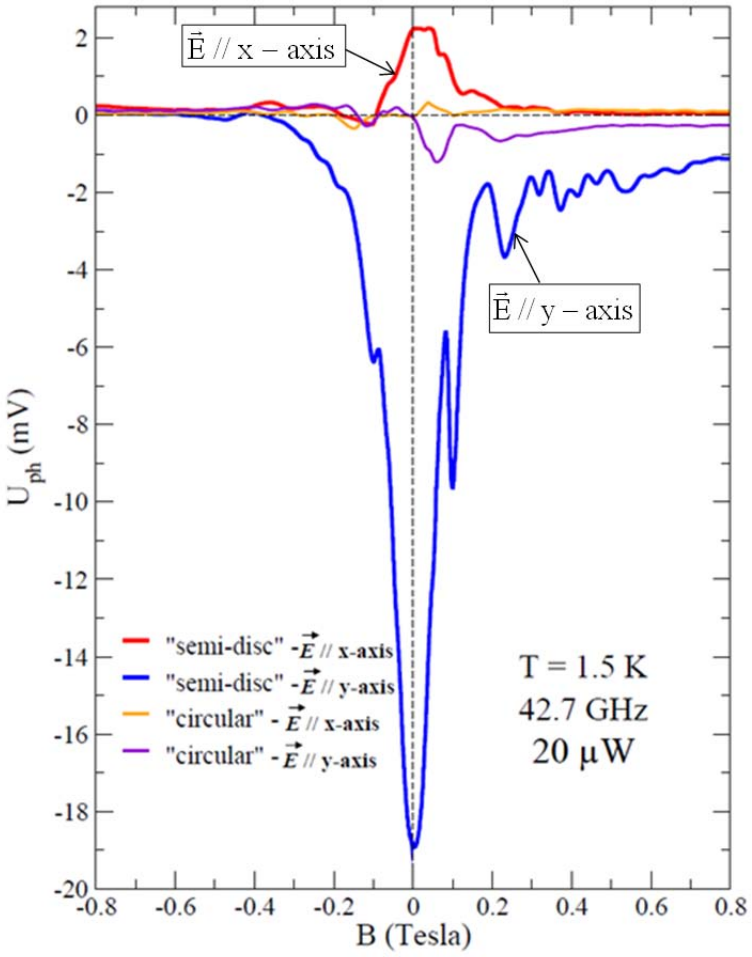


Figure 7: Induced photovoltage measured when applying a magnetic field on circular and semicircular antidots for two different microwave polarizations [5, 6].

According to the theoretical studies [11-14], when the electric field is oriented along the y-axis ($\vec{E}$ // y-axis), it forces the electrons to oscillate vertically and so they scatter with the semicircular side of the antidots. This leads the electrons to move to the right and thus it produces a Ratchet voltage with negative sign. On the other hand, when the electric field is oriented along the x-axis ($\vec{E}$ // x-axis), it forces the electrons to oscillate horizontally and they scatter with the plane side of the antidots. This leads the electrons to move to the left and thus it produces a Ratchet voltage with positive sign. This dependence on the electric field polarization is summarized by equation 1.1:

$$\psi = \pi - 2\theta \tag{1.1}$$

where ψ is the angle between x-axis and the direction of the electron transport and θ is the angle between x-axis and the direction of the radiation force. θ equals zero when $\vec{E}$ is parallel to the x-axis and it equals $\pi/2$ when $\vec{E}$ is parallel to the y-axis.
It is clear from Figure 7 that the Ratchet photovoltage is reduced for circular symmetrical antidots (almost zero for $\vec{E}$ // x-axis) compared to the photovoltage measured in case of

semi-discs antidots, which proves the necessity of having andidots with asymmetrical shape. It has been noticed that the Ratchet photovoltage has a maximum value at zero magnetic field, while for high magnetic fields (B > |0.2| T), the Ratchet Effect vanishes. This is due to the electron cyclotron orbits[2] radius which is smaller than the antidots period at high magnetic field and thus preventing the electrons from scattering with the antidots.
Figure 8 shows the dependence of the DC induced photovoltage on the temperature when the sample is at zero magnetic field and a frequency of 42.7 GHz. The microwave power on the sample surface is estimated to be 20 µW.
As we can see the Ratchet photovoltage exists at low temperature but it vanishes at high temperature, for T > 70 K. In fact, at T = 1.5 K, the mean free path of electrons is equal to 19 µm [6] which is greater than the antidots period (1.5 µm). This means that the Ratchet condition is satisfied. On the other hand, when T = 70 K, the mean free path of electrons is equal to 1.7 µm which is comparable to the antidots period and thus the electrons do not scatter with the antidots. This figure shows also the decrease of the electron mobility for the patterned (Ratchet) and the unpatterned (2DEG) regions when the temperature increases.

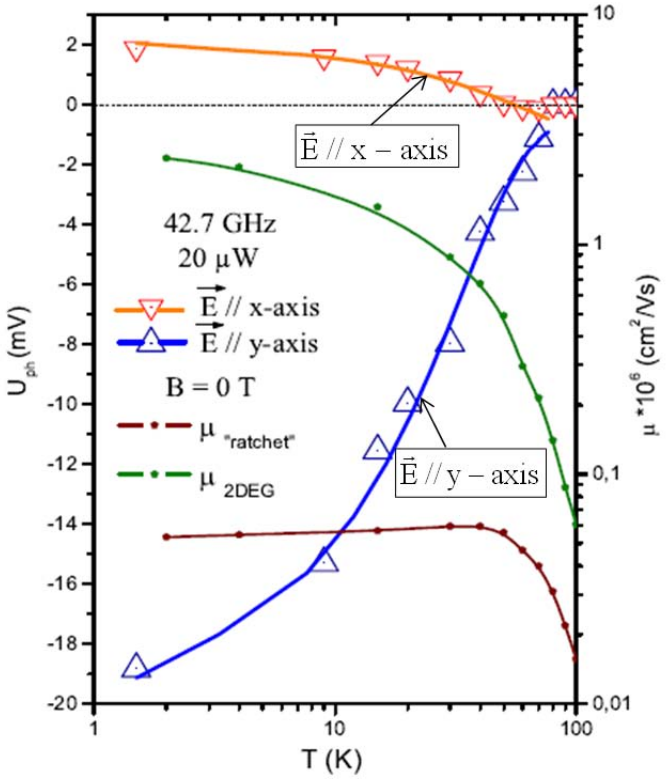


Figure 8: Induced photovoltage (for two different microwave polarizations) and electron mobility (for semicircular antidots and 2DEG) for large temperature range [5, 6].

LNCMI team has also observed a dependence of the induced Ratchet photovoltage on the microwave output power of the generator used in the experiments. As shown in Figure 9,

2 Electron cyclotron resonance is a phenomenon observed when an electron is in a static and uniform magnetic field, it will move in a circle due to the Lorentz force. The circular motion may be superimposed with a uniform axial motion, resulting in a helix, or with a uniform motion perpendicular to the field, resulting in a cycloid [17].

this dependence is quasi-linear and the photovoltage increases with the increase of the microwave output power, which has been expected by theory [12]. At zero magnetic field, this measurement has been performed for T = 1.5 K and the frequency = 42.7 GHz.

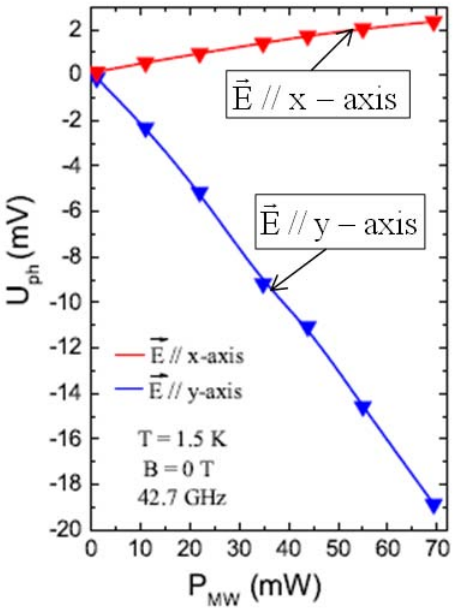


Figure 9: Induced photovoltage measured when varying the output microwave power for two different microwave polarizations [5, 6].

1.3.2 *Ratchet Device based on Si/SiGe heterostructure*

Most of the microelectronic technology for integrated circuits is based on silicon (Si) since it is a cheap semiconductor and available in large quantities. Contrariwise, the first transistor was fabricated from germanium (Ge) since it has higher electron mobility than silicon. Therefore, the study of the Si/SiGe heterostructure properties becomes necessary in the microelectronic domain as Si/SiGe has better qualities than silicon while allowing the use of the standard equipments used in manipulating silicon. This increases the product quality and reduces the cost of renewing the production machines.
Since Si/SiGe has shown interesting material properties, it has been proposed to be adopted in the fabrication of the Ratchet Device. Several samples have been characterized and measured by LNCMI team, under the direction of Prof. J.-C. Portal, in order to investigate the Si/SiGe samples performances.
In the sample studied by I. Bisotto *et al*. [9], a semicircular antidots lattice with the dimensions of 80 µm × 50 µm has been patterned in one of two Hall bars fabricated on each side of the sample, as shown in Figure 10. A lattice with circular antidots has been patterned on the other side, while the area of the pure unpatterned 2DEG has been made at the middle of the sample with the dimenions of 250 µm × 50 µm. The antidots period is 0.6 µm and the antidots radius is 0.2 µm.
Figure 11 shows the magnetotransport and the photovoltage measurements when the sample is radiated by a microwave source at a frequency of 50 GHz. These measurements demonstrate that the Ratchet Device based on Si/SiGe has approximately the same

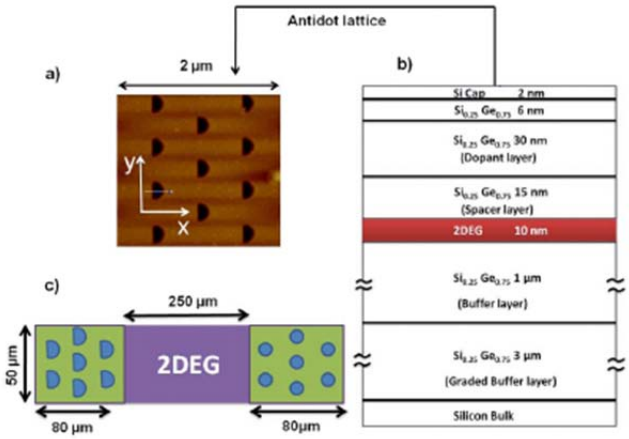


Figure 10: (a) AFM image of Si/SiGe sample with a period a = 0.6 µm and a radius r = 0.2 µm. (b) Schematic of the Si/SiGe heterostructure layers. (c) The dimensions of the three Hall bar fabricated on the sample [9].

behavior of the sample based on AlGa/GaAs discussed before. In Figure 11(a), we can observe an induced photovoltage in case of pure 2DEG and circular antidots. According to [9], this could be due to the photovoltage change generated in the semicircular antidots when a magnetic field is applied that produces a charge gradient in the entire 2DEG of the sample. This behavior was also observed in the studied AlGaAs/GaAs sample (Figure 7).
However, three main differences could be underlined between the experimental results of the Si/SiGe and the AlGaAs/GaAs samples.

i. The first one is that the maximum value of the measured photovoltage in case of AlGaAs/GaAs (around 20 mV) is greater than the photovoltage measured in case of Si/SiGe (around 3 mV).

ii. The second difference is that the maximum induced photovoltage is observed at B = -0.2 T for the Si/SiGe (Figure 11(a)), while it is observed at B = 0 T in case of AlGaAs/GaAs (Figure 7).

iii. The third difference is that the sign of the induced photovoltage is independent of the microwave polarization in case of the Si/SiGe sample. When the electric field is parallel to the x-axis or the y-axis, the sign of the Ratchet photovoltage remains negative (Figure 11(b)), which is different in the case of the AlGaAs/GaAs sample. The shift of the maximum photovoltage and the independence of its polarity on the microwave polarization could be due to the strong electron-electron interactions in the Si/SiGe heterostructures when a magnetic field is aaplied [9, 18].

Figure 12 shows the mangnetotransport of another Si/SiGe sample studied by E. S Kannan *et al.* [10]. It has been noticed that the maximum value of the photovoltage is also shifted toward negative B for different temperatures. The semicircular antidots have been patterned on the middle of a 250 µm × 50 µm Hall bar, while a 2DEG has been left unpatterned on each side of the sample with the dimensions of 100 µm × 50 µm. The antidots period is 600 nm and the antidots radius is 120 nm.
After studying the influence of the magnetic field, the temperature and the microwave power on the value of the generated photovoltage at a certain frequency, a study of the

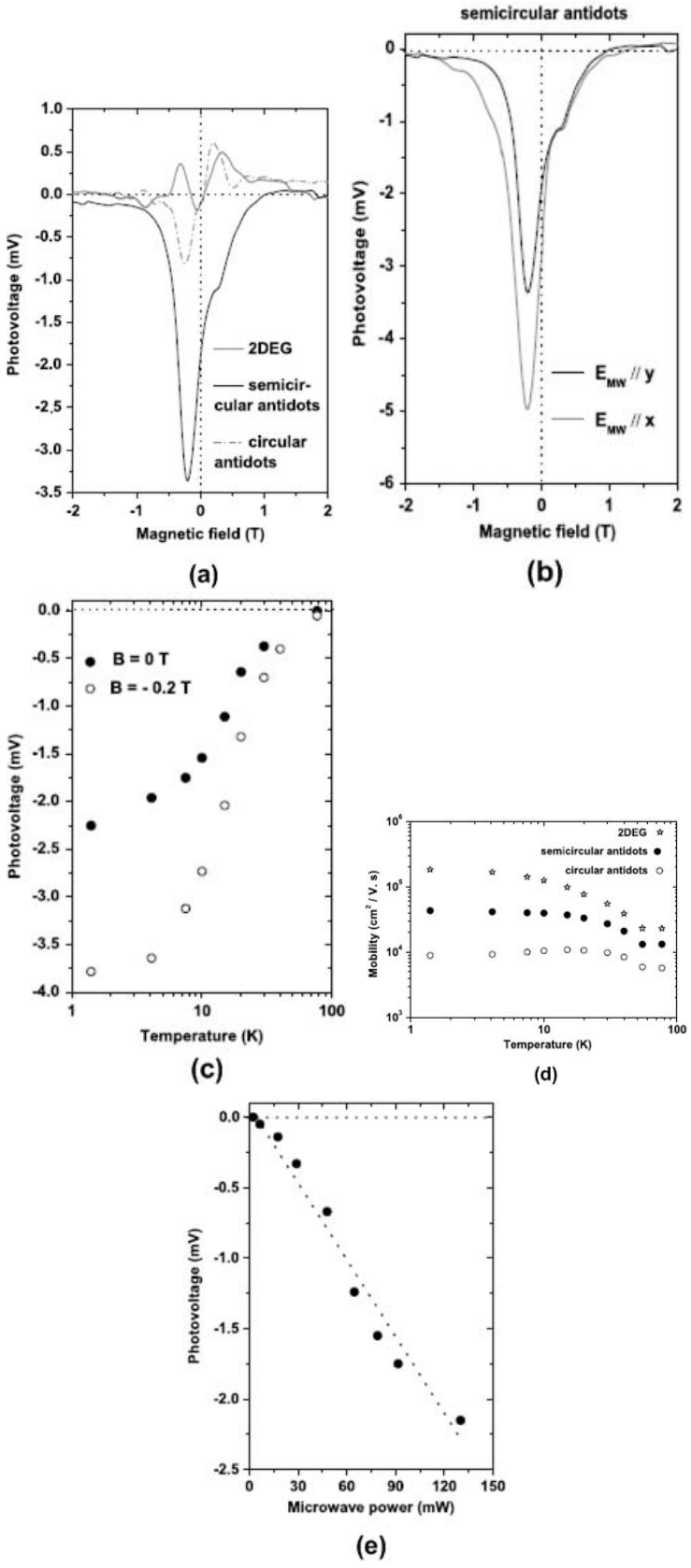


Figure 11: (a) Induced photovoltage measured when applying a magnetic field on 2DEG, circular and semicircular antidots (b) for two different microwave polarizations. (c) Induced photovoltage measured for large temperature range. (d) Electron mobility measured (for 2DEG, semicircular and circular antidots) for large temperature range. (e) Induced photovoltage measured when varying the output microwave power [9].

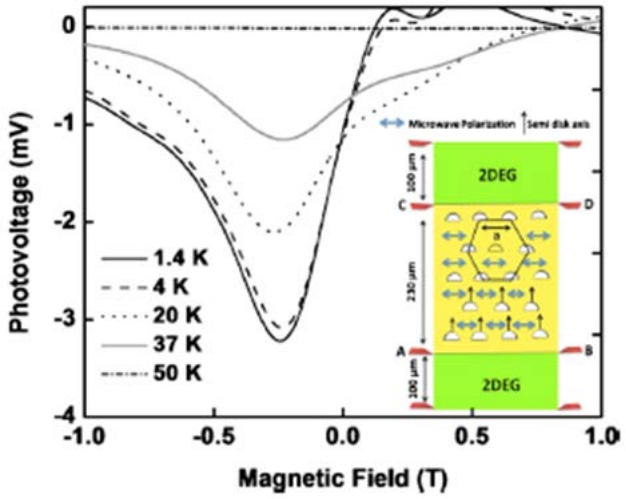


Figure 12: Induced photovoltage measured when applying a magnetic field for different temperatures. Inset is a schematic of the Hall bar dimensions in which a 2DEG and semicircular antidots have been fabricated [10].

dependence of the photovoltage on the microwave frequency has been performed. The studied sample is based on a Si/SiGe heterojunction with an antidot radius of 200 nm, a period of 600 nm and a not perfect hexagonal lattice. The sample has been kept at a temperature of 4 K and has been radiated with a microwave power of 30 dBm (power level at the microwave generator output). Figure 13 reports the photovoltage curves obtained at different frequencies, when varying the magnetic field from -2 to +2 T.
The results show that the photovoltage value changes with respect to the frequency: the peak value of the photovoltage at f = 36.71 GHz is larger than the one observed at f = 29.23 GHz. When B = 0 T, the photovoltage at f = 36.71 GHz is approximately double the value measured at f = 37.35 GHz. However, due to the complexity of the metallic setup used in this type of measurements (described in details in chapters 2 and 3), the influence of the setup on the sample response has not been experimentally clarified. Therefore, some electromagnetic simulations have been performed showing that the electric field distribution changes inside the cavity of the cryogenic system for different microwave frequencies and thus this could affect the measured photovoltage. Furthermore, according to the theoretical studies in [13], the Ratchet velocity is independent of the microwave frequency for $\omega r_d/V_F \ll 1$, where ω is the angular frequency, r_d is the antidot radius and V_F is the Fermi velocity of 2DEG. The electromagnetic study of the influence of the operating frequency on the response of the used setup will be presented in details in chapter 3.

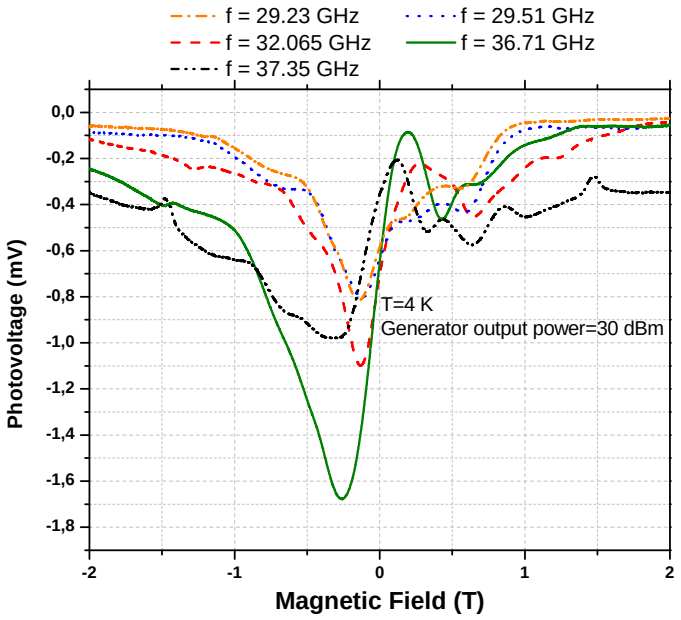


Figure 13: Induced photovoltage measured when applying a magnetic field for different microwave frequencies, at T = 4 K and a power level of 30 dBm at the microwave generator output.

1.3.3 *Other research works performed on Ratchet Device based on heterostructures*

Besides the research work of LNCMI team that was presented in the previous sections, recent studies on Ratchet Effect have been performed by other research groups and will be summarized in this section.
W. Weber *et al*. [15] have observed a Ratchet photocurrent induced by terahertz radiation in GaN/AlGaN heterojunction. At room temperature, the studied sample has a mobility of $\sim 1200\,cm^2V^{-1}s^{-1}$and an electron density of $\sim 10^{13}\,cm^{-2}$. The sample has been radiated with an optical excitation of laser with pulses duration of $\sim 100\,ns$ and with wavelengths of λ = 77 µm, 90.5 µm, 148 µm, 280 µm, 385 µm and 496 µm. As a result, a photocurrent of several nA has been obtained at room temperature. Experimental and theoretical analysis has been performed by this team to study the photocurrent polarization properties as a function of the incidence angle of radiation. The current has been measured at oblique incidence and a small current has been detected at normal incidence.
The observation of Seebeck[3] Ratchet Effect has been reported by P. Olbrich *et al*. [16] in semiconductor heterostructures with one-dimensional array of lateral asymmetric grooves excited by terahertz radiation. The effect of the periodic grooves is that they modulate the intensity of the incident light, due to near field diffraction and thus the light is spatially periodic in the 2DEG plane. The modulated light causes a periodic modulation of the effective electron temperature, hence this Ratchet Effect is based on a spatial modulation of the temperature and it is called Seebeck Ratchet. The studied sample is a GaAs/AlGaAs heterojunction with an electron mobility of $\sim \sim 5 \times 10^6\,cm^2V^{-1}s^{-1}$a and a carrier density of $\sim 2 \times 10^{11}\,cm^{-2}$ at a temperature of 4.2 K. At room temperature, the mobility is reduced to $\sim 6 \times 10^3\,cm^2V^{-1}s^{-1}$ and the carrier density is $\sim 1.2 \times 10^{11}\,cm^{-2}$. The width of the grooves is 0.5 µm with a period of 2.5 µm. The photocurrent of several

3 The Seebeck Effect is the conversion of temperature differences to an induced thermoelectric voltage [19].

µA is produced at room temperature (T = 300 K) and at T = 10 K, for an optical excitation of NH_3 laser operating at a wavelength λ = 280 µm, with a power of ~ 2 KW and a pulse duration of ~ 100 ns. It has been noticed that when decreasing the temperature, the photocurrent increases.
The obtained experimental results have been compared to the results obtained from an unpatterned reference sample. It has been observed that the photocurrent is maximal at normal incidence in the patterned sample, however in the reference sample; the signal vanishes under normal incidence.
In the previous research papers discussed above, the heterostructures samples have been excited using terahertz radiation. C. Drexler *et al*. [20] have reported the generation of a spin polarized current in semiconductor heterostructures samples under microwave radiation, when the samples are exposed to an external in-plane magnetic field. The reason of the current generation is due to the Zeeman[4] splitting of the subbands in the magnetic field which converts the current spin flow into a spin polarized electric current.
Two types of samples have been used in this study: (i) (Cd, Mn)Te/(Cd, Mg)Te and (ii) InAs/(In, Ga)As heterostructures. At T = 4.2 K, the 2DEG of the first sample has a mobility of $\sim 1.6 \times 10^4\ cm^2V^{-1}s^{-1}$ and a carrier density of $\sim 6.2 \times 10^{11}\ cm^{-2}$. At the same temperature, the second sample has a 2DEG mobility of $7 \times 10^4\ cm^2V^{-1}s^{-1}$ and a carrier density of $1 \times 10^{12}\ cm^{-2}$.
These samples have been subjected to an in-plane magnetic field (By) with a strength of 5 T and a variable temperature from 1.8 to 150 K. Two Gunn oscillators, operating at frequencies of 95.5 or 60 GHz, have been used to generate the microwave radiation. A horn antenna and two parabolic mirrors have been used to guide the microwave radiation to the sample. The incident power has a value of 0.1 mW and has been modulated at a frequency of 970 Hz.
For the two studied samples, the current increases with the magnetic field By. However, two different behaviors have been observed with the temperature variation. For the (Cd, Mn)Te/(Cd, Mg)Te sample, when the temperature increases, the current value decreases and it changes its sign at T = 20 K. For the InAs/(In, Ga)As sample, the current decreases too with the rise of temperature but its sign does not change.

1.4 RATCHET DEVICE BASED ON GRAPHENE

As discussed in the previous sections, the Ratchet Device based on semiconductor heterostructures can only work at low temperature. Therefore, the use of a complex cryogenic metallic system is necessary to keep the studied sample at low temperature which is not practical for the Ratchet Device applications. Nowadays, the properties of graphene have attracted the research attention, as a new two-dimensional electron gas system with high mobility at room temperature, which makes the graphene suitable to fabricate a Ratchet Device.
Several fabrication trials of Ratchet Device based on graphene layers have been performed in CNRS-LAAS. The samples design and characterization, the experimental setup used in measurements and the obtained results will be presented in details in chapter 5.

4 The Zeeman Effect is the effect of splitting a spectral line into several components in the presence of a static magnetic field [21].

1.5 CONCLUSION

This chapter provided a general overview of the Ratchet Effect concept, including a brief summary of different recent research efforts performed to fabricate a well characterized Ratchet Device acceptable for several interesting applications. In the domain of physics, we can conclude that there is one general concept of the observed phenomenon which is the generation of Ratchet electrons movements when exciting a semiconductor heterostructure sample with a broken spatial symmetry. However, the properties of the generated transport of electrons differ from one studied sample to another depending on many factors:

- The type of the semiconductor materials forming the heterojunction (e.g. AlGaAs/-GaAs, Si/SiGe, etc.).
- The radiation used to excite the studied sample (e.g. microwave, terahertz, etc.).
- The way of breaking the system spatial symmetry (e.g. semi-discs antidots, lateral asymmetric groov, etc.).
- The shape and the dimensions of the lattice containing the periodic asymmetric scatterers.
- The experimental conditions (i.e. the temperature, the magnetic field, the experimental setup, etc.).

In the following chapters (chapters 2 and 3), the first part of this thesis will be presented which consists of studying the electromagnetic behavior of the experimental setup used in the measurements done by LNCMI team. This study is based on intensive electromagnetic simulations and some indirect measurements that show the great impact of the experimental setup on the induced photovoltage measured.

2

ELECTROMAGNETIC ANALYSIS OF THE EXPERIMENTAL SETUP FRONT-END MODULE USED TO INVESTIGATE THE RATCHET EFFECT

2.1 INTRODUCTION

This thesis work has been progressed based on a certain methodology in order to study the Ratchet Effect and to optimize the experimental setup from the electromagnetic point of view. The methodology steps can be presented as follows:
Step 1. A good understanding of the physical phenomenon and of the future applications based on it.
Step 2. Determination of the experiment conditions and studying the experimental setup used in observing the phenomenon.
Step 3. Developing simple electromagnetic simulations models of the setup, and then increasing the complexity of the models structure to be as close as possible from the actual setup.
Step 4. Finding analytical equations that define the phenomenon and thus enhancing the system response.
Step 1 was discussed in the previous chapter. However, this chapter describes the front-end module of the experimental setup that has been used in studying the Ratchet Effect and in obtaining the measurements results [5-10] presented in the previous chapter. An electromagnetic analysis has been perfomed to optimize the electromagentic behavior of this setup and hence to improve the Ratchet photovoltage obtained. Moreover, different RF techniques will be proposed in this chapter that can be used to radiate the studied samples and to control the Ratchet Effect at room temperature. A comparative performance study between the proposed techniques, based on full wave electromagnetic simulations, will be presented. This study allows identifying the most suitable techniques for enhancing the Ratchet experimental setup.

2.2 DESCRIPTION OF THE EXPERIMENTAL SETUP

The second step of the methodology is to have a good study of the experimental setup. This complex setup exists in CNRS-LNCMI and has been used to study the Ratchet Effect on semiconductor samples. Figure 14(a) shows a photo of the whole system and Figure 14(b) is a schematic to clarify each part of the system. A tunable microwave carcinotron, in the 33–50 GHz frequency range, represents the source of the microwave linear polarization; and an attenuator is connected to the carcinotron output to control the signal level. A circular waveguide with a radius of 5 mm is used to guide the microwave radiation and it penetrates the closed metallic cavity of the cryogenic system. A rectangular-to-circular waveguide transition connects the attenuator rectangular output to the circular waveguide input aperture. A second waveguide transition, circular-to-rectangular, is connected to the circular waveguide output aperture to focus the microwave energy on the rectangular sample. The rectangular aperture of the transition is a WR22 with 5.69 mm length and 2.84 mm width. The sample lies in a ceramic package and its contacts are connected to the package contacts using wire bonding (see Figure 14(c)). There are some copper wires

which connect the package contacts to the pins of three other black packages and finally to a thermal resistance. The aim of this thermal resistance is to indicate the temperature inside the closed metallic cavity. These copper wires are also connected to a voltmeter, digital multimeter with high accuracy, to measure the photovoltage produced between each two contacts of the sample.To exclude the reflection of the radiation on the sample contacts, a diaphragm composed of absorbing material is placed between the sample and the waveguide output. The diaphragm presents a rectangular slot in its center and lies on the ceramic package where the semiconductor sample is placed.

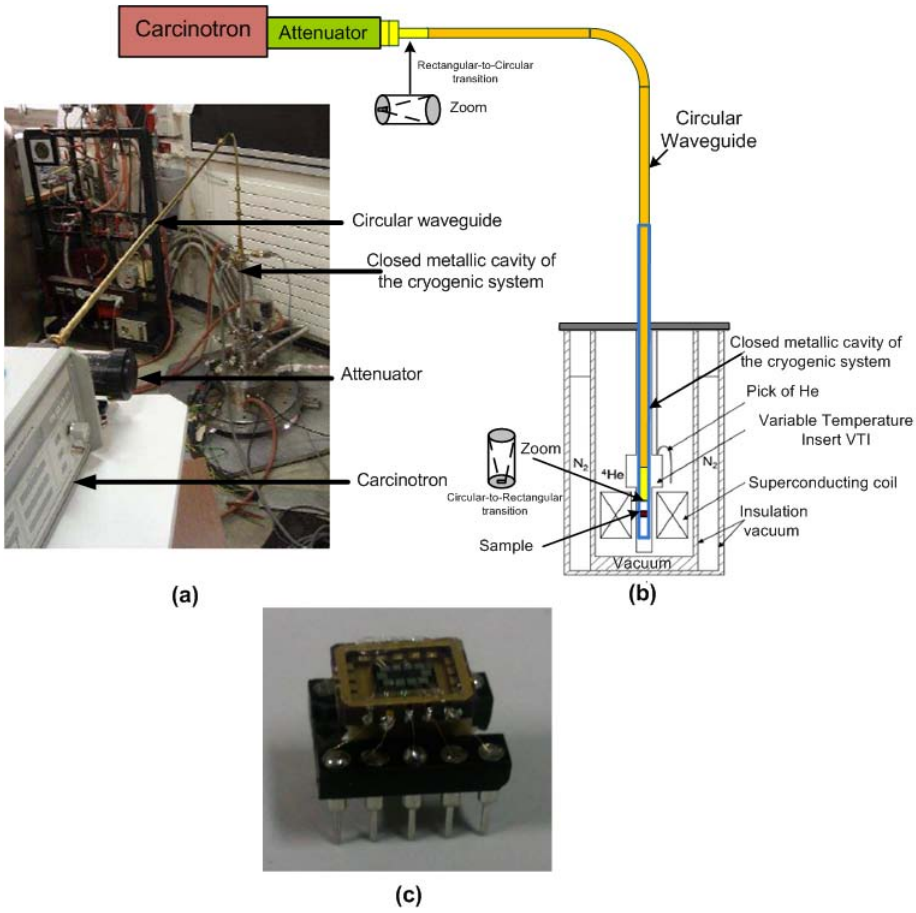


Figure 14: (a) Photo [5] of the complete experimental setup. (b) Schematic of the setup showing the different parts of the cryogenic system used. (c) Photo of the sample connected to the package using wire bonding.

2.3 ELECTROMAGNETIC SIMULATION MODEL OF THE MICROWAVE FRONT-END MODULE

Now, the third step of the methodology is to develop simple simulation models to represent the setup. The important part of this complex experimental setup is the microwave front-end module which is composed of: (i) the open-ended rectangular waveguide (WR22); (ii) the pierced diaphragm placed between the end of the WR22 and the sample; (iii) the sample itself with its package. In this section, the proposed simulation model

for the front-end module is presented, while increasing the complexity of the simulation models to represent the complete setup will be discussed in the next chapter. Figure 15 illustrates the different parts of the simulation model reperesenting the front-end module. The diaphragm is made of absorber (ABS) material manufactured by Emerson & Cuming [22] and it is positioned at a distance d1 = 1.5 mm from the end of the WR22 section. The length and width of the rectangular diaphragm slot are c_x and c_y = c_x/2 = 1.5 mm respectively and its thickness is 0.762 mm. Since exact materials parameters (relative permittivity ε_r and relative permeabilityμ_r, electric and magnetic loss tangentstan $\delta_e$andtan d_m) are not available for ECCOSORB®BSR, the properties of a (supposed) equivalent material (ε_r= 10, μ_r = 1.5, tan δ_e = tan δ_m= 0.2) have been used in the simulation approach. This diaphragm is placed on the sample package and the sample is considered, in the first simulation test, as silicon homogeneous sample (not heterojunction sample and without antidots) with a thickness of 0.6 mm. A wave port has been added to represent the source of the microwave energy with the same dimensions of the WR22. The distance between the diaphragm and the sample surface d2 = 0.162 mm and the distance between the WR22 output and the sample d = 2.424 mm. To minimize the computing time, the model has been split using two symmetry planes: perfect magnetic boundary conditions (y-z plane) and perfect electric boundary conditions (x-z plane). The model is surrounded by a vacuum box with radiation boundaries.

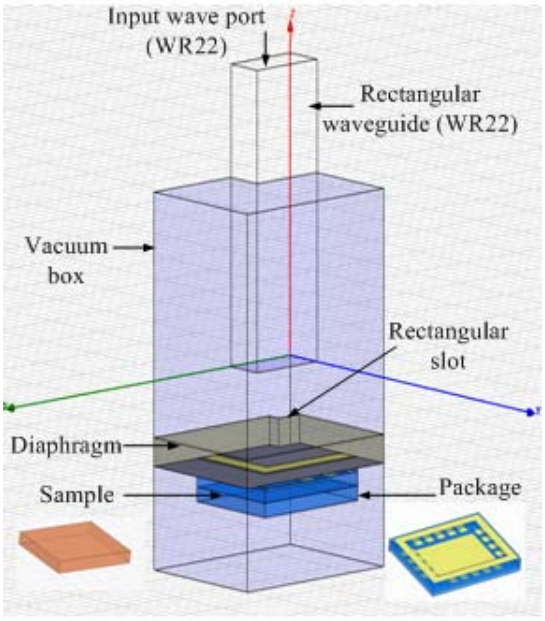


Figure 15: 3D simulation model representing the microwave front-end module of the experimental setup.

The simulations have been performed at a frequency of 42.7 GHz. The choice of this frequency is related to the experimental measurements performed on the AlGaAs/GaAs samples presented in [5-7] where this frequency value has been used. The simulation model has been developped using Ansoft HFSS electromagnetic simulator [23]. HFSS software is a full wave (rigorous) electromagnetic tool based on the Finite Element Method. It is also useful in this electromagnetic study, as it includes a fields calculator that enables us to calculate the analytical equations, presented in the next section, which quantify the Ratchet Effect.

2.4 EVALUATING THE INTRINSIC PERFORMANCE OF THE MICROWAVE FRONT-END MODULE

In this section, the fourth step of the methodology is presented which requires an electromagnetic analysis of the simulation model response. This analysis is based on electromagnetic descriptors calculated using analytical equations that define the Ratchet Effect in a simple manner. The electromagentic descriptors are (using HFSS fields calculator):

i. Calculating the value of the normalized incident electromagnetic power flow P_n across the sample surface using equation 2.1

$$P_n = \frac{100}{P_{in}} \oiint_R Real\left(\overrightarrow{P}\right) \cdot d\overrightarrow{s}\ [\%] \tag{2.1}$$

P_{in} represents the average power at the input wave port of the simulation model (HFSS uses $P_{in} = 1W$ as default value), $\overrightarrow{P}$ is the RMS Poynting vector, R is a rectangle representing the sample surface with 5 mm length and 4 mm width, and $d\overrightarrow{s}$ is the vector element of an infinitesimal area taken at the sample surface R.
The experimental results obtained by LNCMI team (Figure 8 and Figure 10(e)) have shown a direct dependence between the induced Ratchet photovoltage and the power supplied by the carcinotron. However, it appears more convenient to relate this voltage to the electromagnetic power flow across the sample surface. This can be achieved by calculating the descriptor P_n which could indicate the value of the photovoltage that could be obtained at a certain value of P_n .

ii. Calculating the uniformity of the electric field linear polarization K_E on the sample surface using equation 2.2

$$K_E = min^R \frac{\left|\overrightarrow{E_y}\right|}{\left|\overrightarrow{E_t}\right|} \times 100\ [\%] \tag{2.2}$$

$\left|\overrightarrow{E_y}\right|$ is the magnitude of the electric field y-component vector and $\left|\overrightarrow{E_t}\right|$ is the magnitude of the total electric field vector. When the electric field is oriented along the y-axis, it forces the electrons to oscillate vertically and scatter with the semicircular side of the antidots. This leads the electrons to move to the right and hence producing a photovoltage. Thus in this equation, the value of $\overrightarrow{E_y}$ is compared to the value of $\overrightarrow{E_t}$ on the sample surface. If K_E increases, this signifies that $\overrightarrow{E_y}$ is the major component of the electric field on the surface and that the electric field linear polarization is uniformly distributed on the overall sample surface to generate the Ratchet Effect. Moreover, in the practical experiments [5-7, 9], the sample is rotated 90 degrees to study the infuence of the microwave polarization

on the direction of the induced photovoltage in AlGaAs/GaAs and in Si/SiGe samples. This descriptor can also be used in this polarization study by replacing $\overrightarrow{E_y}$ by $\overrightarrow{E_x}$ in the above equation.

iii. Calculating the uniformity of the incident power density K_P on the sample surface using equation 2.3.

$$K_P = \frac{min^R \left| \overrightarrow{P} \right|}{max^R \left| \overrightarrow{P} \right|} \times 100\,[\%] \tag{2.3}$$

When comparing between the minimum and the maximum values of the RMS Poynting vector on the overall sample surface, we can test the uniformity of the electric field density. If K_P increases, this signifies that there is no large difference between the minimum and the maximum values and that the power density is uniformly distributed on the sample surface hence producing high values of the induced photovoltage.

2.5 PARAMETRIC ANALYSIS OF THE MICROWAVE FRONT-END MODULE

Varying the distance between the WR22 output and the diaphragm (d1), the distance between the diaphragm and the sample (d2), as well as, the dimensions of the rectangular diaphragm slot (c_x and c_y), changes the electromagnetic response of the front-end module. In order to perform a parametric analysis and to evaluate the intrinsic performance of the microwave front-end module, the simulation model of Figure 15 has been simplified by removing the sample packages and replacing the sample by a rectangle R to be able to compute the Ratchet descriptors on its surface. Moreover, the influence of the diaphragm material on the simualtion results has been studied by calculating these descriptors for an absorber diaphragm (ABS) and for a copper diaphragm. A part of this parametric study is published in [24, 25].

The simulation results in Figure 16 show that when d1 increases, P_n decreases while K_E and K_P are quasi-stationary for the absorber and the copper diaphragm (except some peak values in the absorber diaphragm case). The value of P_n in case of the copper diaphragm is greater than its value in case of the absorber diaphragm, which is contrary to K_E and K_P that have greater values for the asborber diaphragm.

For Figure 17, when d2 increases, P_n decreases while K_E increases for the absorber and the copper diaphragm. In case of the absorber diaphragm, K_P has a maximum value for d2 = 1.5 mm and in case of the copper diaphragm, it increases with the increase of d2. In general, it has been noticed that there is a contradiction between the normalized power flow and the uniformity of the electric field linear polarization: when the sample is far from the microwave source, the power flow decreases while the uniformity of the polarization increases.

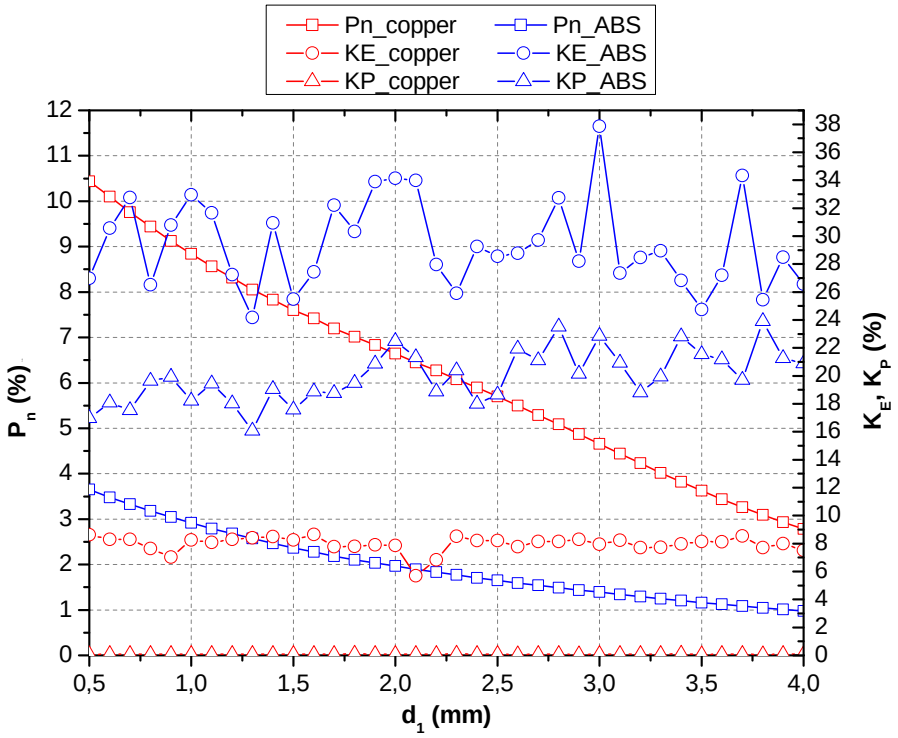


Figure 16: P_n, K_E and K_P in function of d1 and the diaphragm materials, for d2 = 0.162 mm and c_x = 3 mm.

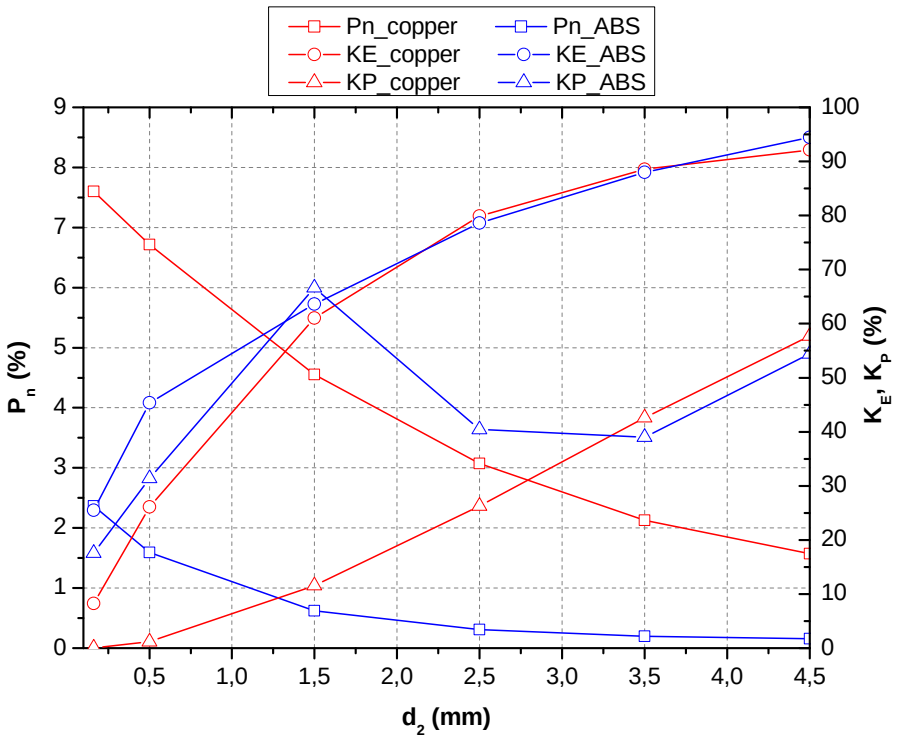


Figure 17: P_n, K_E and K_P in function of d2 and the diaphragm materials, for d1 = 1.5 mm and c_x = 3 mm.

Figure 18 presents the impact of varying the dimensions of the diaphragm slot and the diaphragm material on the simulation results. K_E and K_P show a similar behavior than the one presented in Figure 16. But in the copper diaphragm case, K_E is quasi-stationary when c_x is less than 2.8 mm, beyond this value, it becomes more stable. Concerning P_n, it shows a slow increase with increasing c_x for the absorber diaphragm and in the coper diaphragm case, there is a sort of resonance at c_x = 3.4 mm.

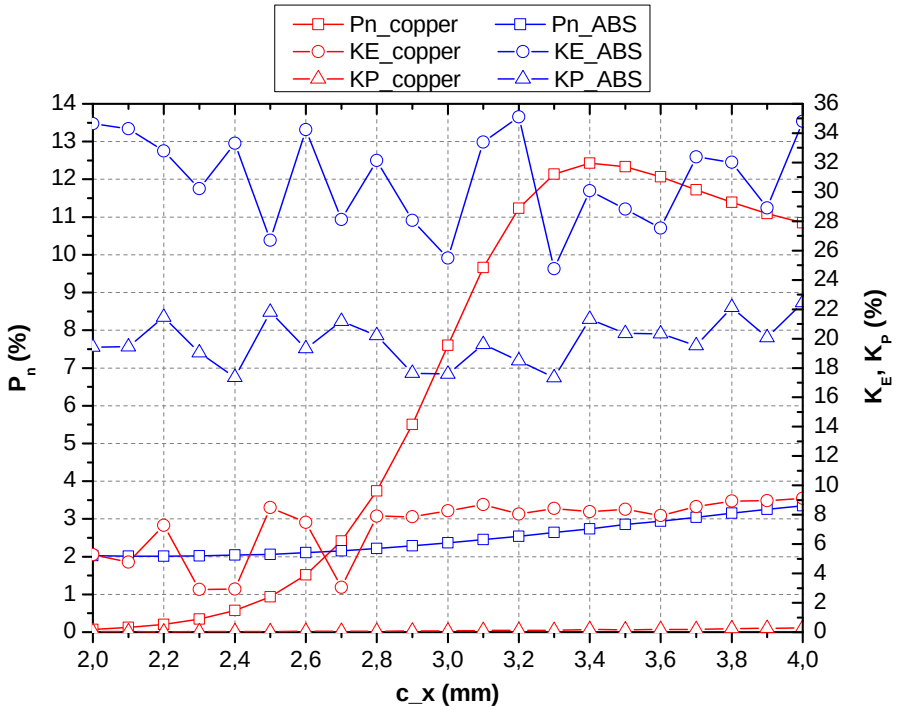


Figure 18: P_n, K_E and K_P in function of c_x and the diaphragm materials, for d1 = 1.5 mm and d2 = 0.162 mm.

2.6 EXPERIMENTAL VALIDATION OF THE SIMULATIONS RESULTS USING INDIRECT MEASUREMENTS TECHNIQUES

The presented simulation results can not be easy validated by measurements due to the small dimension of the front-end module and the complexity of the whole experimental setup with the presence of the metallic cryogenic cavity. Nevertheless, it is possible to validate, indirectly, the simulation results using a back-to-back structure. This work is published in [27].
Figure 19 presents the proposed simulation model which consists of a metallic diaphragm with a rectangular slot placed between two rectangular waveguides (WR22).
Figure 20 shows the simulated S-parameters obtained for the back-to-back structure in function of the slot size (distance between WR22 sections and the diaphragm is 3mm). These results reveal, if a metallic diaphragm is used, that the transmission coefficient (S21) has a maximum value for c_x about 3.4 mm (in agreement with the results presented in Figure 18 for a 'single' structure).

The experimental back-to-back structure used in the indirect measurements is composed of: (i) two coaxial-to-WR22 transitions from A-INFO [26]; (ii) a set of metallic diaphragms

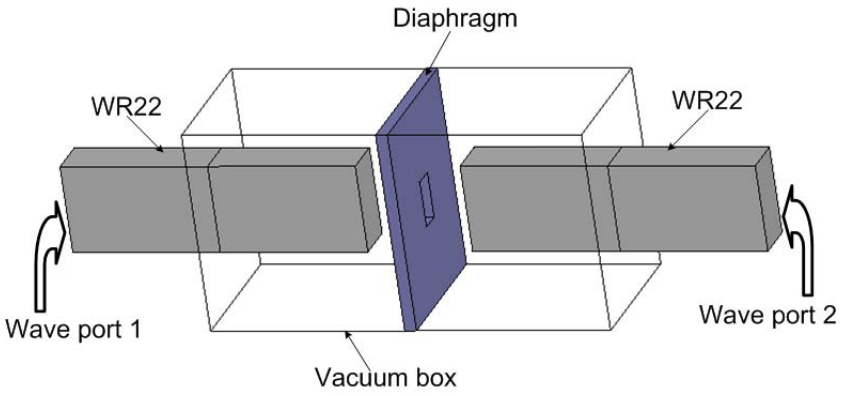


Figure 19: HFSS model of the proposed back-to-back structure.

with various slot sizes and (iii) a set of plastic pieces to control the distance between the diaphragm and the transitions. This back-to-back structure has been connected to a 37397D VNA (Vector Network Analyzer) from Anritsu [27] using flexible coaxial cables (with V connectors). Figure 21 shows a schematic and a photo of the back-to-back structure, the set of the metallic diaphragms and the plastic pieces.
Figue 22 shows the measured and the simulated reflection coefficients (S11) for the two used transitions. As shown in this figure, the difference in values between the black and the red curves, which represent the reflection coefficient of each transition, shows that these two transitions are not identical due to their intrinsic mechanical manufacturing tolerances. To overcome the negative effects of the cables and the connectors on the measurements, a standard SOLT (Short-Open-Line-Thru) calibration has been performed. The exact geometrical dimensions of the coaxial-to-WR22 transition have not been available and have been determined using non-destructive measurement techniques. The difference between the simulation and the measurement results are mainly due to the error in the determination of the exact dimensions of the transition between the coaxial feed and the WR22 waveguide (feed probe radius: 0.5 mm, feed probe height: 1.3 mm, distance between the short-end of the WR22 and the probe feed: 2 mm, length of the WR22 section: 20.8 mm).
Figure 23 shows the experimental and the simulation results of the transmission coefficient (S21) for the back-to-back transitions with the presence of a diaphragm between them (slot size: c_y = c_x/2 = 1 mm, 1.5 mm and 2 mm). To control the distance between the diaphragm and the transitions, two plastic pieces (thickness: 1 mm) have been placed from each side of the diaphragm and have been connected to the two transitions.
As shown in Figure 22 and Figure 23, a good agreement between the simulated and the measured S-parameters is obtained especially in the 42–43 GHz. Therefore, this proposed back-to-back structure has allowed to validate experimentally: (i) the impact of the variation of the distance (d1) between the WR22 end and the diaphragm on the transmission and the reflection coefficients; (ii) the impact of the variation of the diaphragm slot dimensions (c_x and c_y) on the transmission and the reflection coefficients; (iii) the agreement between the simulations and the measurements and consequently the accuracy of the proposed simulation approach.

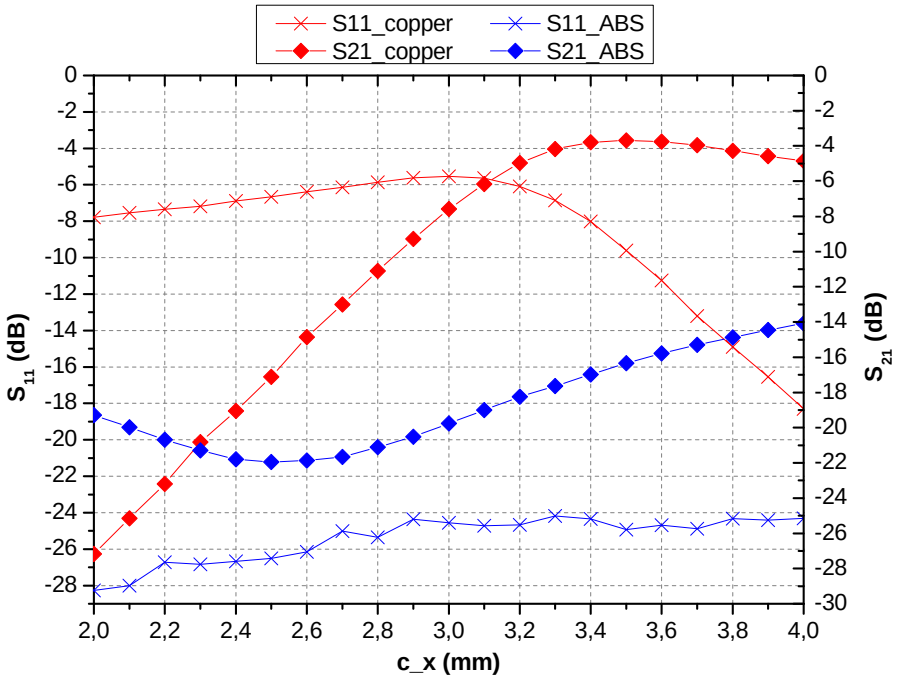


Figure 20: Simulated S-parameters for the back-to-back structure in function of the slot length c_x and the diaphragm materials.

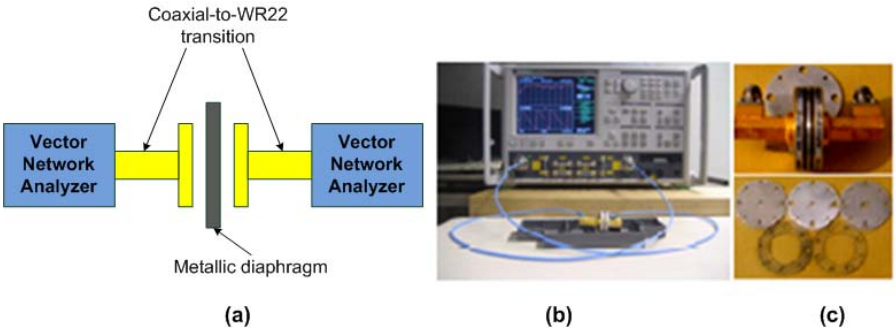


Figure 21: (a) Schematic of the experimental back-to-back structure. (b) Photo of the back-to-back structure connected to the VNA. (c) Set of metallic diaphragms and plastic pieces.

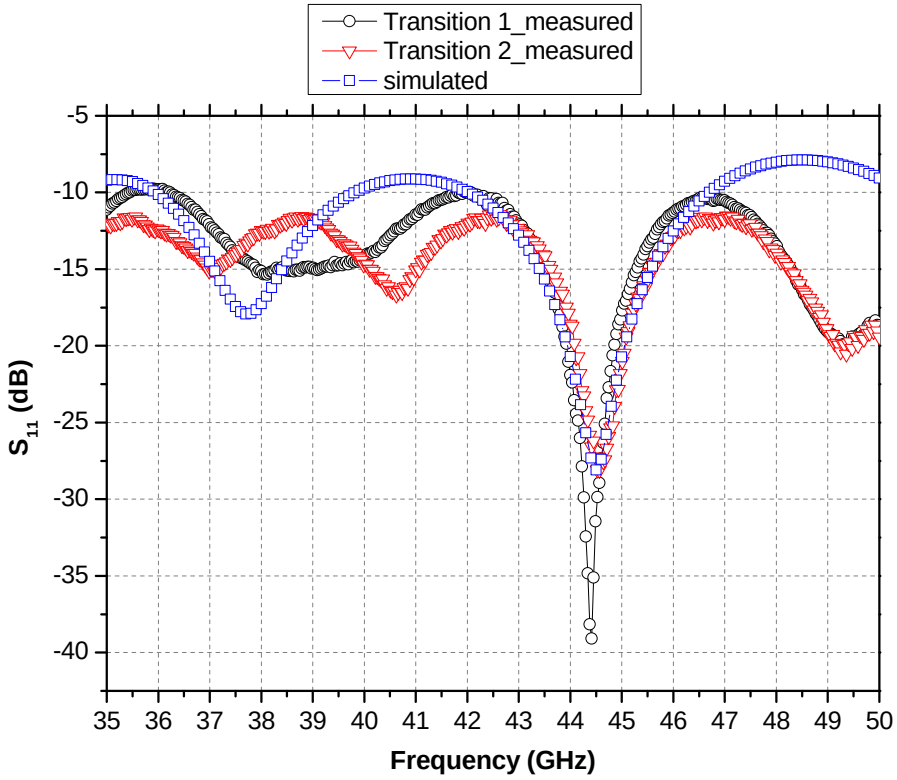


Figure 22: Measured and simulated reflection coefficient S11 of the two coaxial-to-WR22 transitions.

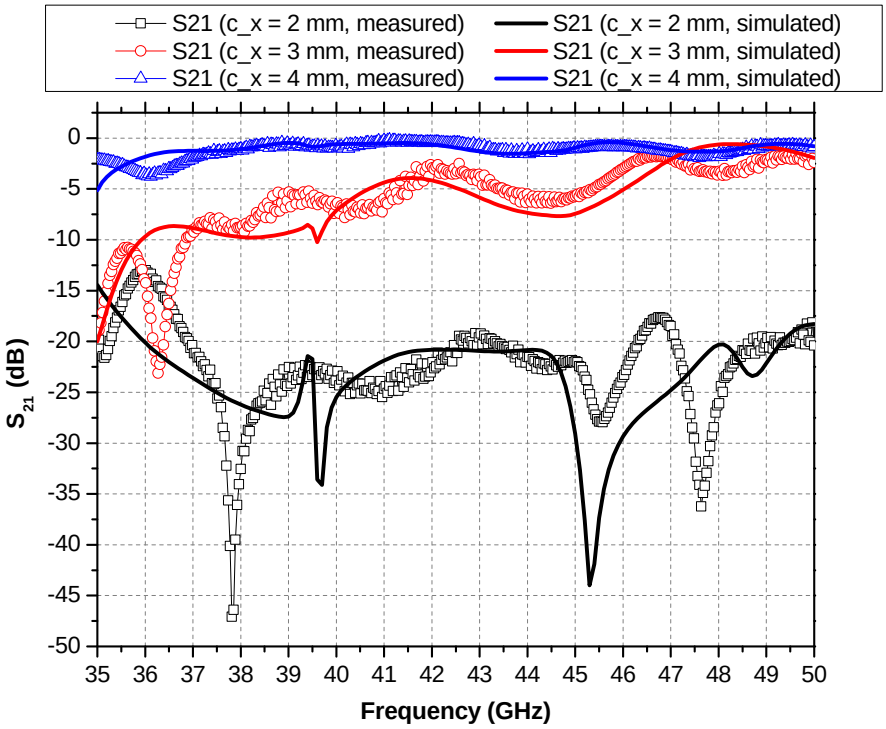


Figure 23: Measured and simulated transmission coefficient S21 of the coaxial-to-WR22 transitions, for slot length c_x = 2 mm, 3 mm and 4 mm.

2.7 DIFFERENT PROPOSED TECHNIQUES TO OPTIMIZE THE FRONT-END MODULE

After studying the microwave response of the front-end module, different microwave illumination techniques have been proposed to be used in radiating the Ratchet sample. A comparative analysis between these techniques has been performed to identify the most suitable techniques that could be used to optimize the experimental setup and hence improving the measured Ratchet photovoltage. This comparison (published in [28]) has been achieved by performing full wave electromagnetic simulations in order to compute the electromagnetic descriptors (discussed in section 2.4) for each technique and thus evaluating their electromagnetic behavior. For all the simulations models of the proposed techniques, the sample virtual position is represented by a set of five rectangles, linear spaced with a distance of 1 mm and positioned at 0.5 mm from the end of the investigated structures.

2.7.1 *Electromagnetic illumination using the WR22 aperture*

In this case, the rectangle R which represents the virtual position of the sample is illuminated using the WR22 section (typically the simulation model of Figure 15 has been used but the diaphragm, the sample and the package have been removed). The best performances have been obtained for a rectangle positioned at 4.5 mm from the end of the WR22 section.

2.7.2 *Electromagnetic illumination using the WR22 aperture and a Diaphragm*

This structure is quite similar with the previous but the diaphragm has been intercalated between the WR22 output aperture and the rectangles set (also the simulation model of Figure 15 has been used but the sample and the package have been removed). The associated material for this diaphragm has been chosen as metallic or absorber. The best performances have been obtained for a rectangle positioned at 4.5 mm from the absorber diaphragm and at a distance of 3 mm between the WR22 output aperture and the diaphragm. While for the copper diaphragm, the rectangle is at a distance of 2.5 mm from the diaphragm and the distance between the WR22 output aperture and the diaphragm is 1.5 mm.

2.7.3 *Electromagnetic illumination using the WR22 aperture and a Dielectric Lens*

The use of the dielectric lenses has been proposed to properly focus the microwave radiation on the small sample surface. In the millimeter wave band, these lenses have reduced weight ad size. As a result, they are used in the embedded systems for radars, satellites and wireless communication systems [29]. The principle of operation is based on the geometrical optics and Fermat's principle [29, 32], also, they could have spherical or hemispherical form. There are two types of dielectric lenses: (i) homogeneous [31] and inhomogeneous [29-31]. The homogeneous lenses are fabricated form one dielectric material, but the inhomogeneous lenses are fabricated from various dielectric materials with a refractive index that varies from the lens center till its surface. The Luneberg spherical lens [30, 31] and the Half Maxwell Fish-Eye (HMFE) hemispherical lens [29] are two examples of inhomogeneous lens antenna.
Inhomogeneous lens has a better performance for the electromagnetic waves focalization but they have a complex structure compared to the homogeneous one [31]. Since the

experimental setup used in obtaining the Ratchet photovoltage is complex too, the homogeneous lens illuminated by the WR22 section has been chosen to be studied and simulated. When simulating this type of lens, several parameters have to be taken into consideration: (i) the lens relative permittivity ε_r; (ii) the lens diameter D; (iii) the distance between the WR22 output aperture and the lens, as well as the distance between the lens and the sample. A single medium lens of $\varepsilon_r = 3$ and $\tan\delta_e = 0.0018$ has been chosen for simulation.
Concerning the distance between the WR22 output aperture and the lens, decreasing this distance makes the lens gain increases and the focus character of the lens becomes much better, according to [31]. It has been noticed that good results can be obtained for a lens positioned directly to the end of the WR22 section.
Preliminary parametric analysis based on full wave simulations has been performed for spherical and hemispherical dielectric lens. The aim of this analysis is to study the influence of the lens diameter D variation on the power flow and the uniformity of the electric field polarization on the sample surface. Figure 24 shows the simulation models of the spherical and the hemispherical lenses.

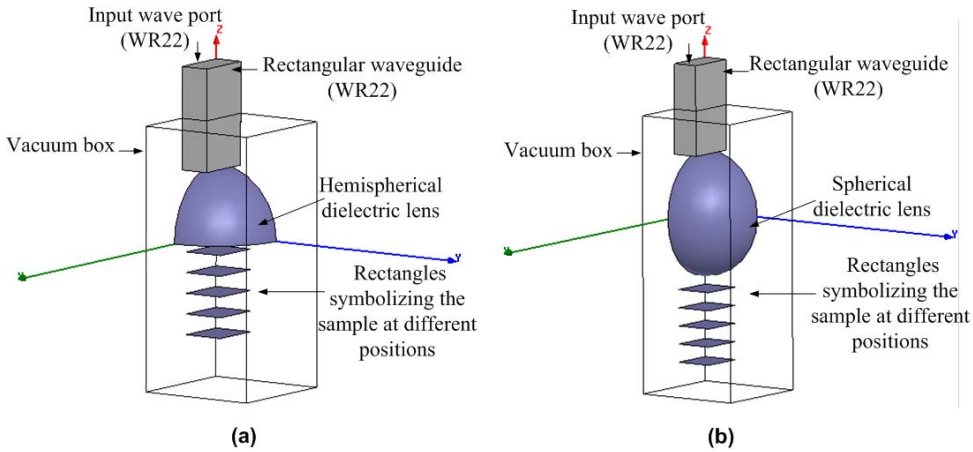


Figure 24: HFSS model of the dielectric homogeneous lens representing the two shapes: (a) hemispherical and (b) spherical.

2.7.4 *Electromagnetic illumination using the WR22 and a Dielectric Multi-slab structure*

This structure consists of two identical cylindrical dielectric layers (separated by air) illuminated by a WR22 section with a flange (type FUPG400) as shown in Figure 25. This structure is similar with the multi-slab dielectric structures based on Cantor superlattice used for patch antenna directivity enhancement [33]. A first design has been made using homemade software based on analytical expressions [33]. This design supposes that the dielectric layers and the flange dimensions are infinite in horizontal plane. The diameter of the flange (and the diameter of the dielectric cylinders) is 28.6 mm. A parameteric analysis based on electromagnetic simulations has been performed. Good performances have been obtained for the following structures: for the first structure S1, the distance between the flange and the first dielectric layer: a0 = 3.5 mm, the distance between the dielectric layers: a1 = 1 mm, the thickness of the dielectric layers: h = 1.6 mm, the relative permittivity $\varepsilon_r = 6$ and $\tan\delta_e = 0.0018$. For the second structure S2, a0 = 3.5 mm, a1 = 1 mm, h = 3.2 mm, $\varepsilon_r = 3$ and $\tan\delta_e = 0.0018$.

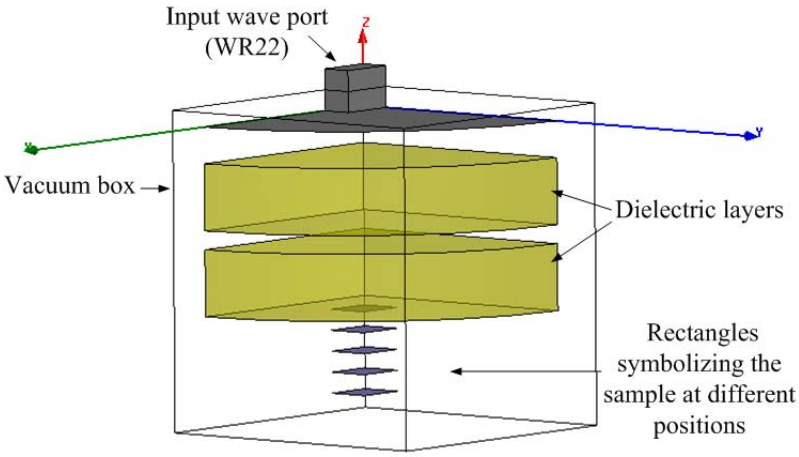


Figure 25: HFSS model of two-dielectric slabs structure.

2.7.5 *Electromagnetic illumination using the WR22 and a Horn Antenna*

Figure 26 shows the simulation model of a horn antenna [34] designed for a theoretical maximum gain of 20 dBi gain. This antenna has been designed using Antenna Magus [35] for an optimum gain horn of 20 dBi (maximum gain for the shortest possible flare length). The length of the horn antenna output aperture is 31.36 mm and its width is 24.45 mm.The best results have been obtained for a rectangle positioned at 0.5 mm from the end of the antenna.

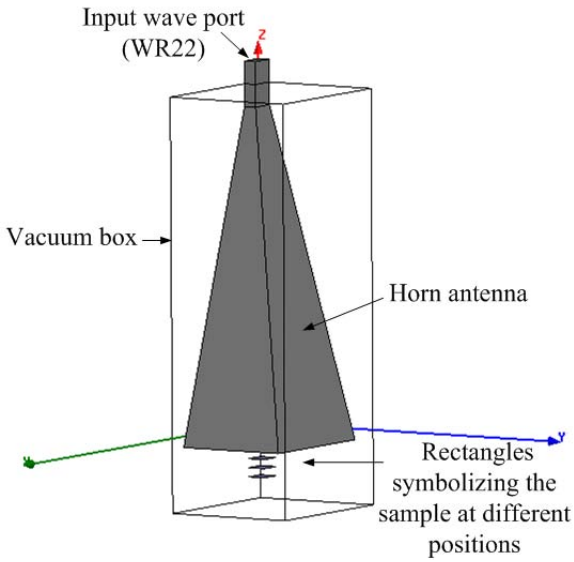


Figure 26: HFSS model of the horn antenna designed.

2.8 PERFORMANCE COMPARISON BETWEEN THE DIFFERENT PROPOSED TECHNIQUES

After studying and simulating each technique, a comparison has been performed between them from the electromagnetic point of view. This comparison is based on calculating the electromagnetic descriptors of the incident power as well as the uniformity of the electric polarization and the power density on the sample surface. Moreover, the size of the investigated structures has been compared. It has been evaluated by the mean of the following parameters: (i) normalized (to wavelength) axial size Ls that represents the distance between the end of the WR22 section and the end of the antenna, (ii) distance dz between the sample position (rectangle R) and the end of the antenna. The results are summarized in Table 1.

Proposed Techniques		K_E (%)	K_P (%)	P_n (%)	Ls	dz
WR22		88.4	36.6	23.3	-	4.5
WR22 + Metallic Diaphragm		80	25	3	0.3	2.5
WR22 + Absorber Diaphragm		98.3	75.4	1.8	0.5	4.5
WR22 + Spherical Lens	D = 7 mm	98.5	47.6	14.2	1	4.5
	D = 14 mm	98.3	38.4	3.8	2	4.5
WR22 + Hemispherical Lens	D = 7mm	99	73.9	8.7	0.5	4.5
	D = 14 mm	92.4	65.1	12.2	1	1.5
	D = 21 mm	96.1	52.4	6.4	1.5	1.5
	D = 28 mm	93.2	62.6	3.8	2	0.5
WR22 + Dielectric Multi-slab	S1	97.8	87.6	6.7	1.1	3.5
	S2	89	88.3	6.7	1.6	4.5
WR22 + Horn Antenna		98	90	6	4.5	0.5

Table 1: Summary of electromagnetic simulation results.

As shown in Table I, the optimization criteria (maximizing the parameters K_E, K_P and P_n while minimizing the axial size: Ls) are more or less contradictory. The horn antenna has good performance over the first two criteria (maximizing K_E and K_P) but it is very bulky. In addition to its important axial size, a large aperture size has been obtained (see subsection 2.7.5). Using only a WR22 gives an important ratio of power P_n but a poor uniformity of the incident electric field linear polarization K_E and of the incident power density K_P on the sample surface. Adding an absorber diaphragm improves the polarization uniformity with a small axial size, but with a very low amount of incident power. The dielectric lens allows obtaining a good uniformity of the electric field polarization. Using the WR22 section and the dielectric multi-slabs seems to offer also a good trade-off between the descriptors K_E, K_P and P_n with an acceptable axial size (approximately one wavelength for S1).
As a conclusion, this work allows us to identify possible solutions and their intrinsic performances in order to illuminate the Ratchet sample with microwave radiation in a free-space measurement setup.

2.9 CONCLUSION

This chapter presented the electromagnetic investigation of the front-end module which represents the radiation part of the whole complex system used in the experimental study of Ratchet Effect. Some other radiation techniques have been studied and simulated that could replace the current front-end module. As explained in the previous sections, several factors affect the electromagentic behavior of the setup:

- The distance between the sample and the source of radiation.
- The materials from which the different parts of the setup are made.
- The illumination technique used in radiating the studied sample.

All these factors have to be taken into consideration before judging on the sample response.
However, the presence of the cryogenic system which is the main reason of the actual experimental setup complexity, limits the choice between the different radiation techniques proposed in section 2.7. For example, the horn antenna can not be used in performing measurements at low temperature due to its large dimensions compared to the diameter of the cryogenic cavity used.
Therefore, in the next chapter, an electromagnetic analysis of the cryogenic metallic cavity will be introduced to show how it could disturb the experimental measurements and could negatively affect the reproducibility of the observed phenomenon.

3

INFLUENCE OF THE CRYOGENIC METALLIC CAVITY SYSTEM ON THE ELECTROMAGNETIC BEHAVIOR OF THE SETUP USED AT LOW TEMPERATURE

3.1 INTRODUCTION

In the previous chapter, a detailed description of the experimental setup and its microwave front-end module was presented. Actually, a cryogenic system is used to keep the sample at low temperature and to perform to the magnetotransport measurements which require a large temperature range (1.4 to 77 K) and magnetic fields up to 15 T. Therefore, the front-end module is not totally exposed to free space, as simulated before, but it is surrounded by a metallic closed cavity. Inside this closed metallic cavity, there are complex metallic parts of various shapes to support the sample, to rotate it in different angles and to connect it to the other instruments needed in measurements. The presence of the cryogenic metallic cavity leads to the generation of standing waves. Moreover, the other metallic parts inside of it disturb the electric field distribution. This makes the position of the sample inside the cryogenic system very critical. Therefore, to be closer to the actual case, the setup has to be simulated with the presence of this closed metallic cavity and all the metallic parts inside of it. The electromagnetic study of the cryogenic metallic cavity has been published in [36]. This chapter indicates that the methodology steps have been also applied on the study of the front-end module used at low temperature.

3.2 DESCRIPTION OF THE FRONT-END MODULE USED AT LOW TEMPERATURE

Figure 27 shows the closed metallic cavity of the cryogenic system and the complex metallic parts inside of it. At the center of the metallic cavity, there is a metallic tube that holds the sample and the packages. Under this central metallic tube, a rotating metallic cylinder permits to rotate the sample 360 degrees and hence changing the direction of the sample with respect to the polarization of the microwave field. Another four metallic cylindrical tubes are placed near the boundary of the metallic cavity. The sample is radiated by the circular-to-rectangular transition which penetrates the metallic cavity of the cryogenic system.

3.3 ELECTROMAGNETIC SIMULATION MODELS OF THE FRONT-END MODULE USED AT LOW TEMPERATURE

Many simulation models, sketched in Figure 28, have been designed using the full-wave simulator Ansoft HFSS. First, Model 0 has been created which represents the simplest case as it considers the cryogenic cavity as an empty hollow metallic closed cylinder, without the metallic parts inside of it. The radius of the cavity is 14.205 mm, so by using a Matlab code (given in appendix A), the number of modes [37] inside the cavity is found to be 58 at the operating frequency of 50 GHz. This frequency has been used in the recent experimental measurements presented in [9] on Si/SiGe samples. Afterwards, a series of models have been simulated; Model 1, Model 2, Model 3 and Model 4; in each one, a metallic part has been added to be as close as possible from the actual setup. The

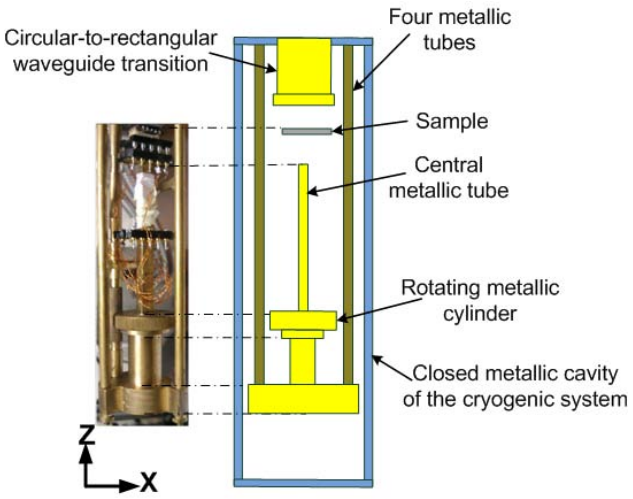


Figure 27: Photo and schematic of the complex metallic parts inside the metallic cavity of the cryogenic system.

height of the cavity is taken to be 179.62 mm which corresponds in the actual setup to the distance from the output aperture of the circular-to-rectangular waveguide transition till the bottom of the metallic cavity. Except for Model 3 and Model 4, where a distance of 20 mm has been added to the height of the cavity. This additional distance represents the penetration height of the waveguide into the cavity. A wave port has been used to represent the source of the microwave energy with the same dimensions of the WR22. To symbolize the sample, many rectangles with a surface of 4 mm × 2 mm, have been placed at different positions inside the cavity. They have been put in the common area between all the models, near the output aperture of the waveguide. These simulation models have been split using one symmetry plane: perfect magnetic boundary conditions (y-z plane), to reduce the calculation simulation time. HFSS software has been used to simulate these models, as it includes the fields calculator which is essential to calculate the analytical equations that quantify the Ratchet Effect. But according to the setup dimensions, there is a challenge in simulating these very big structures using the finite element method of HFSS which requires a huge computation time and large memory (about 32GB RAM).

3.4 STUDY OF THE ELECTROMAGNETIC RESPONSE OF THE SIMULATION MODELS

As explained in the previous chapter, the electromagnetic simulations have been performed without taking into account the presence of the closed cryogenic metallic cavity. Analytical equations based on the electromagnetic power calculation on the sample surface have been used to evaluate the setup response. However, the two descriptors P_n and K_P, that compute the incident power and the power density on the sample surface, could not be used to study the actual setup with the metallic cavity as it produces standing waves. Consequently, similar analytical equations have been computed based on the electromagnetic field distribution inside the cavity and on the amount of the incident field on the sample surface. The study of the electromagnetic response of each simulation model has been performed as follows:

i. Studying the distribution of the y-component of the electric field E_y inside the metallic cavity. Standing waves could be observed in the closed metallic cavity. As a result,

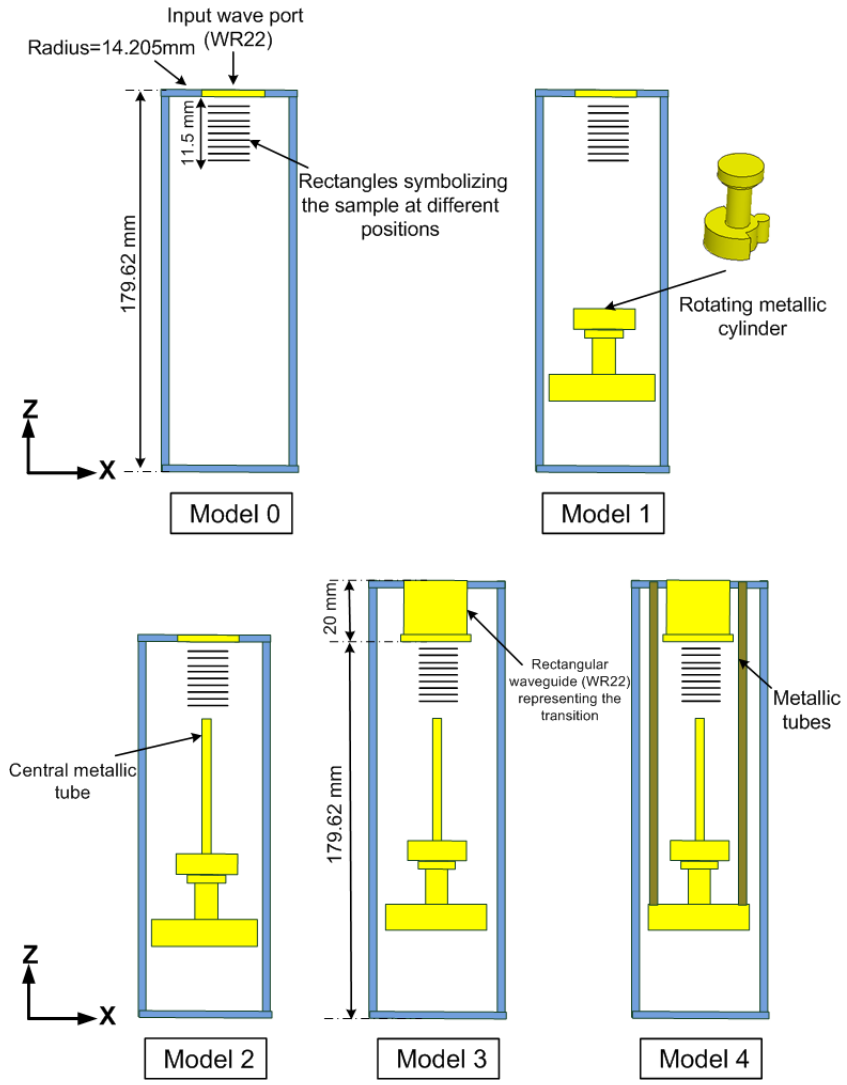


Figure 28: Schematics of the simulation models representing the front-end module used at low temperature.

some regions with maximum values of the electric field and others with zero fields are found inside the cavity. Thus, the distribution of the electric field has to be studied to make sure that the sample is in a position where there are high values of the electric field y-component to produce the Ratchet photovoltage. This distribution changes each time a metallic part is added to the simulation model.

ii. Calculating the uniformity of the electric field linear polarization K_E on the sample surface using equation 2.2

iii. Calculating the uniformity of the y-component of the electric field density K_D on the sample surface using equation 27.

$$K_D = \frac{min^R \left|\overrightarrow{E_y}\right|}{max^R \left|\overrightarrow{E_y}\right|} \times 100\,[\%] \tag{3.1}$$

The size of the studied region (antidots lattice on the sample) is: length = 250 µm and the width = 50 µm. But the overall maximum size of the sample (including the regions without antidots and the sample contacts) is: length = 4 mm and the width = 2 mm. These equations have been computed using the fields calculator of HFSS, on rectangles R which have the maximum size of the real sample (4 mm × 2 mm, the worst case). These rectangles are at a distance of 0.5 mm to 11.5 mm from the wave port for Model 0, Model 1 and Model 2. But for Model 3 and Model 4, this distance is measured from the waveguide output aperture. In each simulation model, we do not search for the maximum values of each descriptor separately; but we try to determine a region where there are high values of the three descriptors; E_y, K_E and K_D . Thus, the sample can be put in the chosen region which guarantees generating high Ratchet photovoltage and uniformly distributed electric field on the sample surface. If many appropriate regions are found in one model, the best position is determined with respect to the complexity of the actual setup where there is a certain tolerance in moving the sample without losing the Ratchet voltage.
The simulation results of Model 0 in Figure 29 show that the best region where to put the sample is between 6.5 mm and 8.5 mm away from the wave port. When adding the rotating metallic cylinder, Model 1, the value of the electric field is affected. It is clear from Figure 30 that this value is decreased by 87 % compared to Model 0. Also, the best region in this model is shifted between 3 mm and 5 mm. For Model 2, 50 % of the electric field is lost compared to Model 1. In this model, the sample can be placed between 4.5 mm and 6 mm, as it is shown in Figure 31.

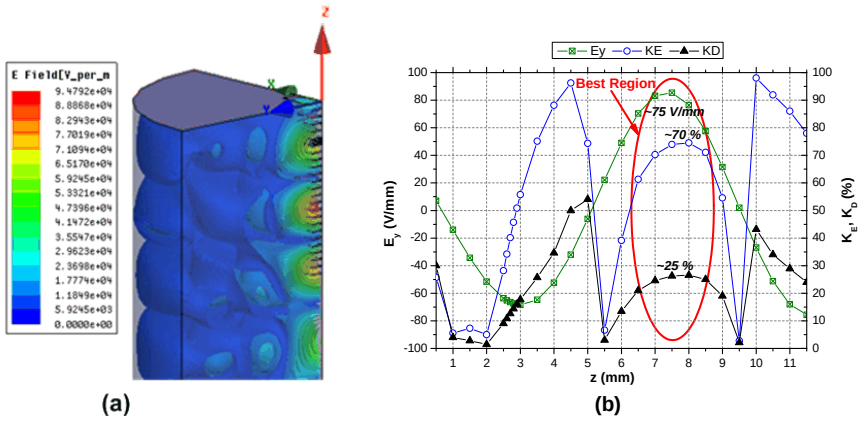


Figure 29: (a) 3D plot of the magnitude of the total electric field in V/m inside the closed metallic cavity. (b)E_y, K_E and K_D calculated on the rectangles representing the sample at different positions (Model 0).

When the waveguide transition penetrates the metallic cavity of the setup with a height of 20 mm, Model 3, the best region becomes too narrow compared to the previous models. From Figure 32, the sample can only be placed between 3.5 mm and 4 mm which means that there is a tight tolerance of 0.5 mm. Therefore, a parametric study of the transition height inside the cavity is performed. The rectangles representing the sample remain at fixed position while decreasing the transition height by 1 mm. The results presented in Figure 33 demonstrate that the three descriptors are improved if the transition height is 19 mm instead of 20 mm used in the actual setup. The best region is between 6.5 mm and 8 mm. These last results show how a little change in the transition height can totally change the electromagnetic behavior of the setup.

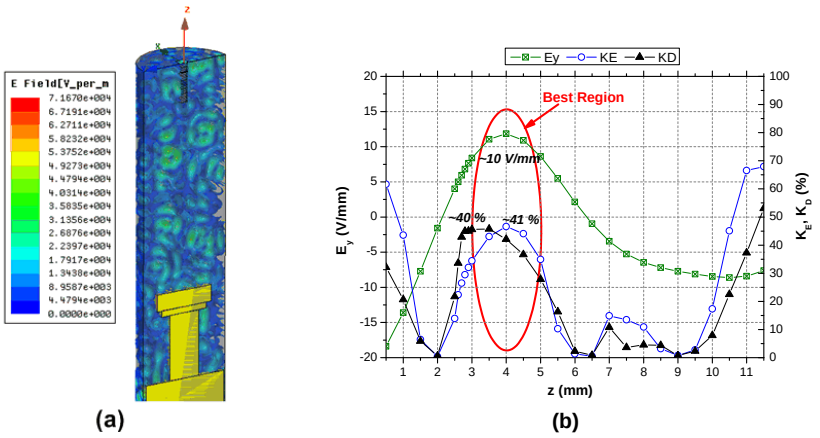


Figure 30: (a) 3D plot of the magnitude of the total electric field in V/m inside the closed metallic cavity. (b)E_y, K_E and K_D calculated on the rectangles representing the sample at different positions (Model 1).

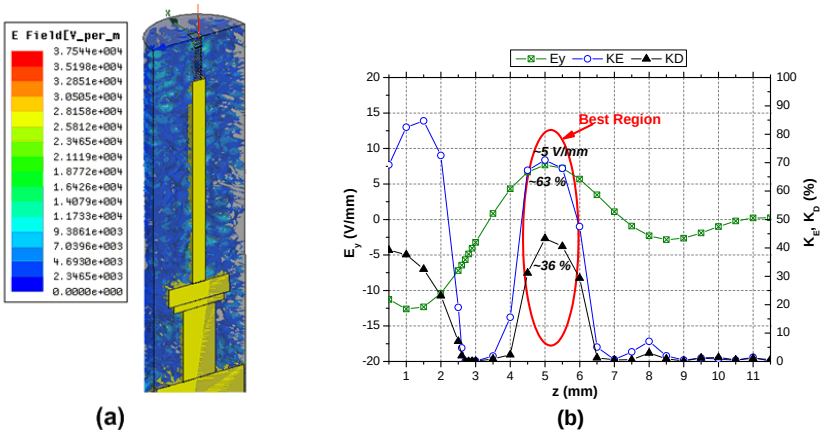


Figure 31: (a) 3D plot of the magnitude of the total electric field in V/m inside the closed metallic cavity. (b)E_y, K_E and K_D calculated on the rectangles representing the sample at different positions (Model 2).

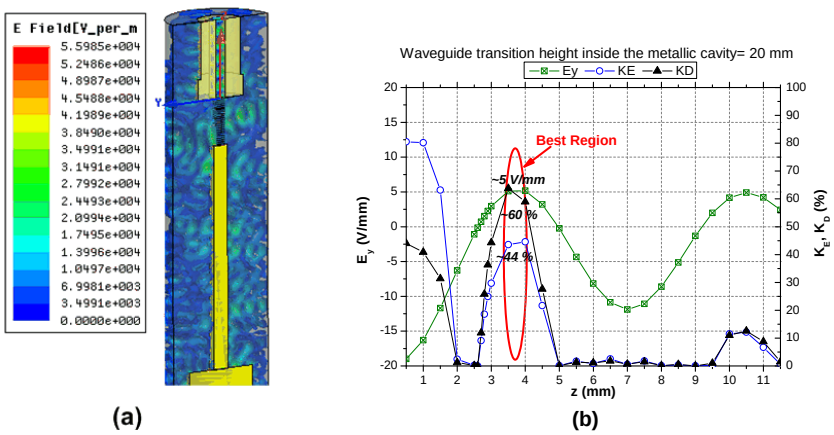


Figure 32: (a) 3D plot of the magnitude of the total electric field in V/m inside the closed metallic cavity. (b)E_y, K_E and K_D calculated on the rectangles representing the sample at different positions (Model 3).

Finally, Figure 34 presents the simulation results of Model 4 which is the most complex model. As described in section 3.2, there are four cylindrical metallic tubes in the actual experimental setup. Due to the memory limitation, only two cubical metallic tubes are simulated to estimate the setup response when adding metallic parts near the cavity boundary. The results are enhanced compared to Model 3 and the best region is located between 4 mm and 5.5 mm.
The convergence criteria used in simulating these models are: maximum delta S is 0.01 and the minimum number of converged passes is 3. However due to the complexity of Model 4, the criteria used are 0.05 and 2 respectively. The maximum delta S is defined as the maximum change in the magnitude of the S-parameters between two consecutive passes. Figure 35 and Figure 36 show the convergence curves obtained when simulating Model 3 and Model 4.
These simulation results representing the setup with its exact dimensions have been published in [36]. A Comparison of these results with the ones published in [38] which represent the setup with approximate dimensions, shows that the electromagentic response is different between the two cases. However, it has to be mentionned that the determination of these exact dimensions is not an easy task due to the complexity of the used setup.

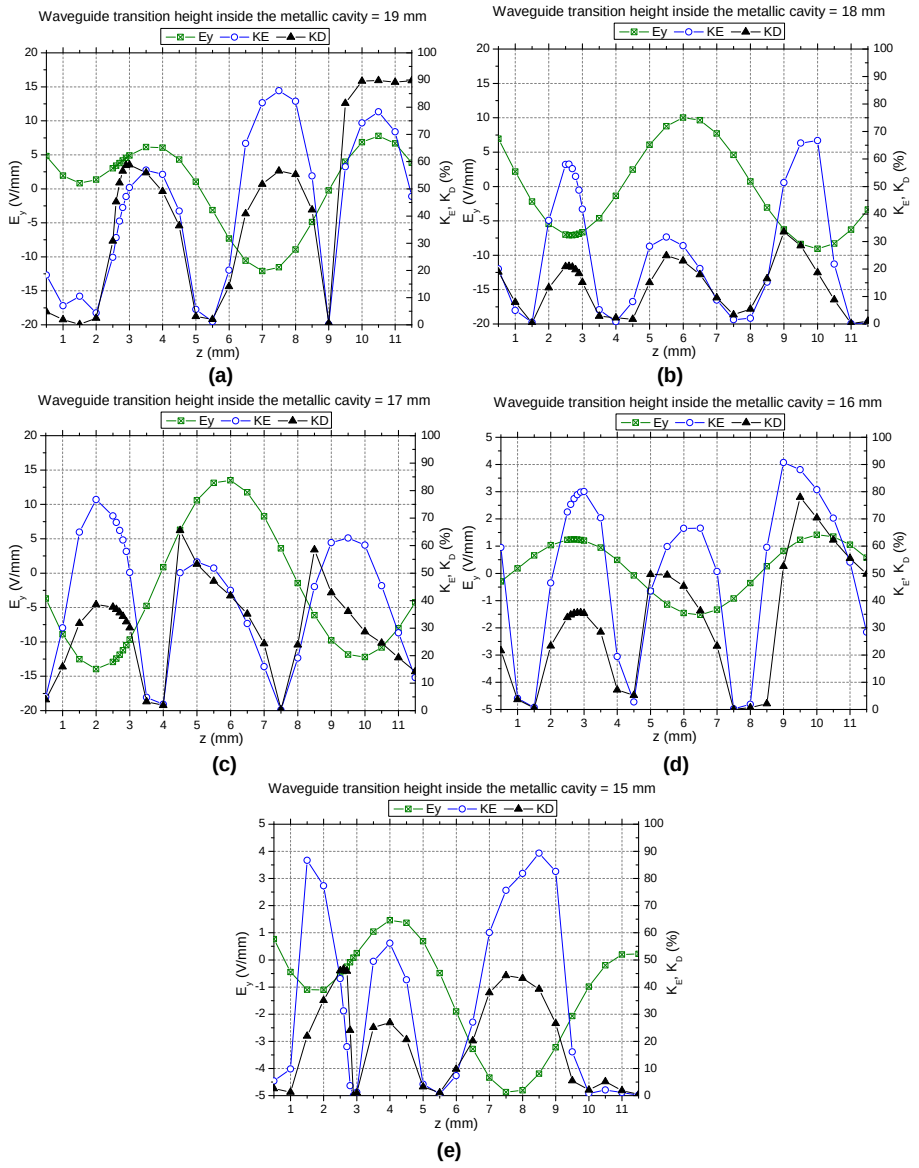


Figure 33: E_y, K_E and K_D calculated on the rectangles representing the sample at different positions when varying the waveguide transition height between 15 mm and 19 mm.

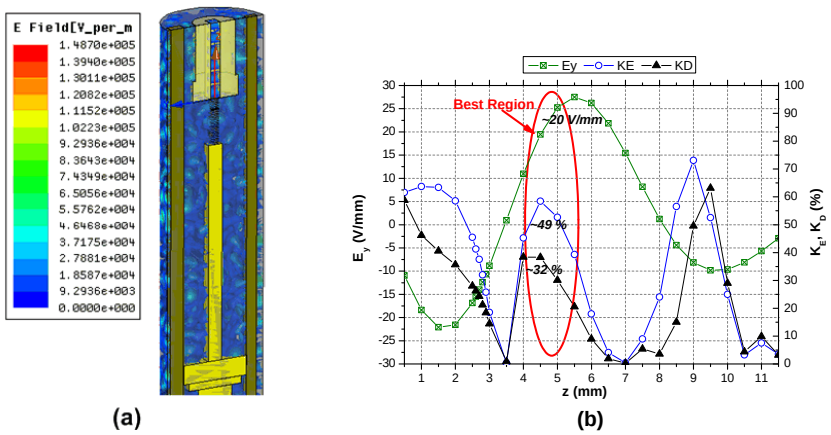


Figure 34: (a) 3D plot of the magnitude of the total electric field in V/m inside the closed metallic cavity. (b)E_y, K_E and K_D calculated on the rectangles representing the sample at different positions (Model 4).

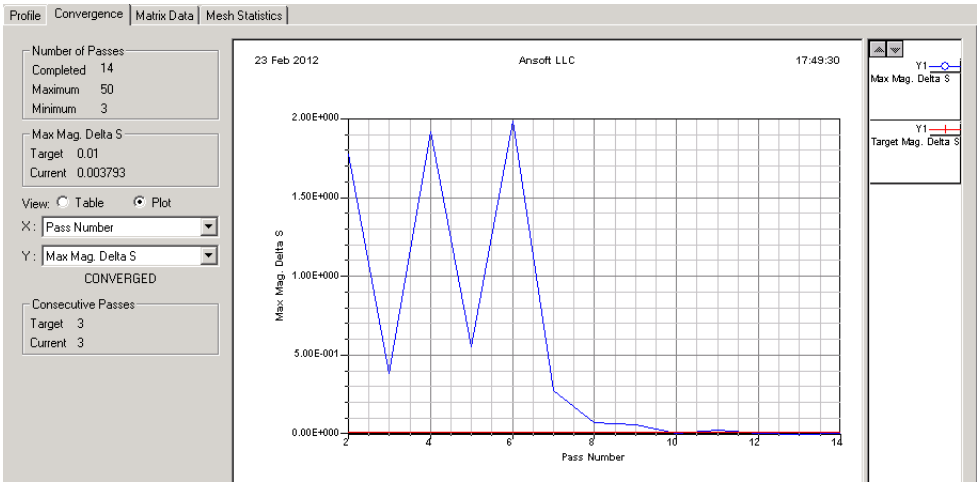


Figure 35: Convergence curve of Model 3 with maximum delta S = 0.01 and the minimum number of converged passes is 3.

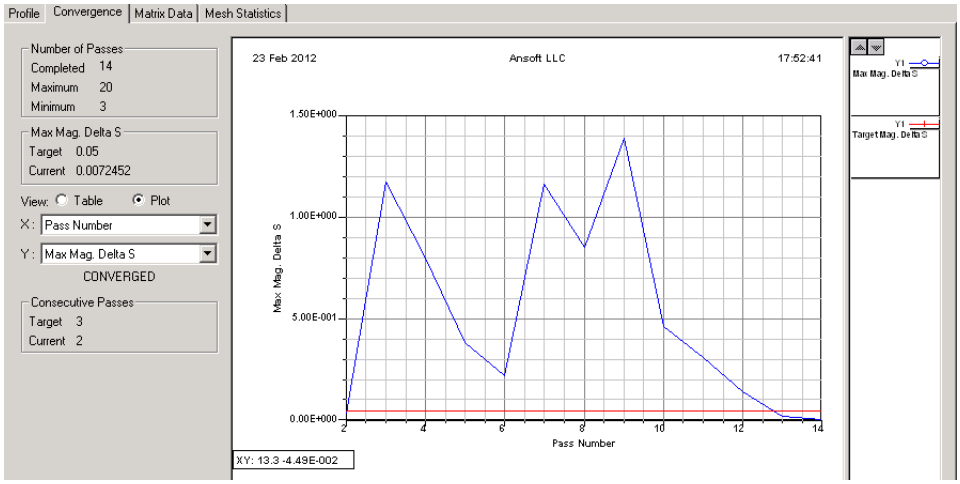


Figure 36: Convergence curve of Model 4 with maximum delta S = 0.05 and the minimum number of converged passes is 2.

3.5 DEPENDENCE OF THE SETUP ELECTROMAGNETIC RESPONSE ON THE OPERATING FREQUENCY

According to the experimental results obtained, the Ratchet photovoltage changes with respect to the microwave frequency (see Figure 12). Nevertheless, the reason of this change could be due to the reflection of the electric field with the various metallic parts of the experimental setup and hence the distribution of the electric field will change inside the closed metallic cavity of the cryogenic system. Thus, this could affect the Ratchet sample response. As a result, an electromagnetic simulation study of the operating frequency influence on the electromagnetic behavior of the setup has been performed. This study could give an approximate approach of the complex experimental setup response. This has been achieved by using Model 4 which is the closest model to the actual setup and a range of frequency from 30 to 35 GHz. The variation of E_y, K_E and K_D for each frequency is presented in Figures 37, 38(a) and (b) respectively. It is clear from these simulation results that for each frequency, the setup response completely changes. For example, if the sample is at 2 mm from the waveguide output aperture and a frequency of 35 GHz is used, it could be noticed that the values of E_y, K_E and K_D are too small. Consequently, this could reduce the measured Ratchet photovoltage at 35 GHz.

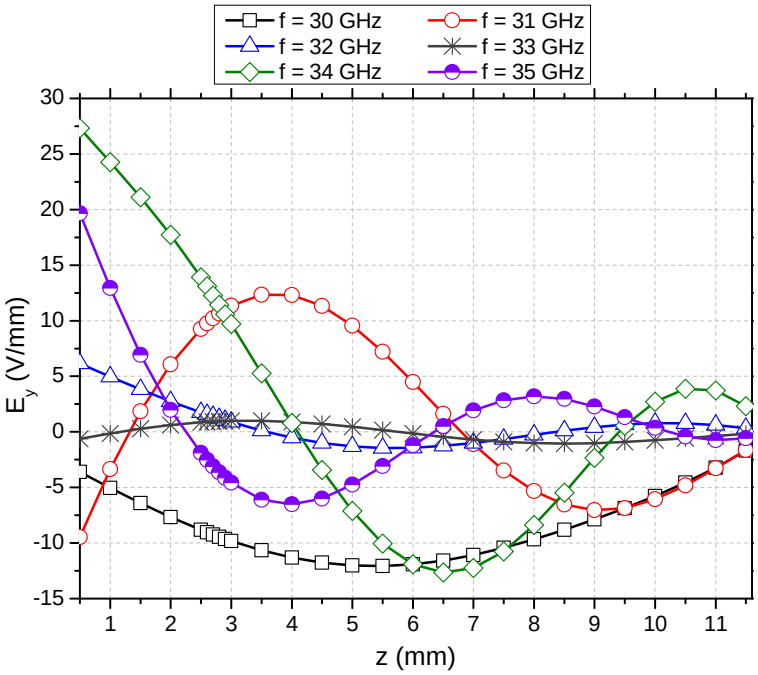


Figure 37: Variation of E_y for various operating frequencies at different positions of the sample (Model 4).

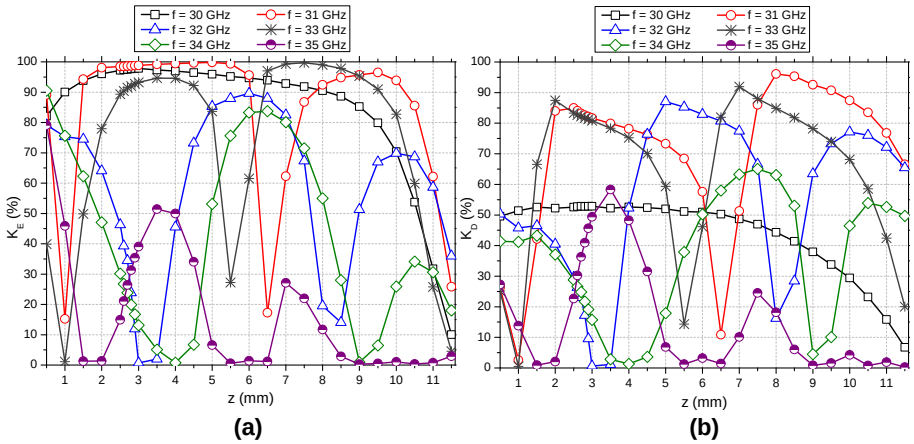


Figure 38: Variation of (a) K_E and (b) K_D for various operating frequencies at different positions of the sample (Model 4).

3.6 CONCLUSION

This chapter discussed the electromagnetic behavior of the metallic cryogenic cavity of the setup used in performing the Ratchet experiments and its impact on the produced photovoltage. Many electromagnetic simulation models have been created to demonstrate that each metallic part added to the setup has a great influence on the electromagnetic behavior of the whole system, as it causes a change in the electric field distribution inside the cavity. It has been noticed that in every model there is an optimal region where there are good values of the three descriptors: E_y, K_E and K_D that ensure best conditions for the generation of high Ratchet photovoltage and thus it is preferable to place the sample in this optimal region. This region changes its position according to the metallic parts added to the system. Its range is about 1.5 mm which means that a little change in the sample position could change the experimental results obtained. From the simulation results of Model 4, which is the closest model to the actual setup, it seems better to put the sample between 4 mm and 5.5 mm if a 20 mm transition height is used.
As a result, this electromagnetic investigation had highlighted another drawback of the experimental setup, besides its huge size, which is its electromagnetic sensitivity to any little modification that is sometimes difficult to control while doing the experimental measurements.

4

FEASIBILITY STUDY OF AMPLITUDE DEMODULATORS BASED ON RATCHET EFFECT

4.1 INTRODUCTION

Amplitude modulation (AM) is one of the earliest radio modulation techniques [39, 40]. The process of extracting the information signal from the modulated signal is called demodulation [39, 40]. In communication systems, many demodulation techniques could be used in manufacturing radio receivers. The simplest one consists of using a diode detector [39, 40], but it is not an efficient method to demodulate the received signal, as it can introduce significant levels of harmonic distortion [40] and hence it is not suitable for high quality applications. Signal detection can also be achieved using more effective and higher level of performance detection systems based on complex electronic circuits, which require a lot of electrical parts making the system bulky and expensive.
The linear dependence of the Ratchet photovoltage on the microwave power applied (see Figure 8 and Figure 10(e)) gives the possibility of using the Ratchet Device as an amplitude demodulator. This can be interpreted as follows:
The general concept of amplitude modulation consists of varying the amplitude of the carrier signal according to the amplitude of the information signal, which means that the power of the transmitted signal varies. Afterwards, the demodulation process is performed by detecting the enveloppe of the incoming signal (in case of using a diode detector). For the Ratchet Device case, if the signal receieved by the Ratchet sample is modulated, the sample detects a change in the amount of power received and consequently the Ratchet produced photovoltage changes giving the shape of the information signal sent.
This chapter presents some preliminary trials of amplitude demodulation that have been tested by CNRS-LNCMI and CNRS-LAAS teams using Si/SiGe Ratchet samples. These measurements have been performed in CNRS-LNCMI, Grenoble where the Ratchet samples and the cryogenic experimental setup are available, while the modulation proposed techniques and the instruments used have been provided by CNRS-LAAS, Toulouse.

4.2 EXPERIMENTAL SETUP USED IN THE ANALOG AMPLITUDE DEMODULATION TESTS

As described in section 2.2 and illustrated in Figure 14, a carcinotron is used to generate the microwave signal which represents the carrier signal. In order to determine the Ratchet sample response to the modulation technique, a prelimiary test has been done in CNRS-LAAS using the set presented in Figure 39. It consists of a function generator that produces the pulse signal which represents the message signal and it is used to modulate the carrier signal generated by a carcinotron that operates in the 110–170 GHz. The power of the modulated signal is measured using a calorimeter.
The duty cycle[1] of the modulating signal has been varied from 42 % to 62 %. Figure 40(a) shows that the power of the modulated signal is quasi-linear with respect to the duty cycle of the message signal at different frequencies of the message signal (f = 1, 10 and

1 The duty cycle is defined as the ratio of the "ON time" to the "TOTAL time" (ON time + OFF time) of operation [41].

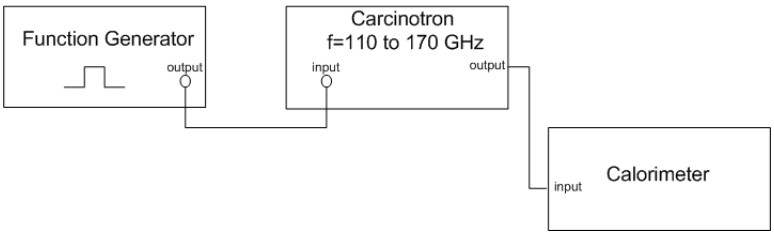


Figure 39: Schematic of the set used to test the modulation technique.

100 KHz). Consequently, it has been noticed that the Ratchet photovoltage generated by the studied sample is also quasi-linear with respect to the duty cycle, as shown in Figure 40(b). The sample response has been observed by LNCMI team using a carcinotron in the 33–50 GHz frequency range. For the two measurements, the level of attenuation is 0 dB, this level could be adjusted using an attenuator connected to the carcinotron output.

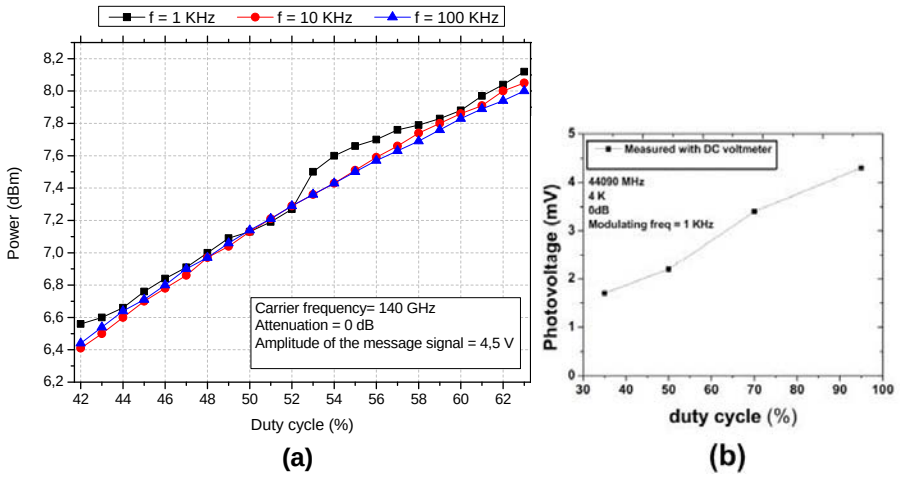


Figure 40: (a) Variation of the output power with respect to the duty cycle of the message signal at different frequencies using a carrier signal of 140 GHz. (b) Variation of the Ratchet photovoltage with respect to the duty cycle of the message signal, for a carrier signal of 44.09 GHz and a modulating signal of 1 KHz.

However, the carcinotron can only read a pulse signal for the external modulation with amplitude from 4 to 5 V. It works as a switch, ON when the amplitude is in the accepted range (4–5 V) and OFF when it is below this range. As a result, it can not detect the difference in amplitude, for example between 4.5 V and 5 V, and it gives the same value of power for the two ON states. Therefore, it can not generate directly an analog amplitude modulated signal but it could be used in performing digital and pulse modulation tests. In order to perform the analog amplitude modulation, the carcinotron has been replaced by a synthesized signal generator (Anritsu MG3694B), with an option of high output power, that operates from 10 MHz to 40 GHz frequency range, with a maximum output power of 30 dBm for low frequencies, but around 20 dBm of maximum power for high frequencies. This power value is comparable with the output power of the carcinotron in the 33–50 GHz frequency range. This signal generator can produce amplitude modulated signal directly, where the frequency and the type of the message signal, the output power level and the modulation depth can be adjusted.

Figure 41 represents the experimental setup and the instruments used in performimg the amplitude demodulation tests. The sample contacts are connected to a digital multimeter to measure the photovoltage. The sample response to the modulated microwave signal is captured by a digital oscilloscope after amplification by a pre-amplifier with band pass filters. A NI LabVIEW program [42] has been developed to control the instruments which are connected together via GPIB cables and they are connected to the computer via GPIB-USB card.

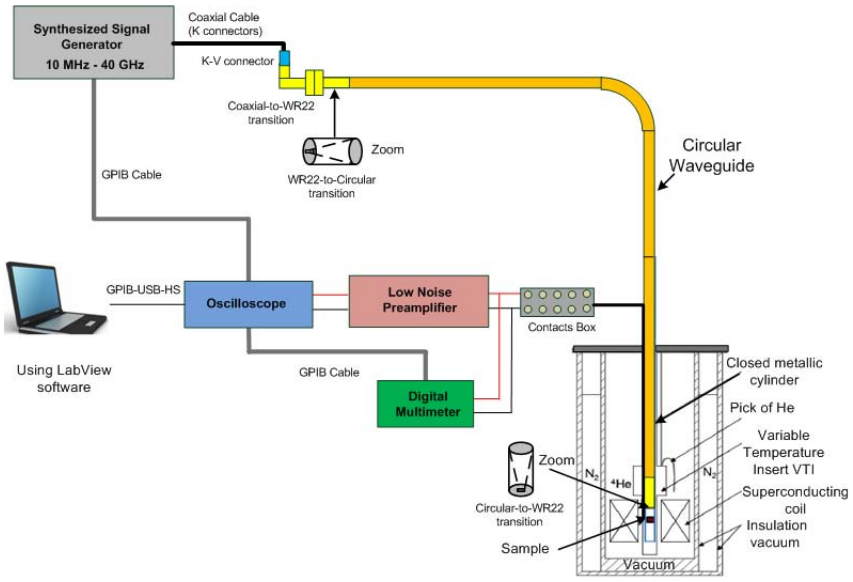


Figure 41: Schematic of the experimental setup and the instruments used in the amplitude demodulation tests.

4.3 DESCRIPTION OF THE STUDIED SAMPLES

Figure 42 illustrates simplified schematics of the two samples that have been used in the amplitude demodulation tests. The first sample is a Si/SiGe sample divided into three regions: the first region where the semicircular antidots are patterned, a second region for the circular antidots and a third region which is left unpatterned. The radius and the period of antidots are 200 nm and 600 nm respectively with a non-hexagonal lattice.
The second studied sample is a virgin sample (without antidots) and it is also based on Si/SiGe with the same size (length and width) of the first studied sample.

4.4 EXPERIMENTAL RESULTS

Before applying the amplitude demodulation, a set of characterization measurements have to be performed to check the sample response with respect to the magnetic field, the temperature and the microwave power (as discussed in chapter 1). First, the experimental results of the first studied sample with the three regions: semicircular, 2DEG and circular antiots will be presented.
Using a LabVIEW program, the microwave frequency generated by the synthesized signal generator has been varied and the photovoltage generated by the semicircular antidots region has been measured between contacts 2 and 3 (see Figure 42(a)) using the digital

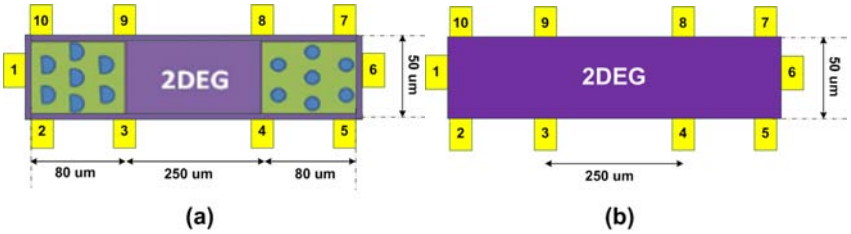


Figure 42: Schematics of the two studied heterostructures samples based on Si/SiGe. (a) Sample with semicircular antidots, unpatterned 2DEG region and circular antidots. (b) Virgin sample without antidots.

multimeter. The aim of this measurement step is to try to choose the microwave frequency of the carrier signal at which a high value of phovoltage can be obtained and hence using this frequency when applying the amplitude demodulation test.
Figure 43 shows the variation of the photovoltage with respect to the microwave frequency, when the sample is at a temperature of 4 K and zero magnetic field. Some peak photovoltages are obtained at f = 29.23, 29.51, 32.065 and 36.71 GHz. The cut-off frequency of the circular-to-rectangular waveguide transition that radiates the sample (see section 2.2 of chapter 2) is about 26.5 GHz. This explains the reason for obtaining a zero photovoltage for the band between 27 GHz and 28 GHz, which is close to the cut-off frequency.

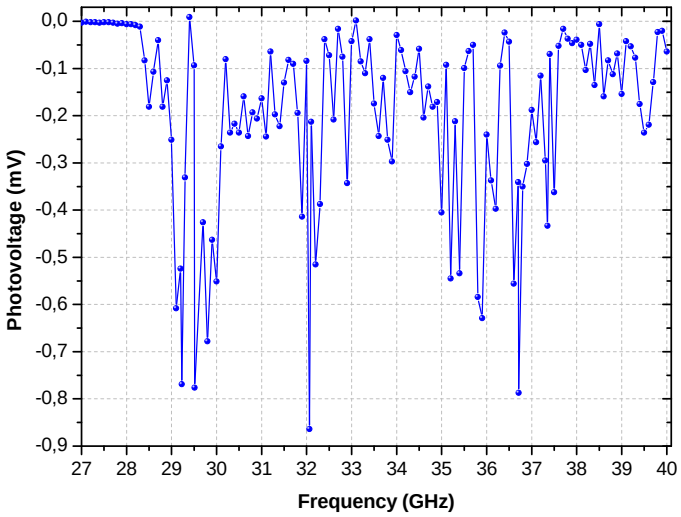


Figure 43: The variation of the photovoltage generated by the semicircular antidots with respect to the microwave frequency. The studied sample is at zero magnetic field and a temperature of 4 K.

A frequency of 36.71 GHz has been chosen for the carrier signal and the amplitude demodulation tests have been performed. The digital oscilloscope has been connected between contacts 2 and 3 of the first studied sample to check the response of the semicircular antidots region (see Figure 42(a)). Figure 44 represents the semicircular antidots response to the received signal with a sine wave modulating signal of 100 Hz and an output power of 16 dBm, when varying the amplitude modulation depth[2] from 10 % to 90 %. Increasing

2 The amplitude modulation depth (also called modulation index) is the measure of the amplitude variation surrounding an unmodulated carrier. In general, the modulation depth is a measure of the efficiency of the

the modulation depth causes an increase of the power level received by the sample. These results show that the Ratchet sample could demodulate the received signal. During the demodulation tests, the polarity of the demodulated signal contacts was reversed which explains the phase shift of about $\pi/2$ between the modulating and the demodulated signal. A distortion of the demodulated signal could be noticed when the modulation depth increases. While obtaining this distortion, a warning message "UNLEVELED" appears on the display screen of the synthesized signal generator. This message indicates that the RF output goes unleveled, which is normally caused by exceeding the specified leveled-power rating and thus causing a distortion of the modulated signal generated from the signal generator. Therefore, in this case, the observed distortion returns to the level of the source producing the modulated signal and it is not representing the sample response.

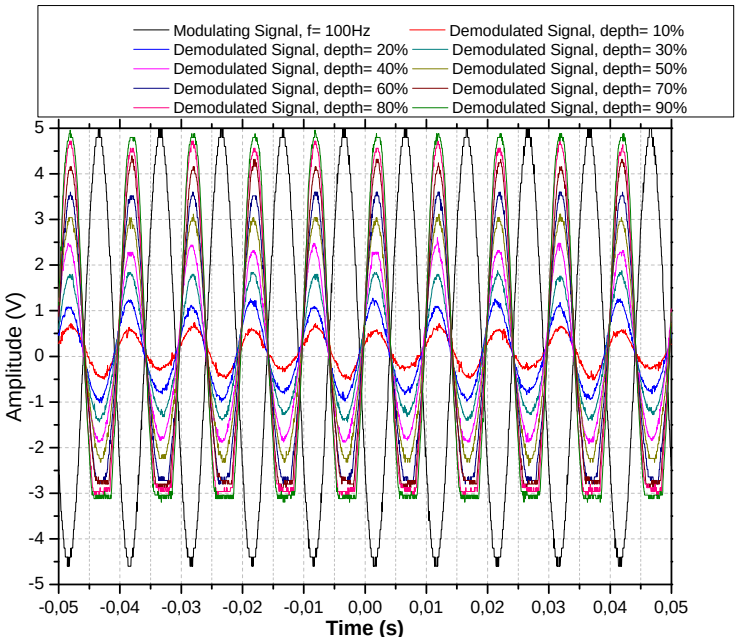


Figure 44: Semicircular antidots region response to the applied amplitude modulated RF signals with different modulation depths. An output power of 16 dBm, a carrier signal of f = 36.71 GHz and a sine wave modulating signal of f = 100 Hz have been used.

The response of the 2DEG unpatterned region and the circular antidots region to a received amplitude modulated RF signal has been also tested by connecting the oscilloscope between contacts 3 and 4 then contacts 4 and 5 respectively. These two regions could also demodulate the received signal and their responses are identical, as shown in Figure 45. According to the interpretation of LNCMI team, this is due to the fact that the unpatterned and the circular antidots regions exist on the same studied sample where the semicircular antidots are patterned.
As a result, when radiating the studied sample with a modulated signal, the semicircular antidots region produces a photovoltage which amplitude varies according to the amplitude of the received signal. The photovoltage change, generated from the semicircular antidots, produces a charge gradient in the entire 2DEG of the sample and thus

modulator and it is normally expressed as a percentage. To avoid distortion, modulation depth must not exceed 100 % [40].

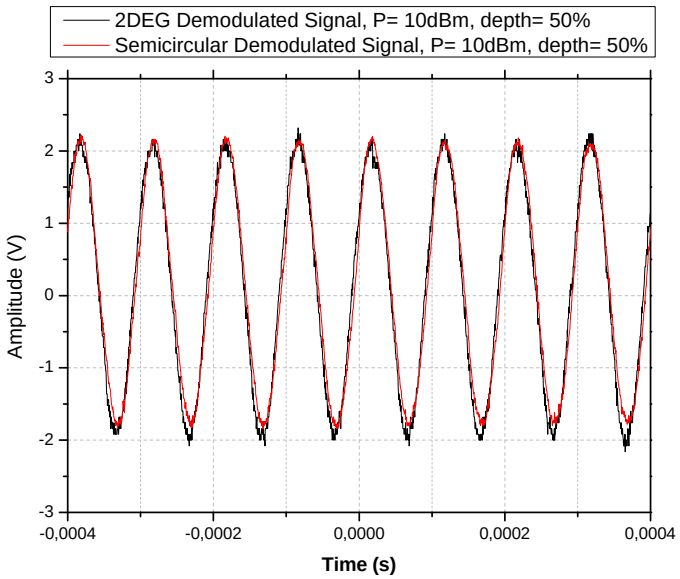


Figure 45: 2DEG and the circular antidots region response to the applied amplitude modulated RF signal for an output power of 10 dBm and a modulation depth of 50 %. A carrier signal of f = 36.71 GHz and a sine wave modulating signal of f = 10 KHz have been used.

the unpatterned and the circular antidots regions are affected and they also produce a photovoltage which is influenced by the amplitude modulation. In order to validate this interpretation, more experiments should be performed on samples containing only symmetrical or only asymmetrical antidots.

The demodulation test has been also applied on the virgin sample, without antidots (see Figure 42(b)) using a carrier signal of f = 36.71 GHz. Normally, this virgin sample should represent no response to the modulated signal. Two types of waveform have been tested: sine wave (Figure 46(a)) and pulse wave (Figure 46(b)). However, an unexpected photovoltage variation has been observed, as shown in Figure 46. This virgin sample produces a demodulated signal with a small amplitude compared to the modulating signal, for an output power of 10 dBm, a modulating signal of f = 100 Hz and a modulation depth of 50 %.

Figure 47 represents another test peformed on the virgin sample which consists of increasing the ouptut power between 5 to 18 dBm. The aim of this test is to check the influence of increasing the power level on the amplitude of the demodulated signal. It has been noticed that there is a slight increase of the amplitude compared to a large increase of the power received by the sample: the amplitude is 0.3 V when the power is 5 dBm, then it changes only to 0.4 V when the power increases to 18 dBm.

It could be concluded from these results that the virgin sample is less sensitive to the increase of the power level which is in contradiction with the characteristics of the Ratchet photovoltage produced by a sample with semicircular antidots (see Figure 8 and Figure 10(e)).

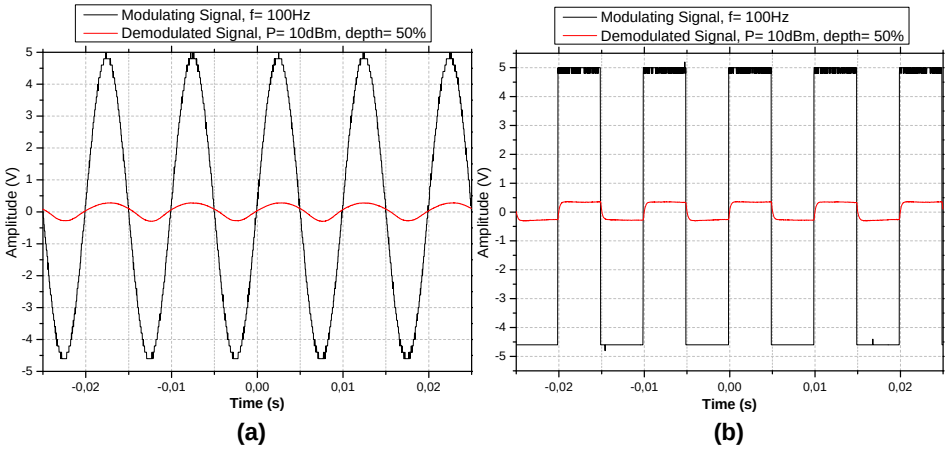


Figure 46: Virgin sample response to the applied amplitude modulated RF signal for an output power of 10 dBm and a modulation depth of 50 %. (a) Sine wave modulating signal, (b) pulse wave modulating signal, with f = 100 Hz and a carrier signal of f = 36.71 GHz.

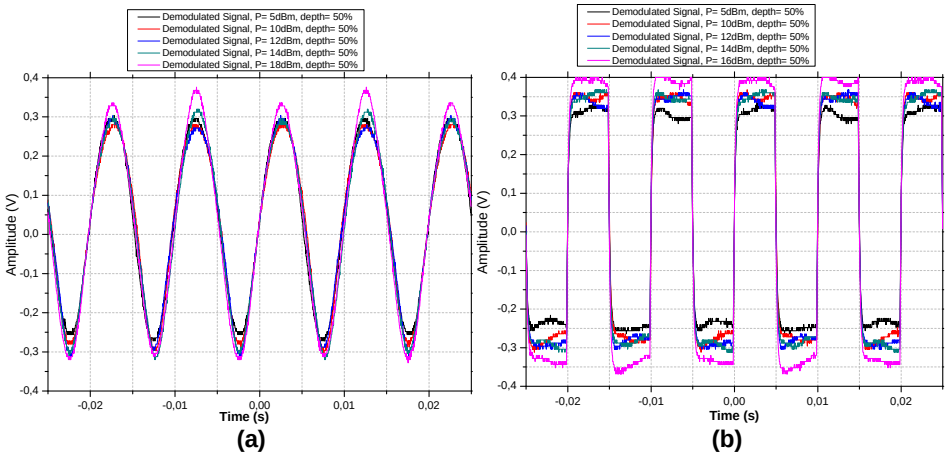


Figure 47: Virgin sample response to the applied amplitude modulated RF signals when varying the output power and fixing the modulation depth at 50 %. (a) Sine wave modulating signal, (b) pulse wave modulating signal, with f = 100 Hz and a carrier signal of f = 36.71 GHz.

4.5 PULSE MODULATION TECHNIQUES

After studying the Ratchet sample response to the analog amplitude modulation, the analog pulse modulation has been proposed to be applied on the studied sample since it plays an increasingly important role in the telecommunication domain. The analog pulse madulation [43] represents the twilight zone between analog and digital modulations. This type of modulation provides low power consumption, better quality communications, inexpensive digital circuitry and error detection and correction is easily implemented. Examples of the techniques that fall in the category of analog pulse modulation:

- Pulse Width Modulation (PWM).
- Pulse Position Modulation (PPM).

PWM and PPM have been widely accepted as control techniques in most of the electronic appliances. In the following, a brief description of these two techniques is presented.

4.5.1 *Pulse Width Modulation (PWM)*

It consists of varying the pulse width but while fixing the pulse period, i.e. varying the duty cycle, as shown in Figure 48. This type of modulation has been used in certain communication systems where its duty cycle has been used to convey information over a communication channel. In telecommunications, the widths of the pulses correspond to specific data values encoded at one end and decoded at the other.
Pulses of various lengths (the information itself) will be sent at regular intervals (the carrier frequency of the modulation).

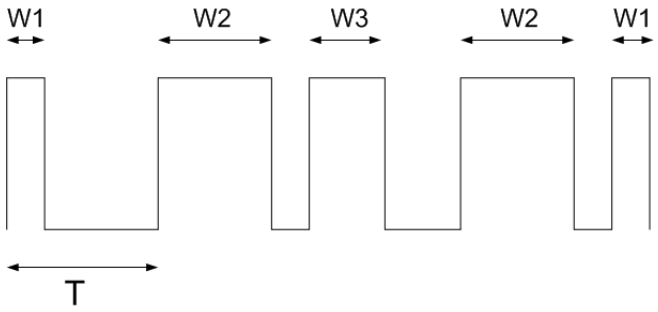


Figure 48: PWM; varied width and fixed period.

Therefore, this technique can deliver a variable amount of power to external devices [44]. It can be used in many applications which require a control of speed or any sudden changes, as controlling motors for robotics applications.

4.5.2 *Pulse Position Modulation (PPM)*

It is a pulse modulation technique that uses pulses that are of uniform height and width but displaced in time from some base position, as shown in Figure 49.
An advantage of PPM is that it could provide higher noise immunity than PWM [45]. Since the PPM pulses have a varied period, a clock signal has to be used to synchronize between the PPM receiver and the transmitter.

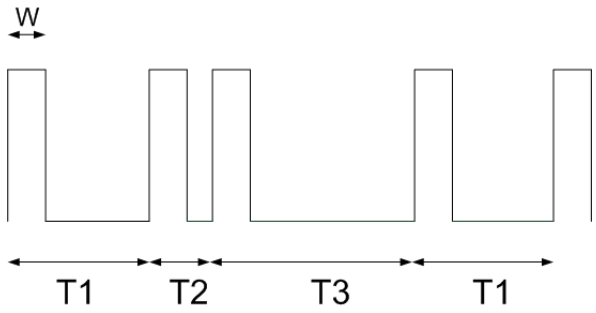


Figure 49: PPM; fixed width and varied period.

Besides the many advantages of these two modulation techniques, they represent the simplest methods among the other modulation techniques that could be easily applied on the studied sample taking into consideration the complexity of the experimental setup that exists in Grenoble. The two techniques could be realized in a simple manner by connecting an electronic circuit to the carcinotron or the synthesized signal generator which are used to generate the carrier signal. The electronic circuit will generate a pulse signal that represents the modulating signal with varied duty cycle (PWM) or with varied period (PPM). This circuit could me a programmable mbed microcontroller or a simple function generator programmed with a developed LabVIEW program to vary the duty cycle or the period of the standard pulse signal generated from the chosen electronic circuit.

4.6 CONCLUSION

Exploratory test of applying an amplitude modulated RF signal on the Ratchet sample with semicircular antidots was introduced in this chapter. It has been observed that the region of semicircular antidots has the ability of demodulating the received signal.
This test has been also executed on a virgin sample, without patterned antidots. The virgin sample shows also a response to the modulation test which was not expected. However, it is worth mentioning that its response is not appropriate compared to the response of the sample with semicircular antidots. Therefore, the origin of the virgin sample response has to be investigated in order to evaluate what are the factors that could be added to the studied sample response and could affect the experimental results obtained.

5

EXPERIMENTAL INVESTIGATION OF THE RATCHET EFFECT IN GRAPHENE AT ROOM TEMPERATURE

5.1 ELEMENTARY PROPERTIES OF GRAPHENE

Graphene is made out of carbon atoms arranged in a hexagonal lattice on a honeycomb structure [46-48]. The current interest in graphene for Ratchet based applications can be attributed to four main reasons. First, as a bidimensional zero band gap semiconductor (Figure 50), the graphene shows an unusual semimetallic behavior [47]. Second, the mobility of graphene is high at room temperature. The mobility of graphene monolayer is $\sim 10000\,cm^2V^{-1}s^{-1}$ [46, 48-50] and for multilayers, the mobility is $\sim 3000\,cm^2V^{-1}s^{-1}$ at room temperature [49]. Third, electrons can propagate without scattering over large distances in graphene. For a mobility of $\sim 10000\,cm^2V^{-1}s^{-1}$ and an electron density of $\sim 5 \times 10^{12}\,cm^{-2}$, the mean free path is $\sim$ 400 nm [48]. According to this reason, an array of antidots could be fabricated with dimensions smaller that the mean free path of electrons at room temperature, which satisfy the third condition of the Ratchet Effect (see section 1.3). Fourth reason is related to the scalability of graphene devices to nanodimensions and its mechanical stability at room temperature.
All these reasons make graphene a promising candidate for the Ratchet Device fabrication at room temperature and thus enhancing its role in further efficient applications.

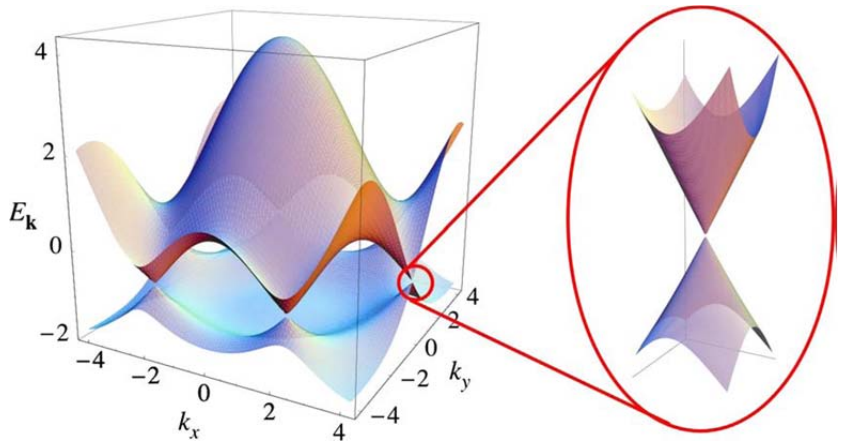


Figure 50: Graphene band structure showing the zero band gap [47].

5.2 THEORETICAL, NUMERICAL AND ANALYTICAL STUDY OF THE RATCHET ELECTRON TRANSPORT IN GRAPHENE

Many research works [51-55] have been established to explore the presence of Ratchet Effect and to study its properties in graphene flakes. L. Ermann and D.L. Shepelyansky [55] (ANR project partners) have studied numerically and analytically the Ratchet directed electron transport in graphene with the presence of semi-discs antidots and under microwave radiation. Moreover, they have compared between the Ratchet transport in

two-dimensional electron gas (2DEG) and in graphene, the Ratchet current has been found comparable in the two cases at low temperature. At room temperature, the mean free path in graphene is large which could allow having an important value of Ratchet current.

5.2.1 *Electrons motion in graphene*

This study has been based on Monte Carlo simulations with the Metropolis algorithm. In the Fermi-Dirac distribution, this approach keeps the non-interacting electrons with fixed Fermi energy EF and temperature T. They have explained the three factors that cause the motion of electrons in graphene with a periodic array of asymmetric antidots, under microwave radiation and with the absence of the magnetic field. These three factors are:

i. The linear polarized microwave force $f\cos\omega t$, where f is the amplitude of the microwave force and ω is the angular frequency.

ii. The force F_s due to the elastic collisions of electrons with the semi-discs antidots.

iii. The force F_i due to the scatter of electrons with impurities.

The dynamics of electrons in this model can be described by the Newton equations:

$$dP/dt = f\cos\omega t + F_s + F_i \tag{5.1}$$

dP/dt represents the rate of change of the electron momentum.
They have found that the velocity of electrons in graphene with asymmetric antidots can be calculated by:

$$|\overline{v_x}|/s = C_g\,(fr_d/E_F)^2\,, C_g = 1.3 \tag{5.2}$$

Where s is the electron effective light velocity in graphene $\approx 10^8$ cm/s, r_d is the antidots radius and C_g is a numerical factor that depends on the ratio of the antidot period to the antidot radius.

5.2.2 *Properties of Ratchet transport in graphene*

After computing and analyzing long trajectories of Ratchet flow, here are some of the Ratchet transport properties:

i. Decrease of the driving microwave force gives a reduction of the Ratchet transport.

ii. Increase of the temperature T, when it is comparable with the Fermi energy, causes the decrease of the Ratchet velocity if the rate of impurity is kept fixed.

iii. Increase of impurity scattering gives a reduction of the Ratchet velocity.

iv. Decrease of the frequency gives a slight increase of the Ratchet velocity for $\omega r_d/s \leqslant 0.5$. But the velocity drops with the frequency for $\omega r_d/s \geqslant 1$.

v. The dependence of the Ratchet flow polarization on temperature is weak. Also, in the case of graphene, unpolarized radiation gives an average current along x-axis, unlike the 2DEG case.

The Ratchet current is calculated by the relation $j = en_e\bar{v}$, where e is the electron charge and n_e is the electron density. Thus, the Ratchet current in graphene is calculated by:

$$j_g = 1.3en_e s\,(fr_d/E_F)^2 \tag{5.3}$$

5.3 PHOTOCURRENT GENERATION IN GRAPHENE MONOLAYER UNDER TERAHERTZ RADIATION

Recently, J. Karch *et al.* [52] have observed the generation of a photocurrent when illuminating the edges of a monolayer of graphene with circularly polarized terahertz radiation at normal incidence. Two types samples have been studied in [52]: (i) large area epitaxial graphene and (ii) small area exfoliated graphene. At room temperature, the carrier density is about $(2-7)\times 10^{12}\,cm^{-2}$ and the mobility is about $1000\,cm^2V^{-1}s^{-1}$. The sample has been radiated with NH_3 laser operating at wavelengths of λ = 90.5 µm,148 µm and 280 µm with pulses duration of ~ 100 ns, peak power P of ~ 10 KW and a repetition rate of 1 Hz. A photocurrent of several µA has been measured at room temperature.
The reason of the current generation has been explained, this is due to the symmetry breaking at the sample edges and thus causing an asymmetric scattering of the carriers under the terahertz radiation. This has been proved by scanning the laser spot across the sample, the current has maximum value when the laser spot is centered at the edge but it decays when the laser spot moves toward the sample center. The spot diameter is from 1 to 3 mm.
Furthermore, it has been observed that the current polarity reverses when changing the radiation helicity from left to right handed.
Under oblique incidence of circularly polarized terahertz radiation, J. Karch *et al.* [53] have reported that a photocurrent has been induced on a monolayer of graphene at room temperature. The voltage measured is due to crossed electric and magnetic fields that are rotating with the light frequency. To demonstrate that the photocurrent generation is due to the graphene illumination and not the substrate, the graphene layer has been removed from the studied sample and the photocurrent has been vanished.
Transverse and longitudinal currents have been observed; the signs of both currents change when reversing the direction of radiation incidence. However, when changing the helicity direction, only the polarity of the transverse current changes and the longitudinal current does not change its direction. For n- and p-type graphene samples, the polarity of the photocurrents is opposite.
Concerning the frequency dependence, the transverse and the longitudinal currents show two different behaviors. For $\omega\tau \ll 1$, the longitudinal current is independent of the frequency, where ω is the angular frequency of light and τ is the momentum relaxation time of electrons in graphene. For $\omega \to 0$, the photocurrent is maximum. While the transverse current increases with increasing $\omega\tau$ for $\omega\tau \ll 1$. For $\omega \to 0$, the photocurrent disappears, but when $\omega\tau \cong 1$, the current reaches its maximum. For $\omega\tau \gg 1$, both currents decrease with increasing the frequency.

5.4 CHARACTERIZATION AND RF MEASUREMENTS OF A GRAPHITE SAMPLE WITH A PERIODIC ARRAY OF ASYMMETRIC SHAPED ANTIDOTS

The first trial of fabricating a Ratchet Device based on graphite sample has been fabricated in CNRS-LPS (ANR project partner). This sample has been brought to CNRS-LAAS to perform a set of characterization and RF measurements.

5.4.1 *Sample description*

Figure 51 presents the different parts of the studied sample. The graphite layer has been deposited on a silicon dioxide substrate with a thickness of 300 nm. Metallic contacts of Ti/Au have been fabricated with a thickness of 30 nm. An asymmetric array of semi-discs shaped antidots has been perforted on the graphite flake using Ion Beam Etching Technology (IBE). The thickness of the graphite flake is about 10 nm, which corresponds to 20 layers of graphene according to [56].

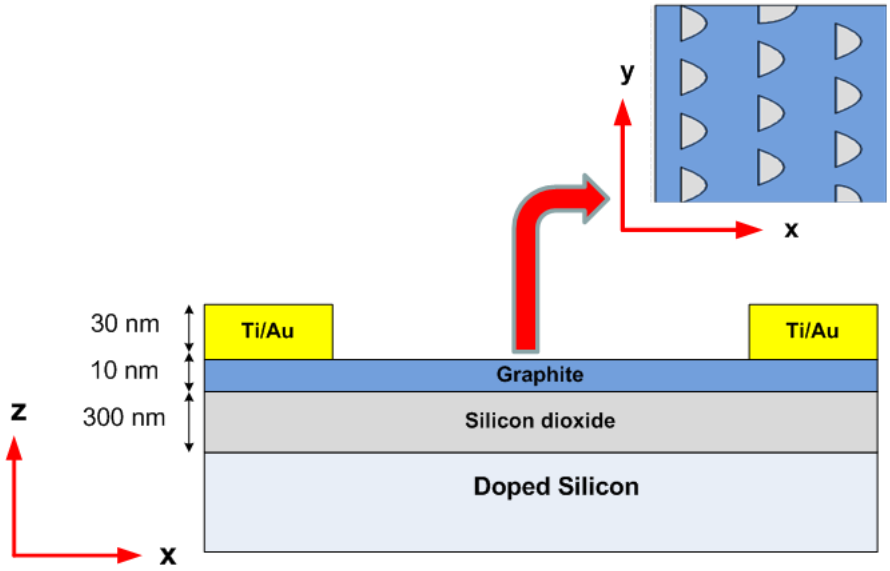


Figure 51: Schematic (cross section) of the graphite sample with an array of asymmetric antidots.

The optical microscope has been used to have an image of the sample contacts, the graphite flake between them (Figure 52) and to determine the sample dimensions. The horizontal contacts (compared to the antidots direction) are 2 and 6, while the vertical contacts are 3 and 1. The distance between the horizontal contacts is about 7.50 μm and it is about 7.85 μm between the vertical contacts. The overall area of the sample is about 2 mm^2.

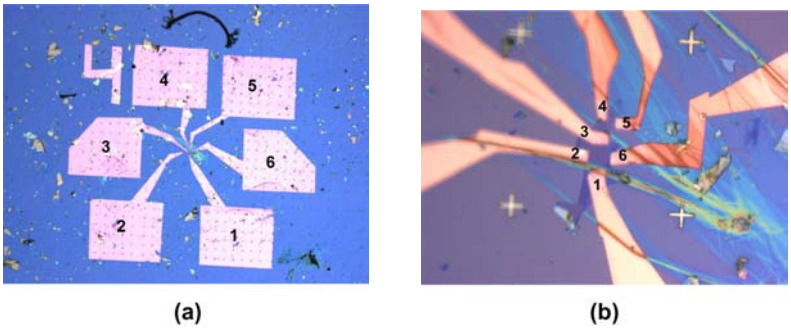


Figure 52: Image of the graphite sample observed with the optical microscope showing the contacts and the graphite flake between the contacts with a resolution of 5 X and 100 X in (a) and (b) respectively.

An Atomic Force Microscopy (AFM)[1] has been used in order to study the shape and to determine the exact dimensions of the antidots. Between the sample contacts, the array of antidots has been fabricated with a period of 721 nm, as shown in Figure 53(a). 53(b) illustrates one single antidot with a radius of 114 nm and a depth of 4 nm.

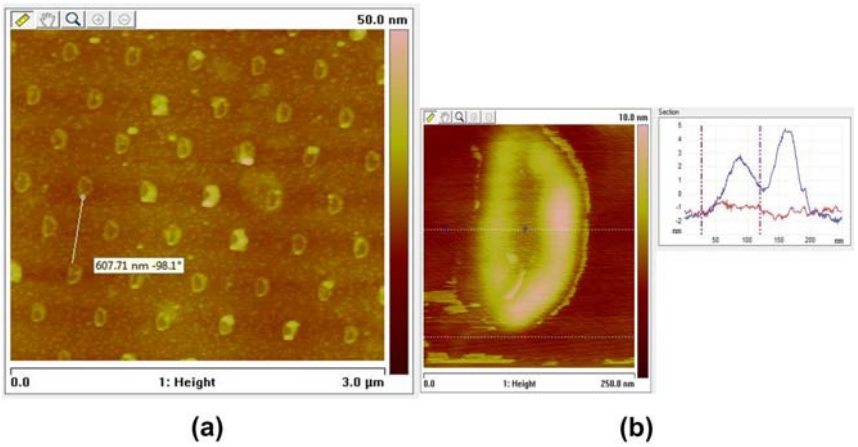


Figure 53: Image of the graphite sample observed with the AFM. (a) The region of antidots with a period of 721 nm, (b) one single antidot with a radius of 114 nm and a depth of 4 nm.

5.4.2 *I-V measurements*

The current-voltage (I-V) measurements have been performed to extract the resistivity of the sample and to check the contacts resistance. Two techniques have been used in this type of measurements; the first one (see Figure 54(a)) consists of a function generator and a resistance of 1 MΩ connected to the sample, a small DC current of about 1 uA is injected between the sample contacts. Measuring the DC voltage between each two contacts using the nanovoltmeter, we can calculate the resistance by R = V/I. The second technique (see Figure 54(b)) has the same concept of the first one but it is more efficient. It consists of a cascade probe station where the sample is put on a vacuum chuck used to secure the sample by holding it firmly in a fixed position. A Keithley 4200 tester injects a small amount of current and measures the voltage and the resistance across the sample.

5.4.3 *RF measurements at room temperature*

As a first trial, the sample has been placed on a microwave probe station and has been illuminated by microwave radiation using a horn antenna that operates in 4–40 GHz frequency range with an average gain of 4–15 dBi. Two DC probes deposited on the sample contacts and connected to a voltmeter have been used to measure the DC voltage. However, no DC voltage has been observed when radiating the sample. The second trial consists of applying the RF signal on the sample back gate using RF probe. As shown in Figure 55, at f = 70 MHz, a maximum voltage has been observed between contacts 1 and 3 (see Figure 52). Its value is about 2 mV for a signal power of 0 dBm and it is about 10 mV when the applied power is 10 dBm. Unfortunately, the sample has been damaged by

1 AFM is a very high-resolution type of scanning probe microscopy. It is one of the foremost tools for imaging, measuring, and manipulating matter at the nanoscale level. AFM images are obtained by measurement of the force on a sharp tip created by the proximity to the surface of the sample [57].

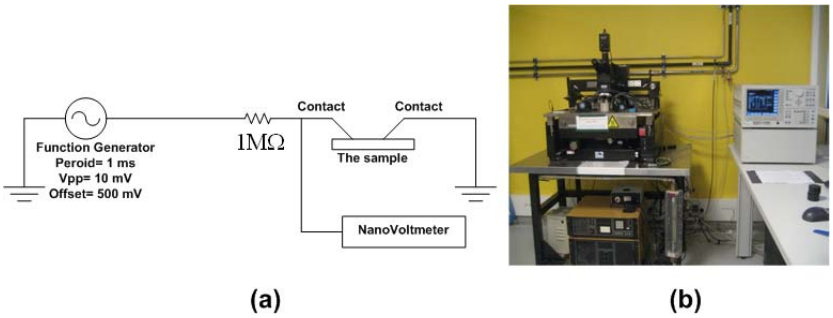


Figure 54: (a) Schematic of the first technique used to measure the resistance. (b) Photo of the second technique used: I-V small signal Test Probe Station.

an electrostatic discharge and no more measurements have been performed in order to reproduce and explain the voltage found around 70 MHz.

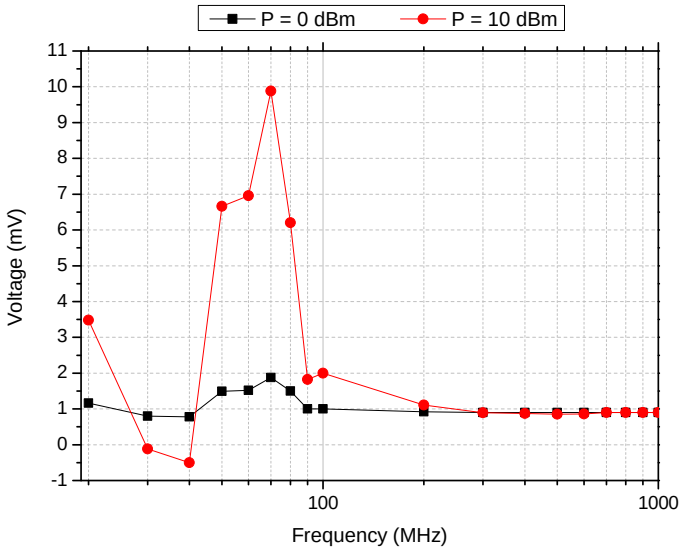


Figure 55: Voltage variation with respect to frequency for a signal power of 0 and 10 dBm.

5.5 DESIGNS, CHARACTERIZATIONS AND RF MEASUREMENTS OF MONOLAYER AND BILAYER GRAPHENE SAMPLES WITH A PERIODIC ARRAY OF ASYMMETRIC SHAPED ANTIDOTS

CNRS-LAAS has initiated an exploratory work of Rachet Effect on exfoliated graphene. A series of monolayer and bilayer exfoliated graphene flakes deposited on Si/SiO2 substrates have been acquired from Graphene Industries, Manchester. The samples substrates are made of oxide with a thickness of 290 nm thermally grown on high resistivity silicon. Using a simple matlab code based on analytical equations given by [37], we could study the effect of the silicon substrate thickness on the incident electric field used to radiate the sample (see Appendix B). As an example, it has been found that for a silicon substrate thickness of 300 µm and an operating frequency of 50 GHz, only 30 % of the incident electric field could be obtained on the sample surface.

Dr. G. Deligeorgis from CNRS-LAAS has performed the contacts process and the antidots patterning. Different challenges have been faced when fabricating the metallic contacts, as the resistance of the contacts is a major issue in device performance [58], and the realization of the antidots array in the studied samples. Our aim is to fabricate a new optimised Ratchet Device based on graphene that could work at room temperature and suitable for many practical applications.

5.5.1 *Sample designs*

The limited size of the available samples presents a limiting factor to the antidots patterning process. Therefore, several designs have been made in order to optimize the fabrication process and to explore the Ratchet Effect adapted to the material size. All the designs are based on Van der Pauw [59] structure to ensure the system symmetry. In the following, the realized designs are presented in historical order.
Figure 56 represents the initial design "A" which is the first trial of fabrication. This design requires a graphene area of 60 × 60 mm^2. In this figure, the blue area symbolizes the graphene flake where the antidots array is supposed to be patterned, while the green areas represent the metallic contacts.

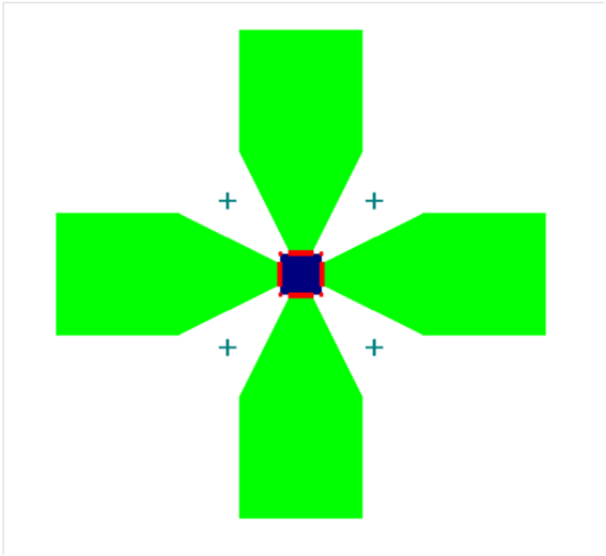


Figure 56: Initial design "A" of Ratchet Device.

Afetrwards, a first improvement has been performed in the next design "B" (shown in Figure 57). This improvement consists of reducing the metallic surfaces surrounding the graphene flake. This could increase the field intensity on the graphene area and hence increasing the Ratchet induced photovoltage.
Figure 58 shows the final improved design "C", where the shape of the graphene has been re-designed. Since a large area of graphene is not easy to obtain, the graphene flake has been placed in a manner to have a lozenge shape between the metallic contacts. This position ensures increasing the interaction length and the number of antidots between each two opposite contacts. The size of the graphene flake obtained is 50 × 50 mm^2. This reduced size minimizes the risks of having a crack or an extended defect on the chosen

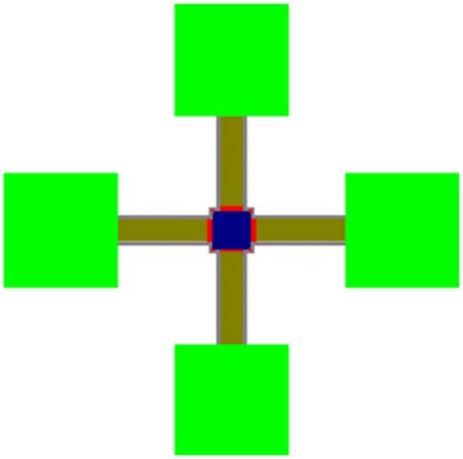


Figure 57: Design "B": metallic areas are minimized to increase the field interaction.

area that could alter the behavior of the device. Also in this design, the surrounding metallic surfaces have been minimized.

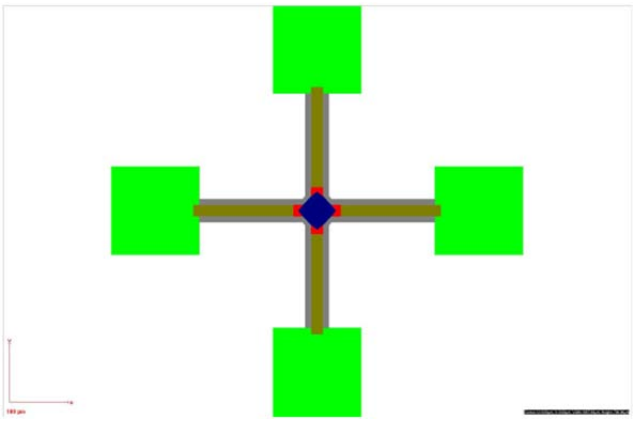


Figure 58: Design "C": graphene placement is optimized to increase the interaction length and the number of antidots between the metallic contacts.

5.5.2 *Graphene sample selection*

A large graphene flake has to be chosen in order to pattern the array of antidots. Figure 59 illustrates the image of graphene monolayer and bilayer flakes.
However, one of the major issues in searching for an appropriate flake is that large flakes often have cracks that are not visible through optical imaging. Therefore, a method to determine the existence of cracks has been found. Using Kelvin Probe Force Microscopy (KPFM)[2], the surface potential of the flake is measured which indicates if the flake surface is homogeneous (without cracks) or not.

2 KPFM is a method to measure the contact potential difference between different materials with high spatial resolution [60].

As shown in Figure 60(a), no cracks appear in the optical image of the graphene flake. However a sharp identification of cracks and areas that have poor adhesion to the substrate are identified in the KPFM image of the same flake, as shown in Figure 60(b).

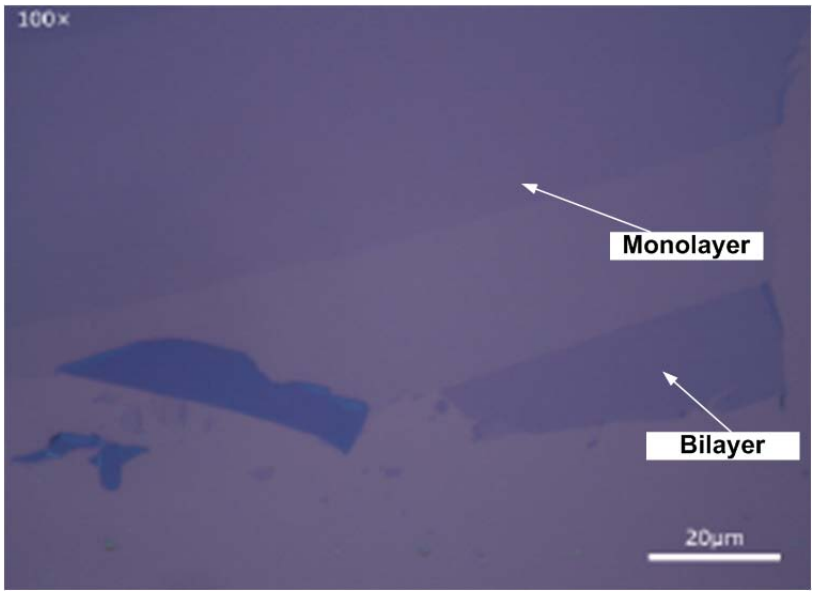


Figure 59: Optical image of graphene monolayer and bilayer flakes. The difference in contrast corresponds to different number of layers.

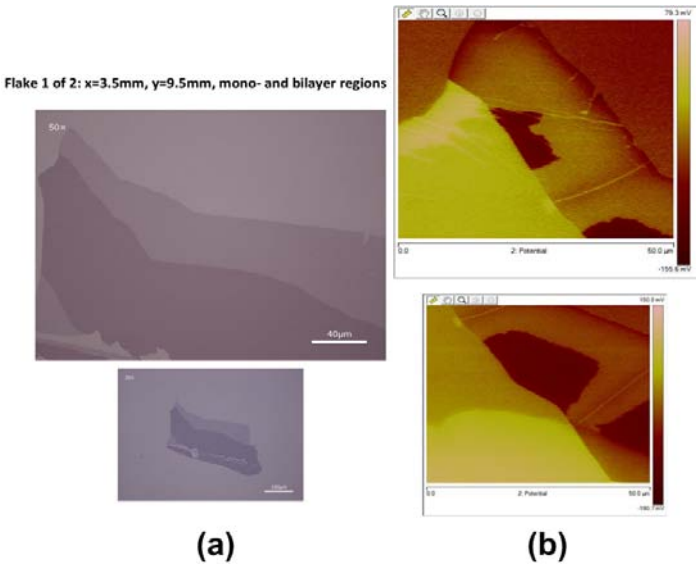


Figure 60: (a) Optical image of a graphene flake, no cracks appear in the flake area. (b) KPFM image of a graphene flake showing the craks.

5.5.3 *Antidots patterning*

Etching asymmetric nano-antidots on the chosen graphene flake is not an easy task. E-beam lithography has been used to pattern shapes on PMMA (electron sensitive resist). ICP plasma etching has been performed to perforate the graphene. Optimization of etching time and power has been implemented to obtain a proper transfer of the pattern on the graphene. Moreover, the e-beam process has been optimized to control size and shape of the antidots.
Figure 61 shows the dimensions of an array of arc shaped antidots that has been realized by Dr. G. Deligeorgis in his first trial of Ratchet Device farication. However, this device has shown some defects and it has not been used in the RF measurements. The new fabricated devices have been patternened with the same way as the first device.
The radius of antidot is 36.75 nm, the arc thickness is 12.3 nm and the period between antidots is 197.3 nm. The depth of antidot is 2.081 nm, as illustrated in Figure 62.

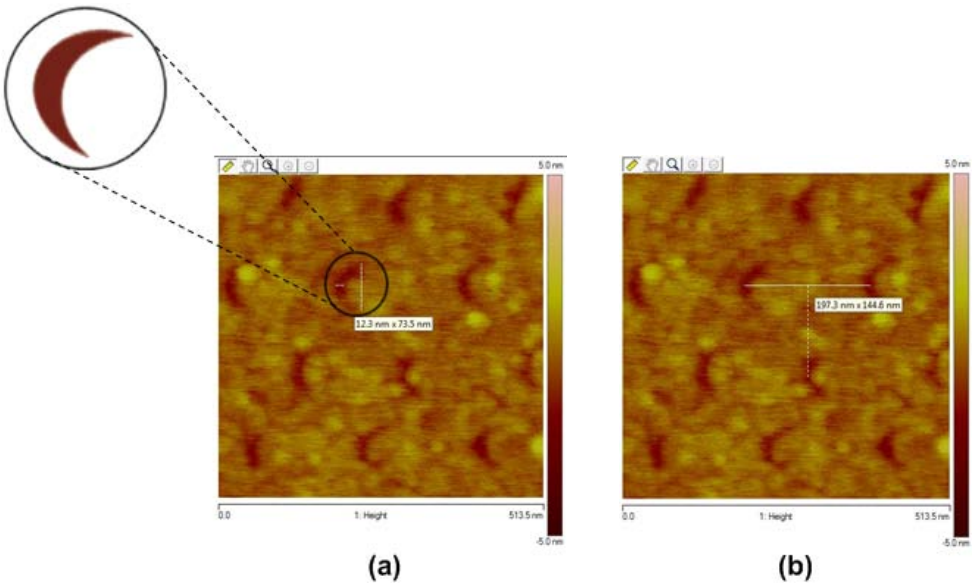


Figure 61: AFM image of the arc shaped antidots. (a) Antidot radius is 36.75 nm and its thickness is 12.3 nm, (b) period between antidots is 197.3 nm.

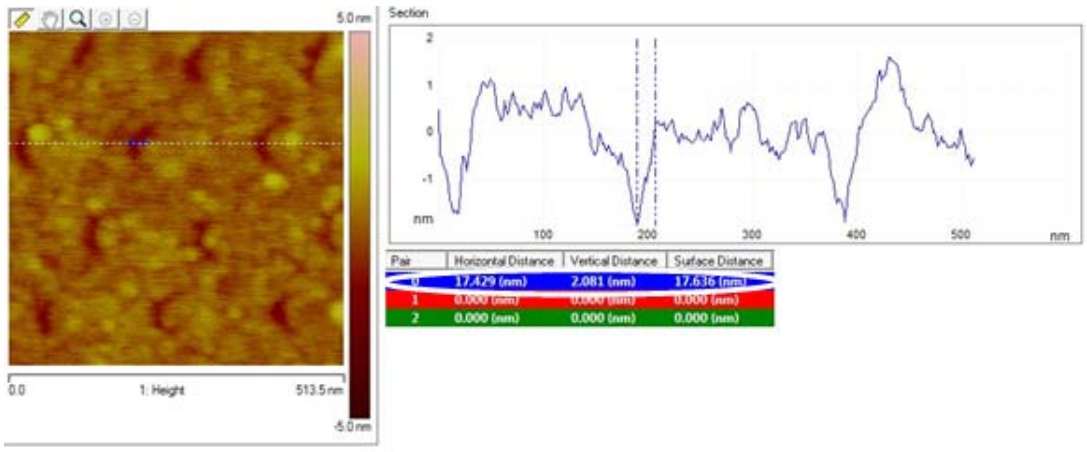


Figure 62: AFM image showing the antidot depth of 2.081 nm.

5.5.4 *Mobility and electron density*

The mobility and the electron density of the studied sample have been measured before attempting to evaluate the presence of the Ratchet Effect. The Hall Effect Measurement System used in performing this characterization measurement is shown in Figure 63. A mobility of about $360\,cm^2V^{-1}s^{-1}$ and an electron density of about $1.2 \times 10^{13}\,cm^{-2}$ have been obtained for the graphene bilayer. However, for the monolayer sample, it has been found a reduced mobility of about $31\,cm^2V^{-1}s^{-1}$ and an electron density of about $1.5 \times 10^{13}\,cm^{-2}$. These measured values are not similar to the values mentioned in the other research works for a bilayer and monolayer flakes of graphene [46, 48-50]. This could due to the presence of the array of antidots that perforates the graphene flake.



Figure 63: HL5500PC Hall Effect Measurement System.

5.5.5 *Description of the experimental setup used to study the Ratchet Effect at room temperature*

Different electromagnetic illumination techniques have been proposed in [28] to radiate the studied sample with microwave energy at room temperature. A standard gain horn antenna has been chosen to be used in the RF measurements, as shown in Figure 64. It operates in the 26.5–40 GHz frequency band with a gain of 20 dBi and it has been connected to RF signal generator (Anritsu MG3694B) which represents the microwave source. The sample has been placed on a polycarbonate plate with a thickness of 5 mm. This plate has been pierced in its center to allow the vacuum to pass through and thus fixing the sample at its place without moving during measurements. To maintain the horn antenna in good position above the sample and to move it in different directions, a motorized arm has been used that can rotate step-by-step in 360 degrees around the sample.

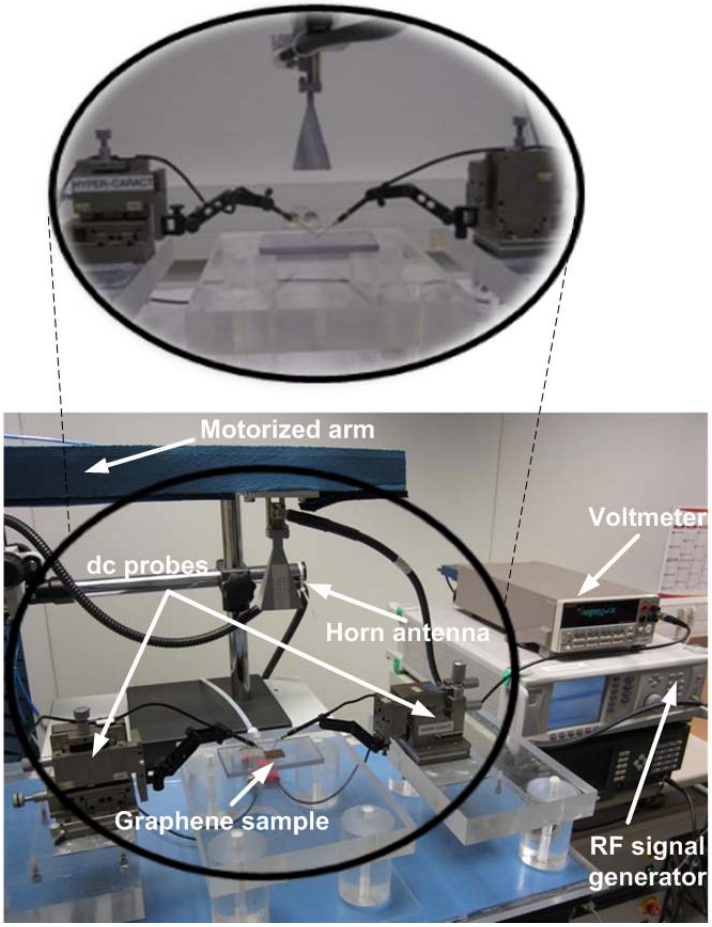


Figure 64: Photo of the experimental setup with its different parts used in measuring the Ratchet Effect.

To measure the DC induced voltage, a digital multimeter with high accuracy (Keithley 2000) has been used and has been connected to DC probes that have been laid on the sample contacts. Figure 65 illustrates how the electric field polarization angle changes while moving the horn antenna around the sample. The horizontal contacts 1 and 3 (parallel to x-axis) have been used in measuring the induced voltage. Concerning the polarization angle, the angle 0° corresponds to an electric field parallel to x-axis. According to the horn antenna aperture, this polarization angle is obtained when the horn antenna is placed at the center of the probe station.

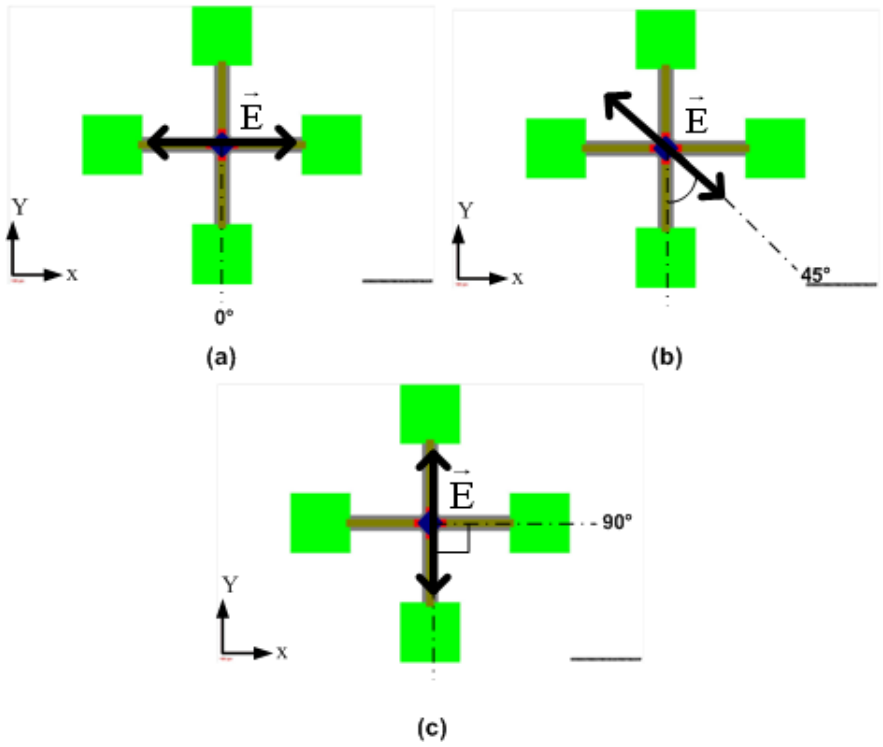


Figure 65: Schematic representing the variation of the electric field polarization angle over the Ratchet Device.

The microwave probe station used in measurements is made of plexiglass and all the metallic parts have been covered with absorber materials to reduce the electromagnetic reflections. In order to test the reflection on the sample level, the reflection coefficient S11 of the setup has been measured, without the presence of the sample, for the frequencies from 26.5 to 40 GHz, when the distance between the antenna and the probe station is about 16 cm.
Three cases have been taken into consideration: the first case consists of placing a metallic plate between the DC probes, the second one is by putting an absorber between the probes, and the third one is with the presence of the polycarbonate plate only. The aim of this measurement is to compare the level of reflection of the station with the polycarbonate plate, which is the actual case, with the worst case of reflection (metallic plate) and the best case (absorber).
As presented in Figure 66, it has been found that S11 has a value of -12 dB for the metallic plate case, compared to -18 dB for the other two cases. Moreover, the reflection coefficient S11 of the setup has been measured, with the presence of the sample, but it has given

the same response as in the absence of the sample. Therefore, the small sample does not affect the reflection level of the setup and this low reflection setup will not influence on the experimental results.

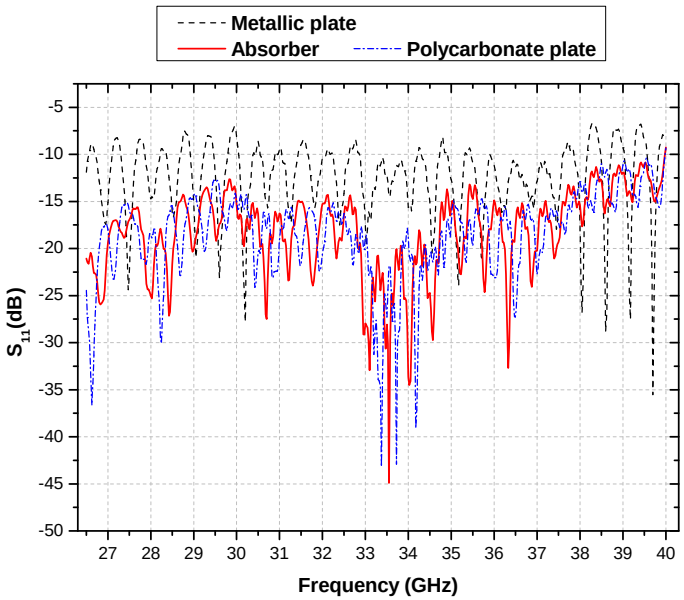


Figure 66: Reflection coefficient S11 of the setup measured in three different cases: Metallic plate, Absorber and Polycarbonate plate.

5.5.6 *Experimental conditions and the results obtained*

A monolayer and a bilayer graphene flakes with patterned arc shaped antidots have been used to study the Ratchet Effect at room temperature. While testing the two samples, many observations have been reported on the samples response. It has been noticed that the bilayer flake shows a better response to the microwave radiation than the monolayer flake. This has been observed for a wide range of frequencies and power. For example, at a frequency of 30 GHz and a power of 20 dBm at the RF generator output, the voltage generated from the bilayer graphene sample is around 13 µV, while the monolayer flake has produced a voltage around 3.5 µV. Therefore, we have focused our RF study on the bilayer graphene flake.
Since the generated voltage is in the µV range, it has been observed that the induced voltage is unstable and fluctuating. This has forced us to perform a statistical study to determine the sample behavior and to calculate the mean value of the generated voltage. These observations had defined the experimental conditions that have been satisfied in the Ratchet Effect tests.
A reference sample (without antidots) has been fabricated in parallel with the patterned samples to compare their response to the microwave radiation. Unfortunately, this reference sample has been damaged during the contacts fabrication process.

5.5.6.1 Statistical study

Under fixed experimental conditions, a significant change of the generated voltage has been noted. Figure 67 represents the variation of the generated voltage with respect to

time, when the electric field is parallel to the horizontal contacts of the sample (angle = 0°). It has to be mentioned that at this configuration (electric field is parallel to the contacts used in measuring the voltage), we ensure that the system symmetry is only broken due to the presence of antidots that cause the voltage generation. The horn antenna is at a distance of about 16 cm above the sample, the value of the frequency used is 30.75 GHz and the power level is 20 dBm at the RF generator output. This measurement has been realized using a LabVIEW program which consists of switching ON and OFF the RF generator and measuring the voltage in the two states. Using this method enables us to observe the influence of the microwave radiation on the sample response and to evaluate the noise level when the RF generator is turned off. As shown in Figure 67, we can observe an oscillation of the produced voltage under the microwave radiation.

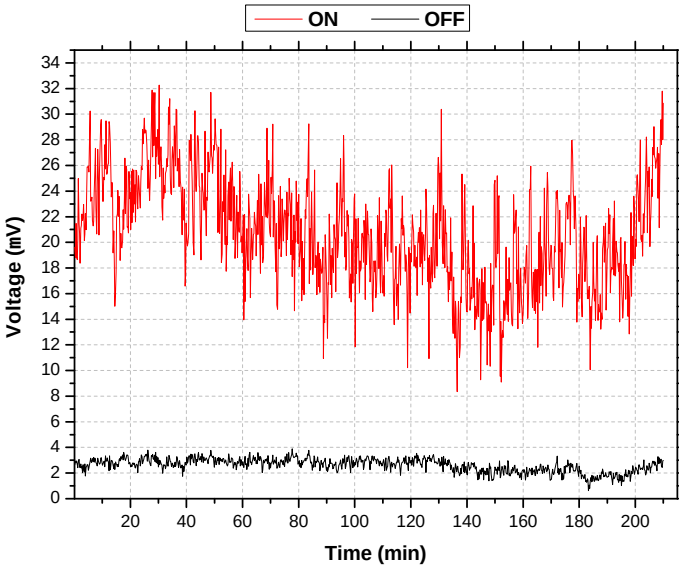


Figure 67: Voltage variation with respect to time produced from a bilayer graphene flake with an array of arc shaped antidots. ON signifies that RF generator is switched ON, OFF signifies that RF generator is switched OFF.

In order to draw a conclusion on the effect of changes in the studied samples response, a statistical study has been conducted. This study is based on taking a large number of measurements (e.g. 1000 points of measurements) and then evaluating the sample behavior to verify if it represents a Gaussian distribution. A Gaussian distribution curve is a statistical function that describes how data behaves around their mean value. A Gaussian shaped curve is characterized by the concentration of the majority of number of elements in the center and the decrease of this number on either side of the curve. This distribution depends on two factors, the mean and the standard deviation. The mean determines the Gaussian distribution center which contains the highest number of occurrence of an element and it represents the average value of all the data values obtained. The standard deviation determines the height and width of the gaussian curve, which means measuring the amount of deviation contained in the data obtained.
In general, a Gaussian distribution translates to a less tendency of the data to produce unusually extreme values. It also signifies that the data is symmetrical and thus any outcome value will lie within a range around the center. Using the same values of frequency, power, antenna distance and polarization angle as the measurement presented in Figure 67, we plot the histogram of the generated voltage under microwave radiation

for 1000 points of measurements, as shown in Figure 68. The voltage values presented in this figure is the difference between the voltages measured when the RF generator is turned on and their values when it is turned off. The sample response represents a Gaussian distribution around a mean value of 18 µV and a standard deviation of 4 µV. Therefore, it could be concluded that in this case there is a deviation of 23 % from the mean value of all the data obtained for 1000 points of measurements. Without changing the experimental conditions, this measurement has been repeated several times to verify the reproducibility of the observed phenomenon. For each measurement, we have found that the values obtained were so close.

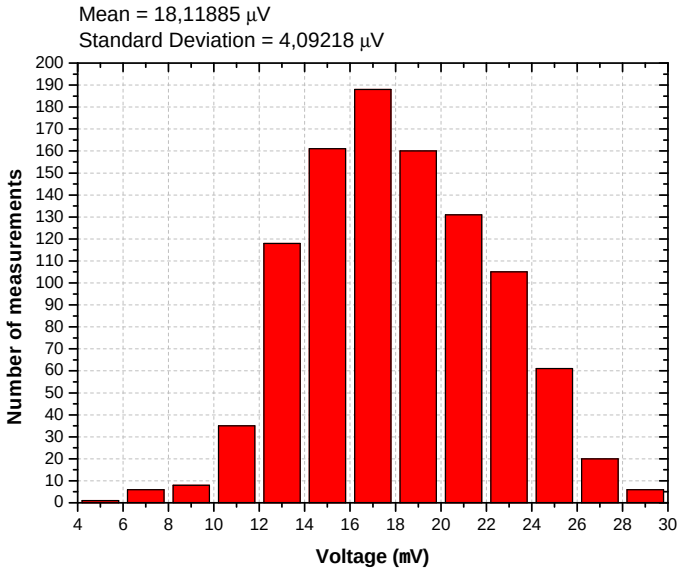


Figure 68: Histogram of the produced voltage for 1000 points of measurements at angle = 0°, the applied power is 20 dBm and the frequency is 30.75 GHz.

Moreover, this statistical study has been tested for other polarization angles of the applied electric field. Figure 69 shows the histograms of the sample response for angle = 15° and -15°. For these two cases, the sample represents also a Gaussian distrubution. In addition, it has been noticed that their mean voltage values are nearly the same. This mean value which is around 11 µV is less than the value obtained for angle = 0°.
Another example is presented in Figure 70 which illustrates the sample response for angle = 25° and -25°. The same observation has been noticed that the mean voltage values for these two angles are almost identical, around 5 to 6 µV, which is less then the mean values obtained for angle = 0°, 15° and -15°.
Since a variation of the voltage value with respect to the polarization angle has been observed, this has encouraged us to implement a further study on the effect of the applied electric field polarization on the sample response. This study is presented in details in the next subsubsection.

5.5.6.2 Impact of the polarization angle

The presence of the motorized arm that holds the horn antenna (see Figure 64) has facilitated the realisation of a detailed investigation of the influence of the polarization angle change on the voltage produced from the studied graphene sample. At a distance of 16 cm from the sample, the position of the horn antenna has been varied between -90° to

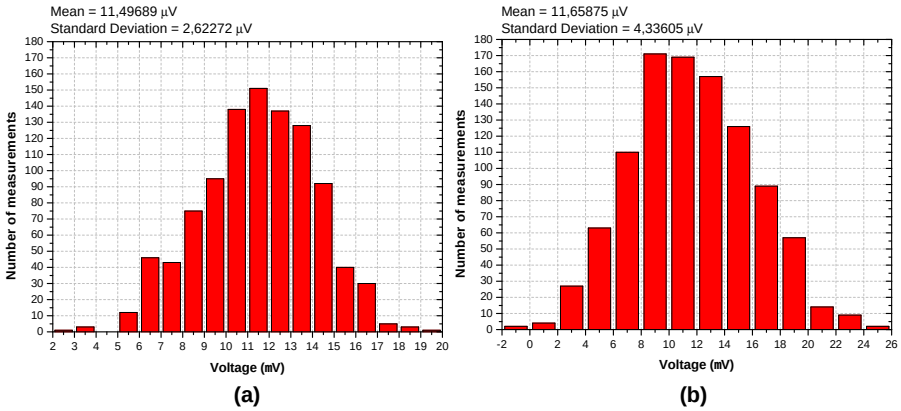


Figure 69: Histogram of the produced voltage for 1000 points of measurements at: (a) angle = 15° and (b) angle = -15°, the applied power is 20 dBm and the frequency is 30.75 GHz.

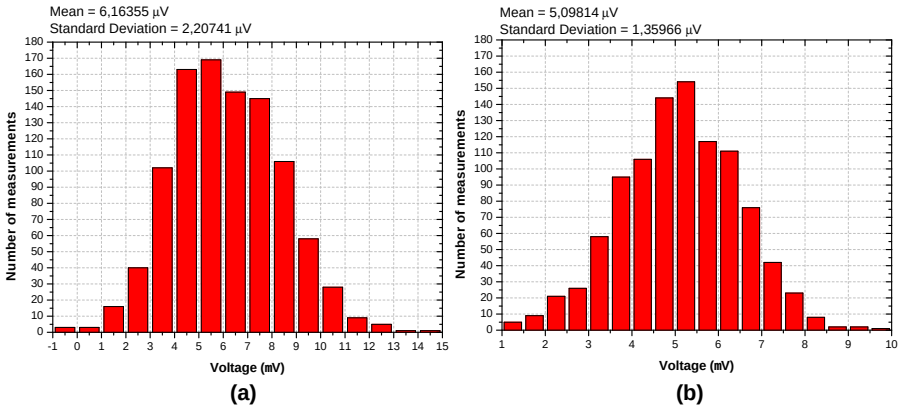


Figure 70: Histogram of the produced voltage for 1000 points of measurements at: (a) angle = 25° and (b) angle = -25°, the applied power is 20 dBm and the frequency is 30.75 GHz.

+90° around the sample with a step of 5°, using a cable of 1.5 m length and an attenuation of about 3 dB. At a frequency of 30.75 GHz and an injected power of 20 dBm, it has found that the voltage has a maximum value when the angle equals 0°. However, the voltage vanishes when the polarization angle is ±90°. Figure 71 represents the voltage variation with respect to the polarization angle from -30° to +30°. For each angle, a statistical study based on 1000 points of measurements has been performed (as described in the previous subsubsection), the mean value and the standard deviation have been calculated and illustrated in the figure below. Besides, an error of about 2° has been estimated for each polarization angle.

Nevertheless, a problem of vibrations on the probe station caused by the RF signal cable forced us to apply some modifications to the experimental setup and to the studied sample to enhance the experimental conditions. First, the cable has been replaced by a longer one of 4 m length and an attenuation of about 7 dB. To compensate for the cable loss, we have reduced the distance between the sample and the antenna. The new distance has been fixed to 6 cm instead of 16 cm used in the previous measurement. Second, the motorized arm has been replaced by another antenna support independent of the probe station to reduce the vibration of the station while moving the antenna. Third, a compressed air system has been added to the probe station to isolate the sample

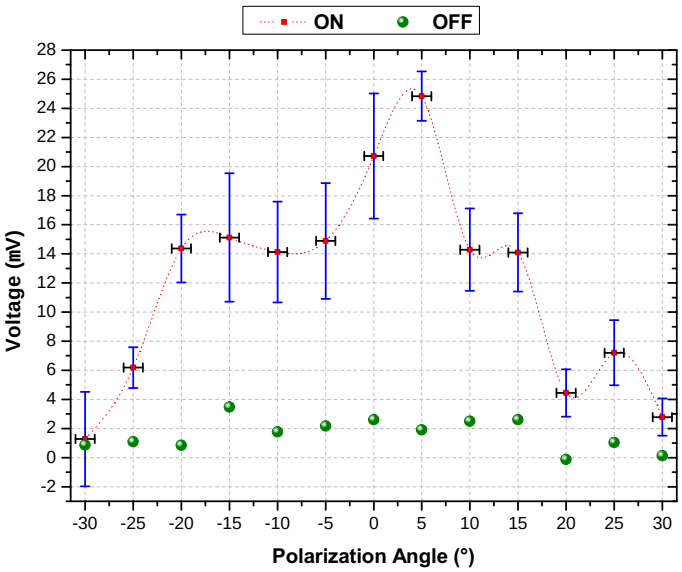


Figure 71: Voltage variation with respect to the polarization angle. The horn antenna is at distance of 16 cm from the sample, the applied power is 20 dBm, the frequency is 30.75 GHz and the attenuation of the cable used is about 3 dB.

from any surrounding vibrations. Concerning the sample, larger metallic pads have been made on the sample substrate near the edges. This makes the operation of putting the DC probes on the sample contacts easier and safer as we do not need to use a microscope and the DC probes will be far from the graphene layer that exists at the center.
Afterwards, the reflection coefficient S11 of the setup has been remeasured, with the presence of the sample, as shown in Figure 73. The aim of this measurement is to check if these modifications have influenced on the reflection level measured before (see Figure 66). The new value is around -15 dB compared to -18 dB obtained before modifying the setup, which is still suitable to perform the RF measurements.

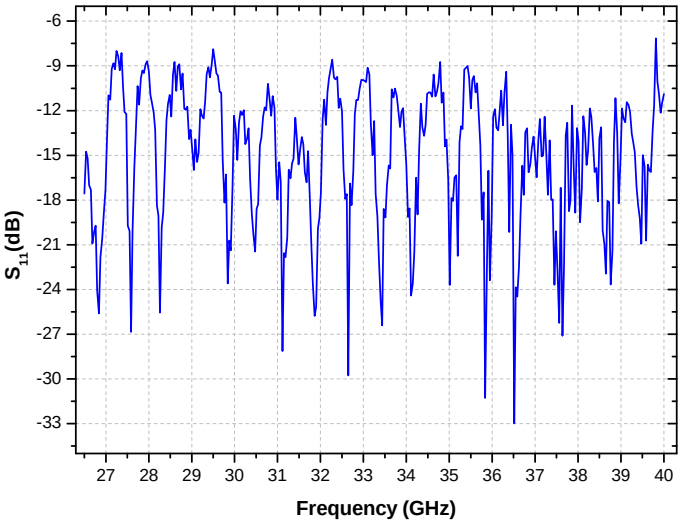


Figure 72: Reflection coefficient S11 of the modified setup measured with the presence of the sample.

After optimizing the experimental conditions, the polarization study has been repeated. Since the new antenna support can only move manually, it is difficult to determine an exact value of the polarization angle and thus this could reduce the measurement accuracy. Therefore, the angle has been varied from -40° to +40°, taking a step of 10° with an estimation error of 5° for each angle. The generated voltage, presented in Figure 73, shows a similar response to the polarization angle change, compared to the previous test performed. At f = 30.5 GHz and a power of 20 dBm, a maximum voltage is produced when the antenna is at the center, angle = 0°, and this value is reduced while moving away from the center.

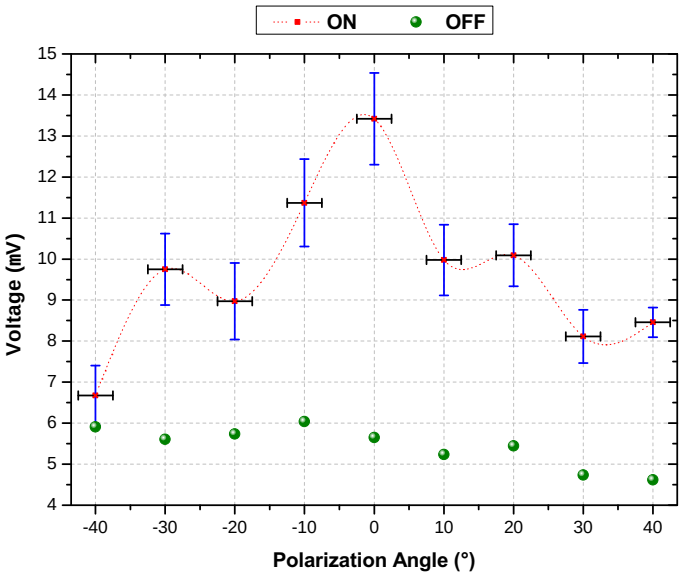


Figure 73: Voltage variation with respect to the polarization angle. The horn antenna is at distance of 6 cm from the sample, the applied power is 20 dBm, the frequency is 30.5 GHz and the attenuation of the cable used is about 7 dB.

5.5.6.3 Voltage Vs Frequency

Using the optimized setup, the relation between the voltage and the frequency has been also analyzed. In this frequency study, the polarization angle and the applied power have been fixed to 0° and 20 dBm respectively. Two bands of frequencies have been investigated: frequency band from 30 to 35 GHz and the band from 1 to 12 GHz.

A) Frequency band 30 GHz to 35 GHz

For the band of frequency from 30 to 35 GHz, the voltage has been measured, taking 20 points of measurements for each frequency and calculating their average. When the antenna is at a distance of 6 cm, this measurement has been repeated three times to verify the reproducibility of the observed phenomenon. As presented in Figure 74, the voltage decreases while increasing the frequency. The voltage values, shown in the figure, represent the difference between the values obtained when the RF generator is turned on and their values when it is turned off.

B) Frequency band 1 GHz to 12 GHz

The variation of the generated voltage with respect to the frequency has been also tested for the frequency band from 1 to 12 GHz. Another horn antenna has been used that

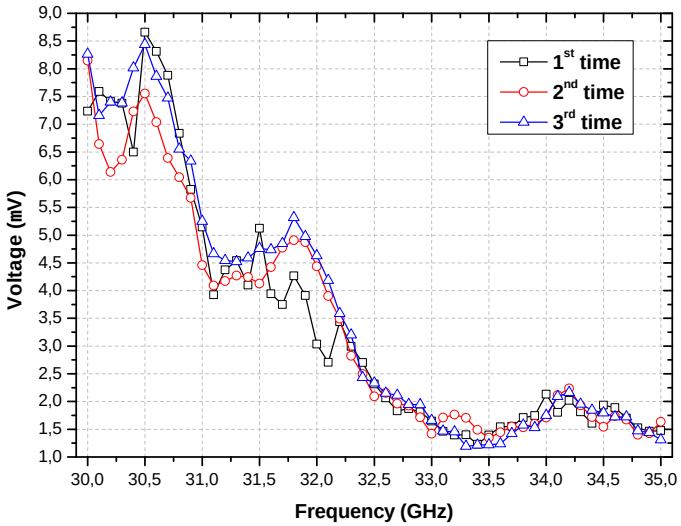


Figure 74: Voltage variation with respect to the frequency when the antenna is at 6 cm from the sample. This measurement has been repeated three times, taking the average of 20 points of measurements for each frequency.

operates in this band of frequency with an average gain of 8-12 dBi. Figure 75 shows the image of the setup used.

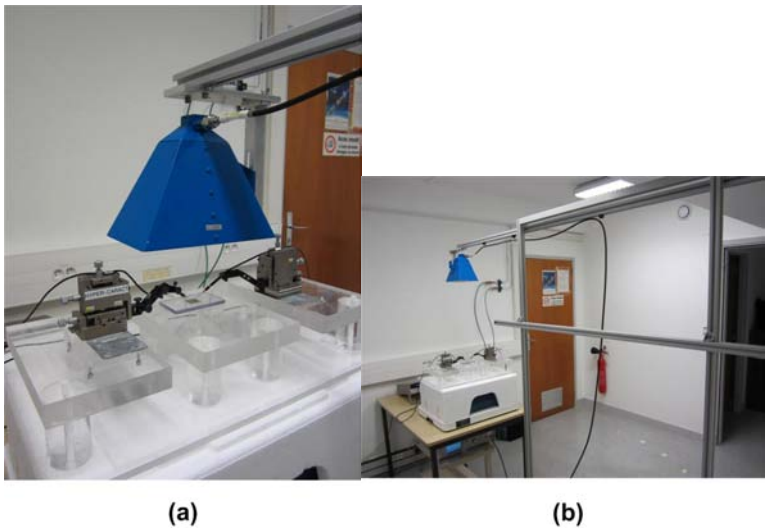


Figure 75: Photo of the horn antenna (1-12 GHz) when it is at a distance of: (a) 11 cm and (b) 60 cm from the sample.

Before performing the frequency study, the reflection coefficient S11 of the setup has been measured when the horn antenna is at a distance of about 11 cm and 60 cm from the sample, as shown in Figure 76. The reflection coefficient is around -15 dB for the two distances.
Afterwards, the sample response to the frequency band from 1 to 12 GHz has been studied. When the antenna is at a distance of 11 cm from the sample, it has been observed that the voltage obtained is in the mV range and it decreases with increasing the frequency

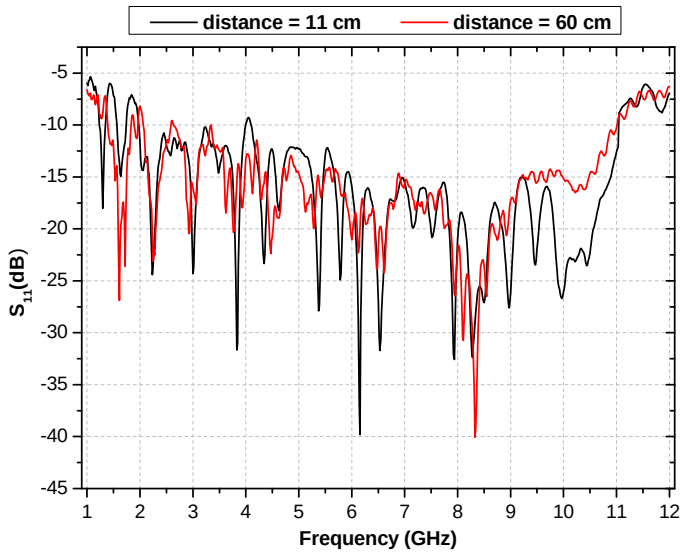


Figure 76: Reflection coefficient S11 of the setup measured when the horn antenna (1-12 GHz) is at a distance of 11 cm and 60 cm from the sample.

as observed before for the frequency band from 30 to 35 GHz. This measurement has been repeated two times taking 20 points of measurements for each frequency and calculating their average, as presented in Figure 77.

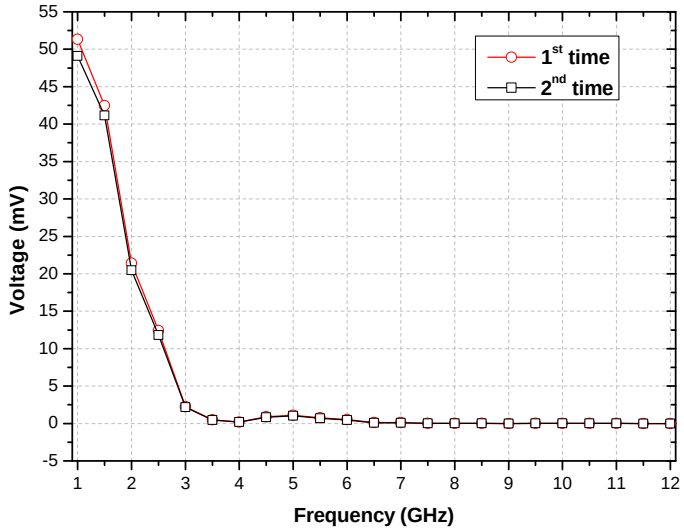


Figure 77: Voltage variation with respect to the frequency when the antenna is at 11 cm from the sample. This measurement has been repeated three times, taking the average of 20 points of measurements for each frequency.

In Figure 78, the voltage ranges with respect to the frequency are presented in details, where we compare the voltage values when the RF generator is switched ON and OFF. In general, the graphs show a decrease of the voltage with the increase of frequency. But for Figure 78(b), a peak voltage has been noticed at f = 5 GHz and in Figure 78(c) there are some fluctuations of the voltage for the frequencies from 9 to 11.5 GHz.

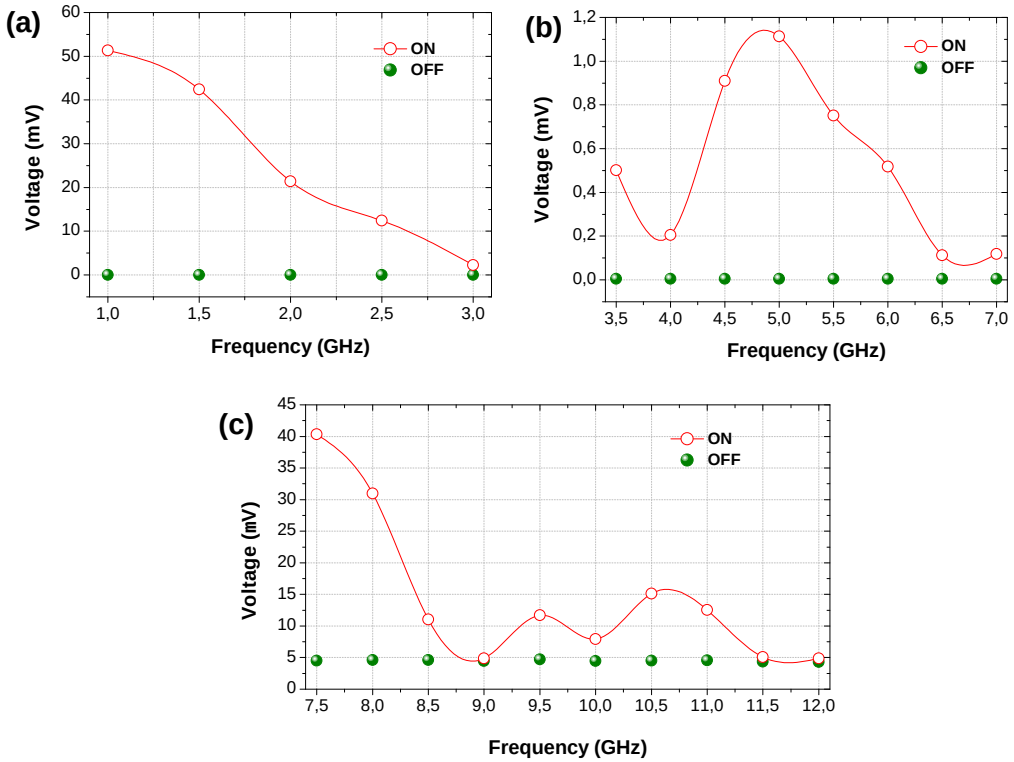


Figure 78: Voltage ranges with respect to the frequency: (a) f = 1 to 3 GHz, (b) f = 3.5 to 7 GHz and (c) 7.5 to 12 GHz.

The previous measurement has been also performed when the antenna is at a distance of about 60 cm from the sample. Figure 79 shows that the voltages values obtained are reduced compared to the previous results of Figure 77. It shows also the decrease of the voltage with the increase of the frequency, except for a peak value at a frequency between 2 and 2.5 GHz, as shown in details in Figure 80(a). Similar to the previous measurement, Figure 80(b) illustrates a peak voltage at a frequency between 4.5 and 5 GHz and in Figure 80(c) we can observe the voltage fluctuations for the frequencies from 8.5 to 10.5 GHz.

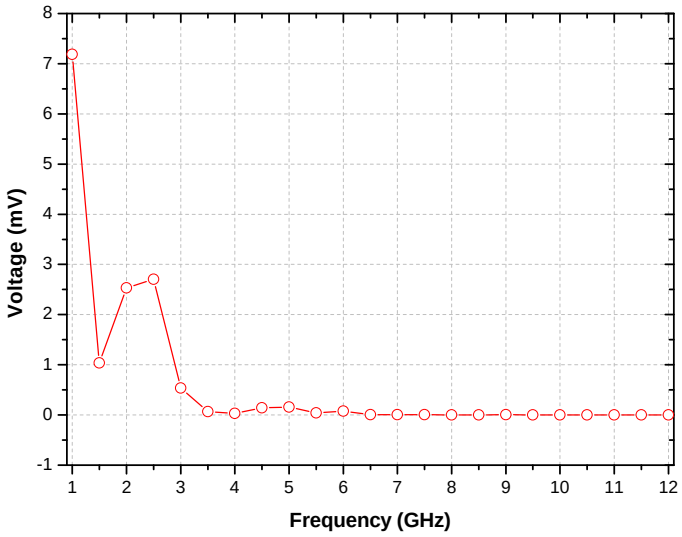


Figure 79: Voltage variation with respect to the frequency when the antenna is at 60 cm from the sample, taking the average of 20 points of measurements for each frequency.

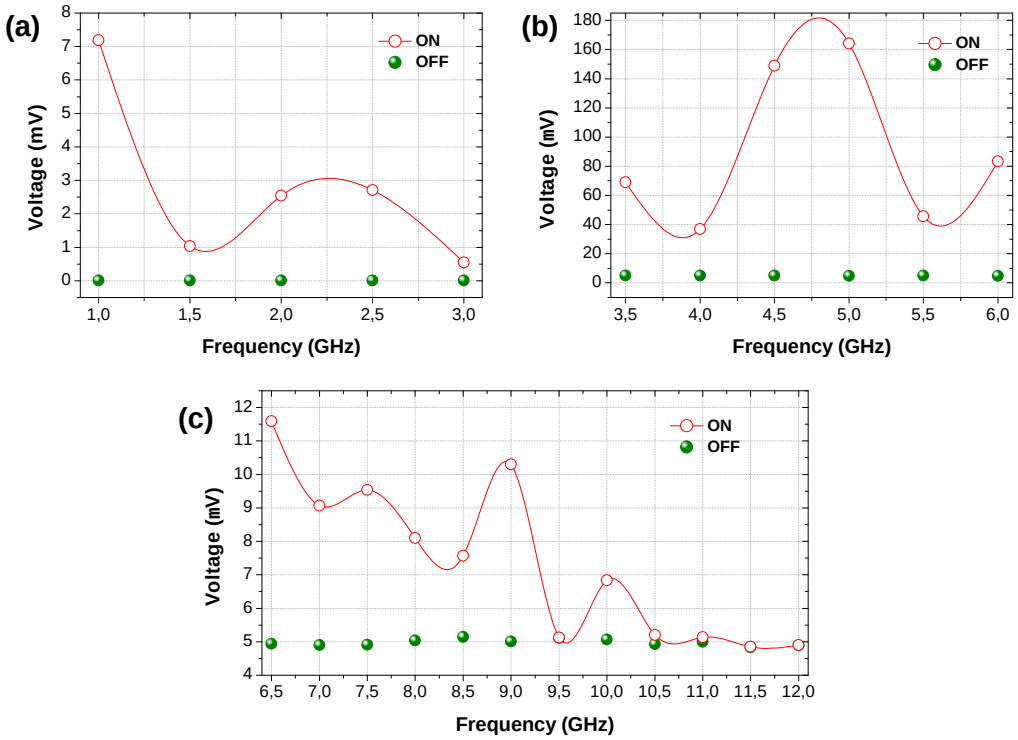


Figure 80: Voltage ranges with respect to the frequency: (a) f = 1 to 3 GHz, (b) f = 3.5 to 6 GHz and (c) 6.5 to 12 GHz.

5.6 CONCLUSION

This chapter revealed the production of a DC voltage from a bilayer graphene flake with asymmetric shaped antidots, under microwave energy at room temperature. Since graphene is a delicate material, it is hard to manipulate the process of contacts fabrication and antidots patterning of the Ratchet Device. Working at room temperature has enabled us to use a simple experimental setup that we could easily control and optimize and hence we can minimize the negative impact of the setup on the experimental results obtained.
According to the experimental and the statistical analysis, we could demonstrate the repeatability and reproducibility of the observed phenomenon under unchanged conditions. The dependence of the produced voltage on the polarization angle and the frequency was presented. The studied sample shows a symmetrical response around the angle zero: the voltage is maximum at angle = 0° (the curve center) while it decays on both side of the curve until it vanishes at angle = ±90°. Therefore, the maximum voltage is obtained when the electric field is parallel to x-axis but it vanishes when the applied electric field becomes parallel to y-axis. On the other hand, for the two tested frequency bands: 1-12 GHz and 30-35 GHz, it has been noticed that the induced voltage decreases while increasing the frequency. For the frequency band from 1 to 12 GHz, a voltage could be obtained in the mV range. This last observation implies the need of performing further and detailed experimental tests in order to study the Ratchet Device response to GSM frequency bands that could open new perspectives in the telecommunication domain. Moreover, amplitutude modulation tests have to be applied on the Ratchet Device based on graphene to verify if it could demodulate the received modulated signals. All these experimental tests have to be repeated on a virgin graphene sample without antidots to compare its response to the Ratchet Device.

GENERAL CONCLUSION AND PERSPECTIVES

This general conclusion briefly summarizes the most important contributions of this thesis and the perspectives on future work. This thesis has been devoted to the study of the Ratchet Device and the used experimental setup from the electromagnetic point of view following a certain methodology. This methodology can be applied to any studied phenomenon, in which there is a challenge between the physical and the electromagnetic experiment conditions. The Ratchet Device based on semiconductor heterojunctions (AlGaAs/GaAs and Si/SiGe) can only operate at low temperature which implies the use of a complex experimental setup with a cryogenic closed metallic system. An important step is to find the descriptors that define the Ratchet phenomenon in a simple manner. These descriptors are: the normalized electromagnetic power flow across the studied sample surface (P_n), the uniformity of the electric field linear polarization on the sample surface (K_E), the uniformity of the incident power density on the sample surface (K_P), the distribution of the y-component of the electric field inside the metallic cavity of the cryogenic system (E_y) and the uniformity of the y-component of the electric field density on the sample surface (K_D). These descriptors represent a helpful tool in judging on the electromagnetic behavior of the setup that could have a considerable impact on the experimental results and prevents us of having a clear image of the Ratchet Device response.

One of the proposed applications of the Ratchet Device is the possibilty of fabricating a simple amplitude demodulator at the nanoscale level. As a result, some preliminary amplitude modulation tests have been performed to investigate the response of the Ratchet Device based on semiconductor heterojunctions. Also, the device response has been compared to the response of a virgin unpatterned semiconductor heterojunction. It has been found that the Ratchet Device seems to have the ability of demodulating a received modulated signal. However, the virgin sample shows also a response to the modulation test but it is not appropriate compared to the Ratchet Device response. This observation forces us to implement further measurements tests and to apply other types of modulation techniques in order to determine the device operation modes and its possible limitations.

On the other hand, we report first time measurements on Ratchet Device based on graphene that has been introduced, in chapter 5, as an alternative to the current Ratchet Devices based on AlGaAs/GaAs and Si/SiGe heterojunctions that work at low temperature. It represents a possible solution to the drawbacks of the current Ratchet Devices as it works at room temperature and thus a simple experimental setup could be used. A rigorous experimental investigation has been performed at room temperature in order to check the Ratched Device capabilities to work as a DC voltage generator or an electric field polarization detector under microwave radiation. In CNRS-LAAS, a simple new setup has been used in order to perform our experiments. This new setup has been developed in a manner that would minimize any negative effects of the setup on the experimental results.

The voltage variation with respect to the electric field polarization and the applied operating frequency has been studied. It has been noticed that a maximum voltage could be obtained when the electric field is parallel to the x-axis (parallel to the sample horizontal contacts). As it has been revealed in chapter 5, this Ratchet Device generates a relatively high voltage in the frequency band from 1 GHz to 12 GHz and a moderate

voltage in the band from 30 GHz to 35 GHz. Therefore, more measurements have to be done on several graphene Ratchet Devices to determine the frequency bands where these devices could operate appropriately. In addition, the device response to the variation of the RF power must be tested in order to have a complete characterization of the device. Furthermore, its ability of demodulating a received modulated signal has to be examined to compare it with the heterojunction Ratchet Device. Besides, the Ratchet Device response to the applied modualtion tests could also be investigated from the theoretical point of view using the numerical approach developed by L. Ermann and D.L. Shepelyansky (presented in section 5.2) in order to check the degree of agreement between theory and experiment.
All these experimental measurements have to be repeated on a virgin graphene sample (unfortunately, our virgin sample was broken during the manufacturing process). This allows doing a comparative analysis necessary to evaluate the frame and the properties of the Ratchet Device based on graphene.
It is important to bear in mind that this set of device tests performance represents the first and the most important step that has to be realized in order to provide a well characterized Ratchet Device that could make a significant leap forward in the wireless telecommunications domain.

[1] R.P. Feynman. *Feynman Lectures on Physics, Vol. 1*. Addison Wesley, 1963.

[2] H. Linke, B. J. Alemán, L. D. Melling, M. J. Taormina, M. J. Francis, C. C. Dow-Hygelund, V. Narayanan, R. P. Taylor, and A. Stout. Self-propelled leidenfrost droplets. *Phys. Rev. Lett.*, 96:154502, Apr. 2006.

[3] R. Ait-Haddou and W. Herzog. Brownian ratchet models of molecular motors. *Cell Biochemistry and Biophysics*, 38:191–213, 2003.

[4] A.M. Song. Electron ratchet effect in semiconductor devices and artificial materials with broken centrosymmetry. *Applied Physics A: Materials Science & Processing*, 75:229–235, 2002.

[5] S. Sassine. *Transport électronique contrôlé par micro-ondes dans des microstructures asymétriques : Effet ratchet mésoscopique*. PhD thesis, Université de Toulouse, 2007.

[6] S. Sassine, Yu. Krupko, J.-C. Portal, Z. D. Kvon, R. Murali, K. P. Martin, G. Hill, and A. D. Wieck. Experimental investigation of the ratchet effect in a two-dimensional electron system with broken spatial inversion symmetry. *Phys. Rev. B*, 78:045431, Jul. 2008.

[7] S. Sassine, Yu. Krupko, Z.D. Kvon, J.-C. Portal, R. Murali, K.P. Martin, G. Hill, and A.D. Wieck. Polarized-microwave control of directed transport in a 2D electron gas with artificial asymmetrical scatterers. *Physica E: Low-dimensional Systems and Nanostructures*, 40(6):2043 – 2045, 2008.

[8] S. Sassine, Yu. Krupko, E.B. Olshanetsky, Z.D. Kvon, J.C. Portal, J.M. Hartmann, and J. Zhang. Microwave radiation induced collective response in Si/SiGe heterostructures with a 2D electron gas. *Solid State Communications*, 142(11):631 – 633, 2007.

[9] I. Bisotto, E. S. Kannan, S. Sassine, R. Murali, T. J. Beck, L. Jalabert, and J.-C. Portal. Microwave based nanogenerator using the ratchet effect in Si/SiGe heterostructures. *Nanotechnology journal*, 22(24):245401, 2011.

[10] E. S. Kannan, I. Bisotto, J.-C. Portal, R. Murali, and T. J. Beck. Photovoltage induced by ratchet effect in Si/SiGe heterostructures under microwave irradiation. *Appl. Phys. Lett.*, 98(19):193505, 2011.

[11] A. D. Chepelianskii and D. L. Shepelyansky. Directing transport by polarized radiation in the presence of chaos and dissipation. *Phys. Rev. B*, 71:052508, Feb. 2005.

[12] A. D. Chepelianskii. Microwave control of directed transport in asymmetric antidot structures. *The European Physical Journal B - Condensed Matter and Complex Systems*, 52:389–396, 2006.

[13] A. D. Chepelianskii, M. V. Entin, L. I. Magarill, and D. L. Shepelyansky. Photogalvanic current in artificial asymmetric nanostructures. *The European Physical Journal B - Condensed Matter and Complex Systems*, 56:323–333, 2007.

[14] A. D. Chepelianskii, M. V. Entin, L. I. Magarill, and D. L. Shepelyansky. Ratchet transport of interacting particles. *Phys. Rev. E*, 78:041127, Oct. 2008.

[15] W. Weber, L. E. Golub, S. N. Danilov, J. Karch, C. Reitmaier, B. Wittmann, V. V. Bel'kov, E. L. Ivchenko, Z. D. Kvon, N. Q. Vinh, A. F. G. van der Meer, B. Murdin, and S. D. Ganichev. Quantum ratchet effects induced by terahertz radiation in GaN-based two-dimensional structures. *Phys. Rev. B*, 77:245304, Jun. 2008.

[16] P. Olbrich, E. L. Ivchenko, R. Ravash, T. Feil, S. D. Danilov, J. Allerdings, D. Weiss, D. Schuh, W. Wegscheider, and S. D. Ganichev. Ratchet effects induced by terahertz radiation in heterostructures with a lateral periodic potential. *Phys. Rev. Lett.*, 103:090603, Aug. 2009.

[17] G. Dresselhaus, A. F. Kip, and C. Kittel. Observation of cyclotron resonance in germanium crystals. *Phys. Rev.*, 92:827–827, Nov. 1953.

[18] A. D. Chepelianskii and D. L. Shepelyansky. Microwave stabilization of edge transport and zero-resistance states. *Phys. Rev. B*, 80:241308, Dec. 2009.

[19] P. Reimann. Brownian motors: noisy transport far from equilibrium. *Physics Reports*, 361(2-4):57 – 265, 2002.

[20] C. Drexler, V. V. Bel'kov, B. Ashkinadze, P. Olbrich, C. Zoth, V. Lechner, Ya. V. Terent'ev, D. R. Yakovlev, G. Karczewski, T. Wojtowicz, D. Schuh, W. Wegscheider, and S. D. Ganichev. Spin polarized electric currents in semiconductor heterostructures induced by microwave radiation. *Appl. Phys. Lett.*, 97(18):182107, 2010.

[21] M. I. Dyakonov. *Spin Physics in Semiconductors*. Springer, 2008.

[22] Emerson & Cuming. http://www.eccosorb.com.

[23] Ansoft HFSS. http://www.ansoft.com.

[24] A. Takacs, D. Medhat, H. Aubert, and J.C. Portal. Electromagnetic analysis of the experimental setup used to investigate the ratchet effect in two-dimensional electron system under microwave radiation. In *Semiconductor Conference, 2009. CAS 2009. International*, volume 1, pages 337 –340, Oct. 2009.

[25] A. Takacs, D. Medhat, H. Aubert, and J.-C. Portal. A method for estimating the electromagnetic power delivered by the front-end module used to investigate the ratchet effect in two-dimensional electron gas system under microwave radiation. In *Microwave Conference (EuMC), 2010 European*, pages 1560 –1563, Sept. 2010.

[26] A-INFO. http://www.ainfoinc.com.

[27] Anritsu. http://www.anritsu.com.

[28] D. Medhat, A. Takacs, H. Aubert, and J.C. Portal. Comparative analysis of different techniques for controlling ratchet effect in a periodic array of asymmetric antidots. In *Microwave Conference, 2009. APMC 2009. Asia Pacific*, pages 1711 –1714, Dec. 2009.

[29] B. Fuchs, O. Lafond, S. Rondineau, and M. Himdi. Design and characterization of half maxwell fish-eye lens antennas in millimeter waves. *IEEE Transactions on Microwave Theory and Techniques*, 54(6):2292 –2300, Jun. 2006.

[30] B. Fuchs, O. Lafond, S. Palud, L. Le Coq, M. Himdi, M.C. Buck, and S. Rondineau. Comparative design and analysis of luneburg and half maxwell fish-eye lens antennas. *IEEE Transactions on Antennas and Propagation*, 56(9):3058 –3062, Sept. 2008.

[31] J. Qiu, S. Lin, and S. Gu. The comparison between luneburg lens and single medium spherical lens. In *Antennas and Propagation Society International Symposium 2006, IEEE*, pages 3365 –3368, Jul. 2006.

[32] R.K. Luneburg. *Mathematical theory of optics*. Mathematical Theory of Optics. Brown University, 1944.

[33] A. Ali and H. Aubert. Fractal superlattice cover with variable lacunarity for patch antenna directivity enhancement analysis and design. *WTOC*, 7(10):1035–1044, Oct. 2008.

[34] Constantine A. Balanis. *Antenna Theory: Analysis and Design*. Wiley, 3 edition, April 2005.

[35] Antenna Magus. http://www.antennamagus.com.

[36] D. Medhat, A. Takacs, and H. Aubert. A methodology to study the electromagnetic behavior of a cryogenic metallic system used to control the ratchet effect. *Progress In Electromagnetics Research M*, 23(18):123 –137, 2012.

[37] David M. Pozar. *Microwave Engineering*. Wiley, 3 edition, February 2004.

[38] D. Medhat, A. Takacs, and H. Aubert. Optimum position of the two-dimensional electron gas sample in the cryogenic metallic cavity system used in studying ratchet effect. In *Microwave Conference (EuMC), 2011 41st European*, pages 964 –967, Oct. 2011.

[39] H.S. Black. *Modulation theory*. Bell Telephone Laboratories series. Van Nostrand, 1953.

[40] G. Smillie. *Analogue and Digital Communication Techniques*. Arnold, 1999.

[41] R.T. Hitchcock and R.M. Patterson. *Radio-Frequency and Elf Electromagnetic Energies: A Handbook for Health Professionals*. Industrial Health and Safety Series. John Wiley & Sons, 1995.

[42] NI LabVIEW. http://www.ni.com/labview/.

[43] A.P.G.U.A. Bakshi. *Communication Engineering*. Technical Publications, 2009.

[44] E.A. Lee and S.A. Seshia. *Introduction to Embedded Systems: A Cyber-Physical Systems Approach*. Electrical Engineering & Computer Sciences. Lulu.com, 2011.

[45] F.M. Mims. *Mims Circuit Scrapbook*. The Forrest Mims Circuit Scrapbook. Elsevier Science, 2000.

[46] A. H. Castro Neto, F. Guinea, N. M. R. Peres, K. S. Novoselov, and A. K. Geim. The electronic properties of graphene. *Rev. Mod. Phys.*, 81:109–162, Jan. 2009.

[47] C. Stampfer, S. Fringes, J. Güttinger, F. Molitor, C. Volk, B. Terrés, J. Dauber, S. Engels, S. Schnez, A. Jacobsen, S. Dröscher, T. Ihn, and K. Ensslin. Transport in graphene nanostructures. *Frontiers of Physics*, 6:271–293, 2011.

[48] K. S. Novoselov, A. K. Geim, S. V. Morozov, D. Jiang, Y. Zhang, S. V. Dubonos, I. V. Grigorieva, and A. A. Firsov. Electric field effect in atomically thin carbon films. *Science*, 306(5696):666–669, 2004.

[49] K. Nagashio, T. Nishimura, K. Kita, and A. Toriumi. Mobility variations in mono- and multi-layer graphene films. *Applied Physics Express*, 2(2):025003, 2009.

[50] K.I. Bolotin, K.J. Sikes, Z. Jiang, M. Klima, G. Fudenberg, J. Hone, P. Kim, and H.L. Stormer. Ultrahigh electron mobility in suspended graphene. *Solid State Communications*, 146(9-10):351 – 355, 2008.

[51] A. V. Nalitov, L. E. Golub, and E. L. Ivchenko. Ratchet effects in graphene with a lateral periodic potential. *Phys. Rev. B*, 2012.

[52] J. Karch, C. Drexler, P. Olbrich, M. Fehrenbacher, M. Hirmer, M. M. Glazov, S. A. Tarasenko, E. L. Ivchenko, B. Birkner, J. Eroms, D. Weiss, R. Yakimova, S. Lara-Avila, S. Kubatkin, M. Ostler, T. Seyller, and S. D. Ganichev. Terahertz radiation driven chiral edge currents in graphene. *Phys. Rev. Lett.*, 107:276601, Dec. 2011.

[53] J. Karch, P. Olbrich, M. Schmalzbauer, C. Zoth, C. Brinsteiner, M. Fehrenbacher, U. Wurstbauer, M. M. Glazov, S. A. Tarasenko, E. L. Ivchenko, D. Weiss, J. Eroms, R. Yakimova, S. Lara-Avila, S. Kubatkin, and S. D. Ganichev. Dynamic hall effect driven by circularly polarized light in a graphene layer. *Phys. Rev. Lett.*, 105:227402, Nov. 2010.

[54] P. San-Jose, E. Prada, S. Kohler, and H. Schomerus. Single-parameter pumping in graphene. *Phys. Rev. B*, 84:155408, Oct. 2011.

[55] L. Ermann and D. L. Shepelyansky. Relativistic graphene ratchet on semidisk galton board. *The European Physical Journal B - Condensed Matter and Complex Systems*, 79:357–362, 2011.

[56] A. C. Ferrari, J. C. Meyer, V. Scardaci, C. Casiraghi, M. Lazzeri, F. Mauri, S. Piscanec, D. Jiang, K. S. Novoselov, S. Roth, and A. K. Geim. Raman spectrum of graphene and graphene layers. *Phys. Rev. Lett.*, 97:187401, Oct. 2006.

[57] G. Binnig, C. F. Quate, and Ch. Gerber. Atomic force microscope. *Phys. Rev. Lett.*, 56:930–933, Mar. 1986.

[58] K. Nagashio, T. Nishimura, K. Kita, and A. Toriumi. Metal/graphene contact as a performance killer of ultra-high mobility graphene analysis of intrinsic mobility and contact resistance. In *Electron Devices Meeting (IEDM), 2009 IEEE International*, pages 1 –4, Dec. 2009.

[59] H. Czichos, T. Saito, and L. Smith. *Springer Handbook of Materials Measurement Methods*. Springer handbooks. Springer, 2006.

[60] M. Nonnenmacher, M. P. O'Boyle, and H. K. Wickramasinghe. Kelvin probe force microscopy. *Applied Physics Letters*, 58(25):2921–2923, 1991.

[61] M. Abramowitz and I.A. Stegun. *Handbook of Mathematical Functions: With Formulas, Graphs, and Mathematical Tables*. Applied mathematics series. Dover Publications, 1964.

[62] Constantine A. Balanis. *Advanced engineering electromagnetics*. Wiley-India.

PUBLICATIONS

JOURNAL PAPER

- D. Medhat, A. Takacs, and H. Aubert. A methodology to study the electromagnetic behavior of a cryogenic metallic system used to control the ratchet effect. *Progress In Electromagnetics Research M*, 23(18): 123–137, 2012.

INTERNATIONAL CONFERENCE PAPERS

- D. Medhat, A. Takacs, and H. Aubert. Optimum position of the two-dimensional electron gas sample in the cryogenic metallic cavity system used in studying ratchet effect. *In Microwave Conference (EuMC), 2011 41st European*, pages 964–967, Oct. 2011.
- D. Medhat, A. Takacs, H. Aubert, and J.-C. Portal. Investigation of the metallic cavity influence on the electromagnetic behavior of the setup used in studying the ratchet effect. *Progress In Electromagnetics Research Symposium Abstracts*, 452-453, Mar. 2011.
- Takacs, D. Medhat, H. Aubert, and J.-C. Portal. A method for estimating the electromagnetic power delivered by the front-end module used to investigate the ratchet effect in two-dimensional electron gas system under microwave radiation. *In Microwave Conference (EuMC)*, 2010 European, pages 1560–1563, Sept. 2010.
- D. Medhat, A. Takacs, H. Aubert, and J.C. Portal. Comparative analysis of different techniques for controlling ratchet effect in a periodic array of asymmetric antidots. *In Microwave Conference, 2009. APMC 2009. Asia Pacific*, pages 1711–1714, Dec. 2009.
- Takacs, D. Medhat, H. Aubert, and J.C. Portal. Electromagnetic analysis of the experimental setup used to investigate the ratchet effect in two-dimensional electron system under microwave radiation. *In Semiconductor Conference, 2009. CAS 2009*. International, volume 1, pages 337–340, Oct. 2009.

NATIONAL CONFERENCE PAPER

- D. Medhat. Analyse électromagnétique du dispositif expérimental utilisé dans l'étude de l'Effet Ratchet dans un réseau d'antipoints asymétriques. *Journée de l'école doctorale GEET*, Avr. 2012.

APPENDIX

A

CALCULATION OF THE NUMBER OF PROPAGATING MODES IN A CIRCULAR WAVEGUIDE USING A MATLAB CODE

A simple Matlab code has been developed in order to calculate the number of modes propagating in a circular waveguide.
The number of modes depends on the operating frequency f and the waveguide inner radius a. In this example, the values of **f** and **a** are 50 GHz and 14.205 mm respectively. This frequency has been used in performing the Ratchet experiments and the radius value corresponds to the inner radius of the metallic cavity of the cryogenic system (see section 3.3). Taking as physical constants, the permeability **uo**, the permittivity **eo** and the velocity of light in free space **c**.

```
% Initial values

f=50*1e9;
uo=4*pi*1e-7;
eo=8.854*1e-12;
c=1/sqrt(uo*eo);

a=14.205*1e-3;
```

Concerning the TM modes, we have to compute first the zeros of the Bessel function of the first kind J(n,x) for various integer orders n. The roots of the Bessel function **P_TM** could be determined using the matlab function **fzero(fun,v)**. This matlab function tries to find the roots of a chosen function **fun** near the scalar value **v**.
These roots could be presented in a matrix form P_TM[n,m], as shown in Table A, with n the number of rows and m the number of columns. The first zero of J(0,x), which is P_TM[0,1], has a value near the scalar value 2. Therefore, we can say that the first column of the Bessel function roots P_TM[n,1], lies in the interval between 2 and **h_TM**. In order to determine **h_TM**, a computable formula presented in equation A.1 has been used. This formula is obtained from the asymptotic formula given by Abramowitz and Stegun [61]

$$h_TM = n + 1.9 \times n\hat{} (1/3) + 1 \tag{A.1}$$

In order to complete the rest of Table A, it has been noticed that the scalar value near each element of the second column P_TM[n,2] could be determined by adding the number 4 to the values of the first column. In general,

$$Scalar\,value\,near\ P_TM\,[n, m] = P_TM\,[n-1, m-1] + 4 \tag{A.2}$$

Then, this scalar value is used in the fzero Matlab function to compute the roots presented in Table 2.
Concerning the TE modes, we have to compute **P_TE** that represents the zeros of the Bessel function derivatives J'(n,x) for various integer orders n. According to Table B, the first zero of J'(0,x) has a value a value near the scalar value 3. The first column of the Bessel function derivatives roots lies in the interval between 3 and **h_TE**. In this case, **h_TE** is calculated using equation A.3

n\m	m = 1	m = 2	m = 3	m = 4	m = 5
n = 0	2.4048	5.5201	8.6537	11.7915	14.9309
n = 1	3.8317	7.0156	10.1735	13.3237	16.4706
n = 2	5.1356	8.4172	11.6198	14.7960	17.9598
n = 3	6.3802	9.7610	13.0152	16.2235	19.4094
n = 4	7.5883	11.0647	14.3725	17.6160	20.8269
n = 5	8.7715	12.3386	15.7002	18.9801	22.2178
n = 6	9.9361	13.5893	17.0038	20.3208	23.5861
n = 7	11.0864	14.8213	18.2876	21.6415	24.9349
n = 8	12.2251	16.0378	19.5545	22.9452	26.2668
n = 9	13.3543	17.2412	20.8070	24.2339	27.5837
n = 10	14.4755	18.4335	22.0470	25.5095	28.8874

Table 2: Roots of Bessel function, **P_TM**.

$$h_TE = n + 1 \tag{A.3}$$

The rest of Table 3 is completed by also incrementing the values of each column by the number 4 to define the interval of the next column.

n\m	m = 1	m = 2	m = 3	m = 4	m = 5
n = 0	3.8317	7.0156	10.1735	13.3237	16.4706
n = 1	1.8412	5.3314	8.5363	11.7060	14.8636
n = 2	3.0542	6.7061	9.9695	13.1704	16.3475
n = 3	4.2012	8.0152	11.3459	14.5858	17.7887
n = 4	5.3176	9.2824	12.6819	15.9641	19.1960
n = 5	6.4156	10.5199	13.9872	17.3128	20.5755
n = 6	7.5013	11.7349	15.2682	18.6374	21.9317
n = 7	8.5778	12.9324	16.5294	19.9419	23.2681
n = 8	9.6474	14.1155	17.7740	21.2291	24.5872
n = 9	10.7114	15.2867	19.0046	22.5014	25.8913
n = 10	11.7709	16.4479	20.2230	23.7607	27.1820

Table 3: Roots of Bessel function Derivatives, **P_TE**.

```
% TM_roots & TE_roots

incr=4;
k=1;
for n=0:10
   h_TM=n+1.9.*n.^(1/3)+1;
   h_TE=n+1;
   if n==0
      P_TM=fzero(@(x)besselj(n,x),2);
      P_TE=fzero(@(x) -besselj(n+1,x),3);
   else
      P_TM=fzero(@(x)besselj(n,x),h_TM);
      P_TE=fzero(@(x) besselj(n-1,x)-(n.*besselj(n,x)./x),h_TE);
   end
   vect_TM(k)=P_TM;
   vect_TE(k)=P_TE;
   k=k+1;
   for m=2:5
      P_TM=fzero(@(x)besselj(n,x),P_TM+incr);
      P_TE=fzero(@(x) besselj(n-1,x)-(n.*besselj(n,x)./x),P_TE+incr);
   vect_TM(k)=P_TM;
   vect_TE(k)=P_TE;
   k=k+1;
   end
end
P_TM = vec2mat(vect_TM,5);
P_TE = vec2mat(vect_TE,5) ;
```

After creating the two tables presented above, the cut-off frequency of each TM and TE mode could be calculated using equations A.4 and A.5 given by [37]

$$fc_TM = \frac{P_TM}{2\pi a\sqrt{\mu\varepsilon}} \tag{A.4}$$

$$fc_TE = \frac{P_TE}{2\pi a\sqrt{\mu\varepsilon}} \tag{A.5}$$

```
% Cut-off frequency of TM & TE modes

fc_TM=(P_TM.*c)./(2.*pi.*a);
fc_TE=(P_TE.*c)./(2.*pi.*a);
```

As a result, a matrix of **fc_TM** and **fc_TE** is obtained, as presented below.

```
fc_TM =

1.0e+010 *

0.8078   1.8542   2.9067   3.9607   5.0152
1.2871   2.3565   3.4172   4.4754   5.5324
1.7250   2.8273   3.9031   4.9699   6.0326
2.1431   3.2787   4.3717   5.4494   6.5195
2.5489   3.7166   4.8277   5.9171   6.9957
2.9463   4.1445   5.2736   6.3753   7.4629
3.3375   4.5646   5.7115   6.8257   7.9225
3.7239   4.9784   6.1427   7.2693   8.3755
4.1064   5.3870   6.5683   7.7072   8.8229
4.4856   5.7912   6.9890   8.1401   9.2653
4.8623   6.1917   7.4055   8.5685   9.7031

fc_TE =

1.0e+010 *

1.2871   2.3565   3.4172   4.4754   5.5324
0.6184   1.7908   2.8673   3.9320   4.9926
1.0259   2.2526   3.3487   4.4239   5.4911
1.4112   2.6923   3.8110   4.8993   5.9752
1.7861   3.1179   4.2598   5.3623   6.4479
2.1550   3.5336   4.6982   5.8153   6.9112
2.5196   3.9417   5.1285   6.2602   7.3668
2.8813   4.3439   5.5521   6.6984   7.8156
3.2405   4.7413   5.9702   7.1307   8.2587
3.5979   5.1347   6.3836   7.5581   8.6968
3.9538   5.5248   6.7928   7.9811   9.1303
```

In order to determine the number of TM modes, **N_TM_modes**, and the number of TE modes, **N_TE_modes**, that could propagate in the circular waveguide, each element of the **fc_TM** matrix and the **fc_TE** matrix has to be compared to the operating frequency of 50 GHz. A propagating mode must have a cut-off frequency smaller than the value of the operating frequency.

```
% Number of TM modes

dim=nnz(fc_TM);
N_TM_modes=0;
[rows_TM cols_TM] = size(fc_TM);
for i = 1:rows_TM
   for j = 1:cols_TM
      t = fc_TM(i, j);
      if t < f
            N_TM_modes=N_TM_modes+1;
      end
   end
end
N_TM_modes

% Number of TE modes

dim=nnz(fc_TE);
N_TE_modes=0;
[rows_TE cols_TE] = size(fc_TE);
for u = 1:rows_TE
   for v = 1:cols_TE
      s = fc_TE(u, v);
      if s < f
            N_TE_modes=N_TE_modes+1;
      end
   end
end
N_TE_modes
%%%
```

B

EFFECT OF THE SUBSTRATE THICKNESS ON THE INCIDENT ELECTRIC FIELD

Based on the analytical equations presented in [62], the reflection of the electric field on the dielectric interfaces could be calculated. This approach has been used to study the effect of a silicon substrate thickness on the electric field under normal incidence. Figure 81 illustrates a schematic of the three dielectric regions: dielectric 1 and dielectric 3 represent the free space surrounding the substrate with intrinsic impedances **n1** and **n3** respectively which are equal to the intrinsic impedance of free space **n0**. Dielectric 2 represents the silicon substrate with a relative permittivity **er_si** of 11.7. As an example, we have taken a silicon substrate with a thickness **d** of 300 µm and an operating frequency **f** of 50 GHz.

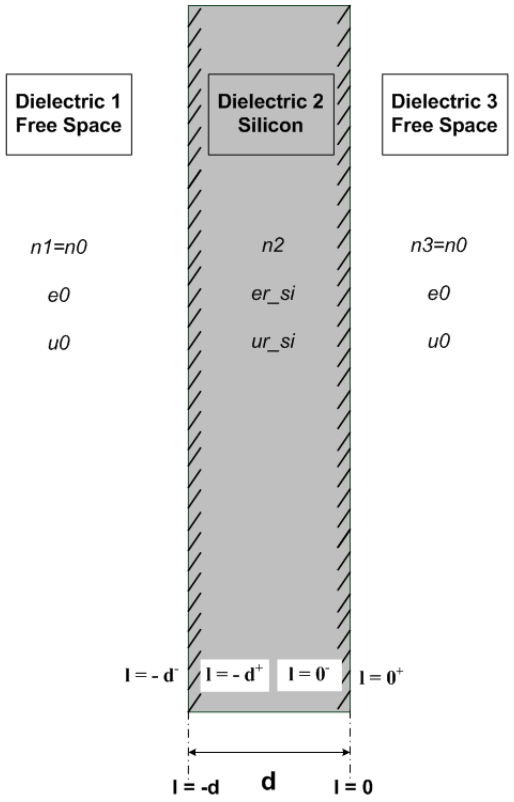


Figure 81: Schematic of dielectric boundaries.

```
% Initial values

f=50*1e9;
w=2*pi*f;
eo=8.854*1e-12;
uo=4*pi*1e-7;
no=377; % no=n1=n3
beta_o=w*sqrt(eo*uo);

d=0:0.1*1e-6:300*1e-6;
l=-300*1e-6;

er_si=11.7;
ur_si=1;
n2=no/sqrt(er_si);
```

Individual reflection coefficients could be determined at each of the boundaries. **Reflection_12** represents the refection cofficient at the first boundary between dielectric 1, the free space, and dielectric 2, the silicon substrate at a distance $l = -d$ .While **Reflection_23** is the reflection coefficient at the second boundary at $l = 0$. **Reflection_12** and **Reflection_23** contribute in the calculation of the total input refelction coefficient **Total _Reflection** at $l = -d^{-}$.

```
Reflection_12=(n2-no)/(n2+no);
Reflection_23=(no-n2)/(no+n2);
beta_2=w*sqrt(eo*uo*er_si*ur_si);

Total_Reflection=((Reflection_12)+(Reflection_23).*exp(-1i.*2.*beta_2.*d))./
(1+((Reflection_12).*Reflection_23.*exp(-1i.*2.*beta_2.*d)));
```

Using the total input reflection coefficient, the electric field on the substrate surface could be calculated as presented below.

```
Ei_Eo=exp(-1i.*beta_o.*l);

Er_Eo=Total_Reflection.*exp(1i.*beta_o.*l);

E_total=Ei_Eo+Er_Eo;

E_surface=1+Total_Reflection;
```

Figures 82(a) and 82(b) show the total input refelction coefficient and the amount of the electric field on the substrate surface with respect to the sbustrate thickness. It has been found that the reflection increases with the increase of the thickness substrate, as a result, the amount of the electric field on the surface is reduced. It is clear from Figure 82(b) that only 30 % of the incident electric field could be obtained on the substrate surface with a thickness of 300 µm.

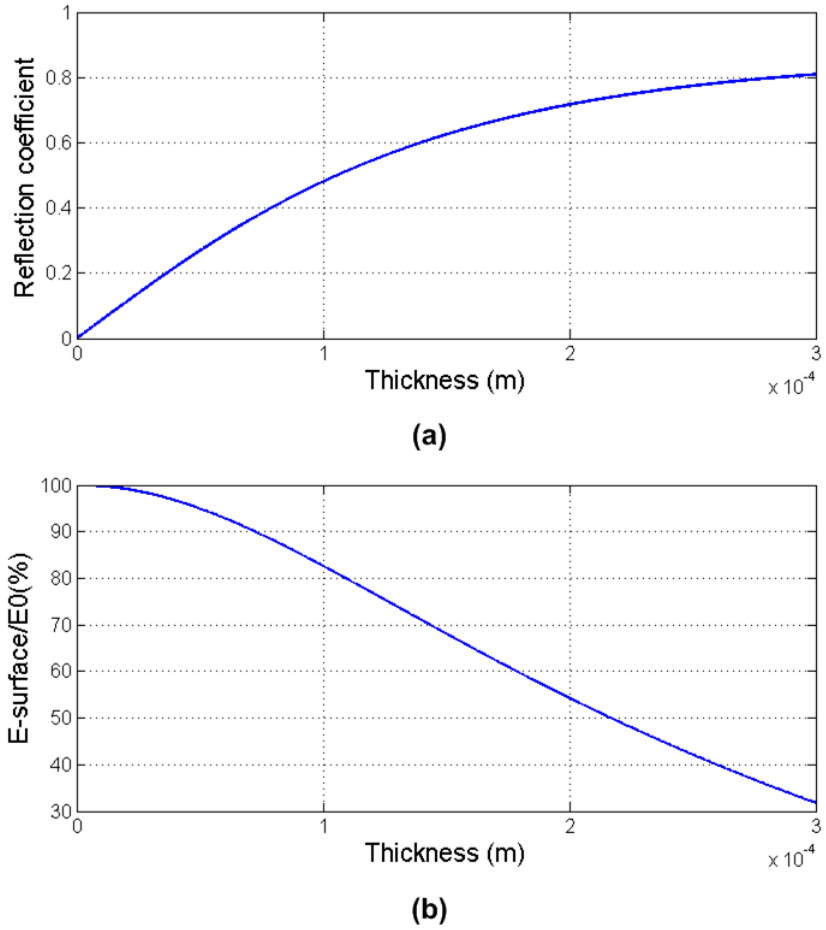


Figure 82: (a) Total input reflection coefficient and (b) amount of the electric field on the substrate surface with respect to the the substrate thickness

Étude de Nouveaux Dispositifs Miniaturisés Micro-ondes basés sur l'Effet Ratchet dans un Environnement de Nano-Diffuseurs Asymétriques

RÉSUMÉ

La nanotechnologie est un domaine en voie d'expansion qui a attiré l'attention de la recherche en raison de ses applications potentielles illimitées. La technologie des ondes millimétriques est un autre domaine intéressant qui joue un rôle de premier plan dans le développement des systèmes de communications sans fil. La combinaison de ces deux champs de recherche avancée, donne naissance à l'innovation du Dispositif Ratchet qui est une nouvelle application qui représente un vrai défi. Ce dispositif est de taille nanométrique et son concept d'opération consiste à générer une tension DC lorsque le dispositif, basé sur le gaz d'électron bidimensionnel, est rayonné par l'énergie des micro-ondes.

L'objectif de cette thèse est d'essayer d'améliorer la réponse du dispositif, ce qui ouvre de nouvelles perspectives dans la fabrication des détecteurs de champ à haute fréquence et à l'échelle nanométrique. Malheureusement, les Dispositifs Ratchet actuels, basés sur des hétérostructures de semiconducteurs, réalisés jusqu'à présent fonctionnent à basse température pour assurer une grande mobilité électronique. Cette condition nécessite l'utilisation d'un setup expérimental complexe qui a un grand impact sur la tension induite et sur la reproductibilité du phénomène Ratchet observé.

Dans ce contexte, le travail effectué dans le cadre de cette thèse a abordé ce problème en deux parties. La première partie concerne l'analyse électromagnétique du setup expérimental. Ceci a été réalisé par la mise en œuvre des simulations électromagnétiques intenses. D'autre part, différentes solutions ont été proposées afin d'optimiser le setup et ainsi améliorer la tension Ratchet produite. Outre l'étude électromagnétique, certaines mesures de modulation ont été réalisées pour tester la faisabilité du Dispositif Ratchet comme un démodulateur d'amplitude.

La deuxième partie de cette thèse traite l'étude de la matière qui compose le Dispositif Ratchet. Récemment, le graphène commence à envahir le monde scientifique et technologique avec ses fascinantes propriétés électroniques, tels que sa mobilité d'électrons élevée à température ambiante, où les matériaux conventionnels sont en train de confronter des obstacles. En conséquence, l'idée de fabriquer un Dispositif Ratchet à base de graphène au lieu des

hétérojonctions de semiconducteurs, a été introduite. Plusieurs modèles de conception, caractérisation et mesures RF ont été accomplis en vue d'obtenir un Dispositif Ratchet fiable approprié pour de nombreuses applications pratiques à la température ambiante, dans la gamme de fréquences micro-ondes et pourraient s'étendre à la bande térahertz.

-**Les mots clés :** Effet Ratchet, radiation micro-ondes, tension DC induite, modélisation électromagnétique, graphène, détecteur de champ électromagnétique